# RATIONAL DESIGN AND CHARACTERIZATION OF SOLUTION-PROCESSABLE ORGANIC PHOTOVOLTAIC DEVICES: A STUDY OF BOTH ORGANIC AND INORGANIC ARCHITECTURES

**Wenting Li**

**A DISSERTATION**

in

**Chemistry**

**Presented to the Faculties of the University of Pennsylvania**

in

**Partial Fulfillment of the Requirements for the Degree of Doctor of Philosophy**

**2013**

**Supervisor of Dissertation**

_____

Cherie R. Kagan

Professor of Electrical and Systems Engineering, Materials Science and Engineering, Chemistry

**Graduate Group Chairperson**

_____

Gary A. Molander

Professor of Chemistry

**Dissertation Committee**

Tobias Baumgart, Professor of Chemistry

Michael Fryd, Adjunct Professor of Chemistry

Bradford B. Wayland, Professor of Chemistry

*To my husband & my parents*

**ACKNOWLEDGMENT**

This dissertation not only represents five years of a PhD student's research work, but also the support of many people.

First, I would like to express my sincere gratitude to my current committee members, Prof. Baumgart, Prof. Wayland and Prof. Fryd. Thank you for your time and contribution which makes this dissertation possible.

To all the people contributing to this dissertation, thanks to Dr. Taegweon Lee for his contribution on the synthesis of C12DPP-π-BT polymer, NMR spectra, and GPC analysis; thanks to Soong Ju for his help with spatially resolved photoconductivity and intensity and electric field dependent photoconductivity measurements; thanks to Aaron for sharing his expertise on CdSe nanocrystals ligand exchange method, thanks to Sangam and Yu Jen's help with FET characterization, and thanks to my advisor, Dr. Kagan in supervising projects, experiments discussion, as well as great help with manuscript editing.

To all the people who encouraged me during the most depressed moments in my life: the professors and my graduate friends at Penn and outside of Penn. Thank you for teaching me to be a fighter and never give up.

Finally, a heartfelt thank you to my family, especially my beloved husband, Fumin Shi. Thank you for your endless support, encouragement and love.

# ABSTRACT

## RATIONAL DESIGN AND CHARACTERIZATION OF SOLUTION-PROCESSABLE ORGANIC PHOTOVOLTAIC DEVICES: A STUDY OF BOTH ORGANIC AND INORGANIC ARCHITECTURES

**Wenting Li**

**Cherie R. Kagan**

In this dissertation we report the synthesis and photovoltaic characterization of a number of semiconducting polymers and colloidal inorganic nanomaterials and their implementation into organic solar cells with different architectures (Schottky single layer, bilayer heterojunction, and bulk heterojunction), with research emphasis on the mechanisms underlying material and device optimization, which sheds light on future material design for high efficiency solar cells and other organic electronic devices, such as organic light emitting diodes (OLEDs) and organic field effect transistors (OFETs).

In the first part, the synthesis, characterization, and photovoltaic applications of a new conjugated copolymer (C12DPP-π-BT) are reported. The energy levels of C12DPP-π-BT were designed to be intermediate to those of popular electron donor and acceptor photovoltaic materials, P3HT and PCBM. The unique ambipolar nature of C12DPP-π-BT was then explored in two different photovoltaic systems where C12DPP-π-BT serves as either an electron donor or an acceptor when paired with PCBM or P3HT to form junctions with large built-in potentials. Optical, electrical, and structural characterization have been carried out to understand the photoinduced charge separation, charge carrier transport and recombination mechanism in different device configurations. The influence of polymers' molecular weight and processing condition on device performance has also

been explored. In addition, preliminary studies of OLED and OFET application of the C12DPP-π-BT have been carried out.

In the second part, the synthesis, surface ligand treatment and photovoltaic application of inorganic PbSe and CdSe nanocrystals have been investigated. In Chapter 3, photoluminescence quenching, current-voltage characterization and electrochemical measurements have been used to study the mechanism of photoinduced charge transfer between PbSe and P3HT, which confirmed material incompatibility and suggested new directions for the design of inorganic material as electron acceptor. In Chapter 4, the photovoltaic application of thiocyanate capped CdSe nanocrystals in combination with P3HT in bilayer hybrid devices has been explored. Important factors such as nanocrystal size and bilayer interfacial mixing on the device performance have been investigated and discussed. Bilayer solar cells with ligand exchanged CdSe nanocrystals and P3HT achieved 1.3% power conversion efficiency with good tunability in performance parameters and promising optimization potential.

**Table of Contents**

**List of Tables**

**List of Figures**

# Chapter 1

# Introduction

## 1.1 A Brief Historic Review of Solar Cells Technology

Currently, traditional fossil fuels dominate the world energy consumption market with a majority stake over 80%.[1] Due to the unsustainable nature of oil/gas/coal exploration and the rapidly increasing demands for energy, we are facing the challenge to find a renewable, environmentally friendly energy source to sustain the growth in population and maintain the development of civilization. Among various alterative renewable energy resources, such as solar energy, wind energy, geothermal energy, biomass, hydropower and ocean energy, solar energy is the most abundant resource.[2] Approximately 120,000 terawatts (TW) of solar energy reaches the earth's surface each day, far exceeding the current total worldwide energy consumption (~16 TW). If solar energy could be utilized efficiently (>10% power conversion efficiency) with low cost technologies, it may provide us the ultimate way to resolve the energy challenge.

In 1839, Becquerel discovered the photovoltaic effect.[3] He observed the generation of photocurrent when silver chloride (or silver bromide) coated platinum electrodes were illuminated in aqueous solution. After that, scientific interests mainly focused on the photoconductivity of materials and photocurrent conversion mechanism[4-6] until the late 1950s. In 1954, Chapin et al., successfully fabricated a photovoltaic device with 6% energy conversion efficiency, which marked the beginning of developing silicon-based solar cells for industrial application.[7] Silicon solar cell technology advanced rapidly with emerging technologies such as multicrystalline, microcrystalline, and amorphous silicon, and the silicon based solar cells have reached high power conversion efficiency over 20%. Today, silicon solar modules are by far the dominating photovoltaic devices, which account for more than 80% share of the photovoltaic market.[8] However, the high material

and production costs and the fragile nature of the silicon modules greatly limit their potential for large scale commercialization and market adoption to compete with traditional fossil fuels. In contrast, organic solar cells are receiving increasing attention as one of the promising candidates for future affordable energy due to their advantages of easily tunable properties, low cost, low temperature processing techniques, and the ability to be incorporated into flexible substrates such as plastic, paper or cloth. Later in this chapter we will briefly review the development of organic solar cells and three types of devices with different active layers geometry – single layer, bi-layer and bulk heterojunction.

## 1.2 Basic Concepts of Organic Solar Cells

## 1.2.1 Working principle

Before introducing the development of organic solar cells, the basic working principles and design criteria are briefly discussed in this section. Organic heterojunction solar cells will be used to illustrate the basic concepts. For organic semiconductors, absorption of light excites the electron from the valence band into the conduction band, generating a coulombically bound pair of an electron and a hole, called an "exciton", which can only be separated by energies much larger than kT at room temperature[9], or in the presence of large electric fields. There are four fundamental steps involved in the "light – electricity" power conversion process. (Figure 1.1)

(1) Absorption of light and generation of excitons

(2) Exciton diffusion

(3) Exciton separation to the opposite charges at the interface

(4) Charge transport and charge collection
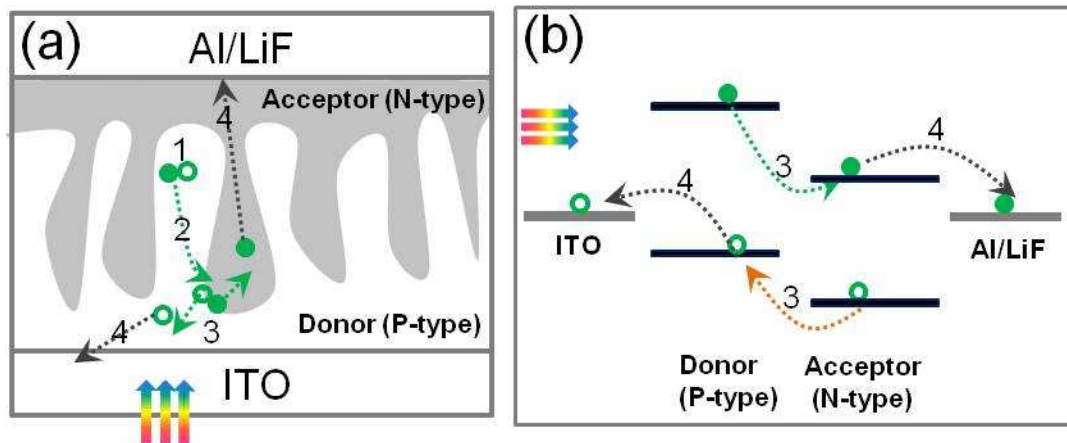


**Figure 1.1.** Schematic of the working principle of an organic photovoltaic cell (a) illustration of the 4 steps of energy conversion - 1) exciton generation, 2) exciton diffusion, 3) exciton separation, and 4) charge transport and collection; (b) energy band diagram showing an effective photoinduced charge separation and transfer. Filled circles represent electrons, and open circles represent holes. Green dotted lines represent the situation when the donor absorbs light and generates an exciton, while orange lines represent a similar charge generation process when the acceptor is photoexcited instead of the donor. In practice, an exciton can often be generated in both components.

Next, we will discuss the mechanism for each step and their design criteria:

(1) Upon illumination, photons with energy higher than optical bandgap ($E_g$) are absorbed by the active layer materials, exciting the electron from the highest occupied molecular orbital (HOMO) to the lowest unoccupied molecular orbital (LUMO). Absorbed photons then thermalize and release the excess energy via non-radiative decay. The photoexcitation results in a coulombically bound pair of electron-hole (a mobile

4

excited state, called an "exciton") rather than a free electron–hole pair. This occurs due to 2 reasons: 1) the attractive Coulomb interaction is strong due to the typically low dielectric constant of organic material and 2) the weak non-covalent electronic interactions between organic molecules results in a narrow bandwidth and a localized electron (hole) wave function around its conjugate hole (electron)[10]. Therefore, the photoexcitation generates a tightly bound electron-hole pair in organic materials (Frenkel exciton).

Design Criteria: Maximizing solar absorption. The absorption spectrum of the active layer should collect a large portion of the solar emission spectrum (Figure 1.2). Over 50% of solar energy lies in the red and NIR region while widely used organic semiconductors have absorption limited in the visible portion, causing large transmission loss. Strategies for maximizing solar absorption include: 1) chemically modifying and extending the effective conjugation of polymers or small organic molecules to red-shift the absorbance; 2) synthesizing nanocrystals with NIR absorption, such as PbSe; 3) fabricating multi-layer tandem devices to maximize the overall device absorption.
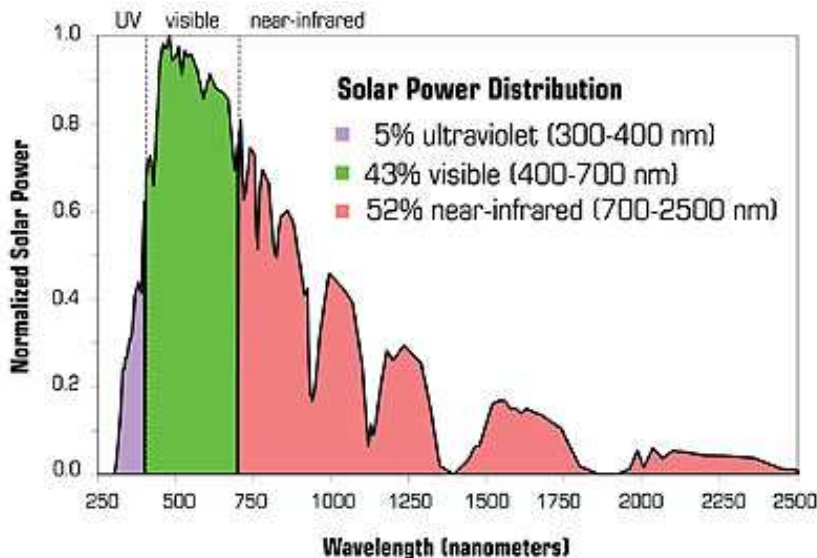
**Figure 1.2.** The solar radiation spectrum (Image courtesy of Lawrence Berkeley National Lab)

(2) The formed exciton diffuses to the interface between donor (p-type) and acceptor (n-type) where the electron-hole pair may be dissociated by a driving force (potential drop). The lifetime of an exciton is very short, and the exciton diffusion length is usually around 10-20 nm in organic material[11, 12].

Design Criteria: To ensure effective diffusion of exciton to the p-n interface, the material should be nano-engineered to have an intertwined structure with large interface. Micro-scale phase separation should generally be avoided and the distance between p-n junctions should be controlled to be less than 20 nm to allow the exciton to diffuse to the interface from the bulk component to get dissociated.

(3) At the interface, excitons are separated into holes and electrons and then driven towards different electrodes due to the potential drop (LUMO or HOMO offset) between

donor and acceptor materials, the photoinduced chemical potential energy gradient of electrons and holes, and the electrical potential energy difference provided by the asymmetrical ionization energy/work function of the electrodes. If the donor is photoexcited, the electron transfers from the LUMO of donor material to the LUMO of acceptor material which is energetically more favorable. If excitons are generated in the bulk of the acceptor upon illumination, holes will transfer from the HOMO of acceptor to the HOMO of donor. (Figure 1.3 (a)).
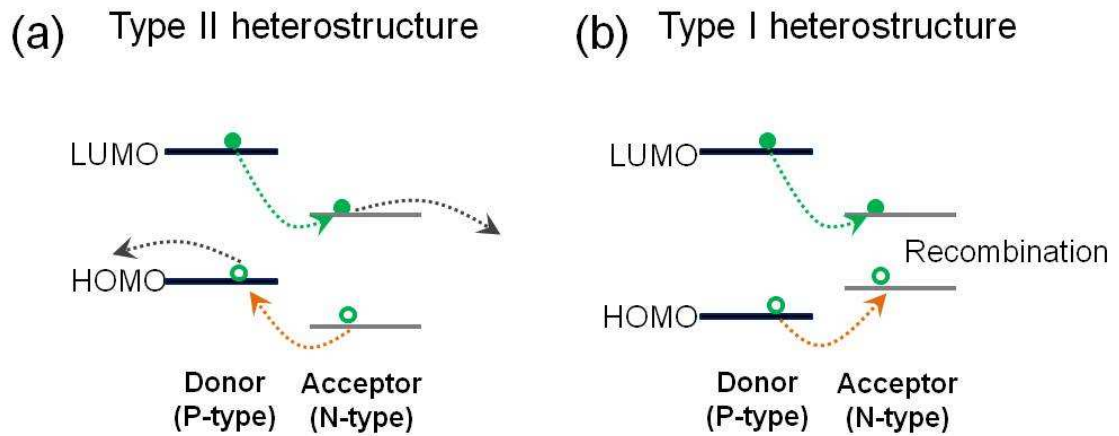


**Figure 1.3.** Schematic of type II and type I heterostructure (Details of band bending and discontinuity at the interfaces are omitted here for simplicity)

Design Criteria: A type II heterostructure is required for electrons and holes to be separated and transported into different phases to avoid charge recombination. As shown in Figure 1.3(b), if the electronic energy levels of two materials form a straddling gap rather than staggered gap, it results in a type I heterojunction, in which both electrons and holes tend to flow in the same direction (to the material with smaller bandgap) and

significantly increase the probability of charge recombination. Type I alignment is preferred for organic light-emitting diodes (OLEDs), which requires electrons and holes to move towards the same direction (emissive material). The recombination forms an exciton and the decay of the exciton (excited state) results in a relaxation of the energy levels of the electron accompanied by light emission. The working principle of solar cells (light-harvesting) is basically the reverse of the working principle of OLED (light-emitting). In the solar cell configuration, the presence of radiative and non-radiative recombination losses significantly decreases solar cell efficiency, which should be avoided for the solar cell devices design.

(4) After exciton dissociation at the interface, charges (electrons and holes) transport through percolation networks of different components or via hopping from site to site and eventually get collected at opposite electrodes.

Design Criteria: improve charge mobility and collection at the electrodes. Organic semiconductors typically have low mobility as compared to inorganic crystalline silicon[13, 14]. Tailoring the chemistry and structure of both donor and acceptor material to increase the charge mobility is critical to enhance the performance of PV device. The choice of electrodes should contain one transparent electrode, allowing maximum light pass-through and one counter metallic electrode reflecting light back into the active layer. The difference between two electrodes' workfunctions will assist the potential drop created by the active layer interface to drive holes and electrons to move towards opposite electrodes and get collected.

In summary, bulk heterojunction solar cell architecture requires the donor and acceptor materials to be tailored to provide: 1) strong and broad absorption of solar radiation, 2) a

staggered type II energy level structure to drive charge separation, 3) fine nano-structured mixture morphology to avoid charge recombination and 4) high hole and electron mobilities in the bulk and asymmetrical electrodes for facile charge transport and collection.

### 1.2.2 Device Layout

Organic solar cells are typically fabricated in a sandwich geometry, which is also called vertical structure (Figure 1.4(a)) since current transport direction is perpendicular to the device substrate. Transparent glass or plastic are generally used as the substance. Indium tin oxide (ITO) is sputtered on the substrate and works as the bottom electrode because of its high optical transparency, good electrical conductivity and high work function. Due to the low abundance of indium and high cost of ITO, there are many research efforts to develop low cost alternatives, such as conducting polymers and carbon nanotubes. On the ITO glass, a conducting polymer mixture, Poly(3,4-ethylenedioxythiophene) : poly(styrenesulfonate) (PEDOT:PSS) is often used to coat the ITO by spincasting from an aqueous solution. PEDOT:PSS smoothens the rough ITO surface to reduce the probability of shorts and serves as a hole extraction layer because of its high work function (5.1eV±0.2eV).[15] The chemical structure of PEDOT:PSS is shown in Figure 1.4(b). Recent research effort involves improvement of the conductivity or modification of work function of PEDOT:PSS by using additives or modifying the functional groups of this polymer blend. The middle active layer can be deposited from solution or via vacuum deposition. Finally, on the active layer, a top electrode consisted of a low work function metal (Aluminum or Calcium) with an ultra-thin layer (0.6-1nm)

of lithium fluoride (LiF) is deposited by vacuum thermal evaporation. The inserted LiF

lowers the work function of Al and serves as an electron extraction layer[16].
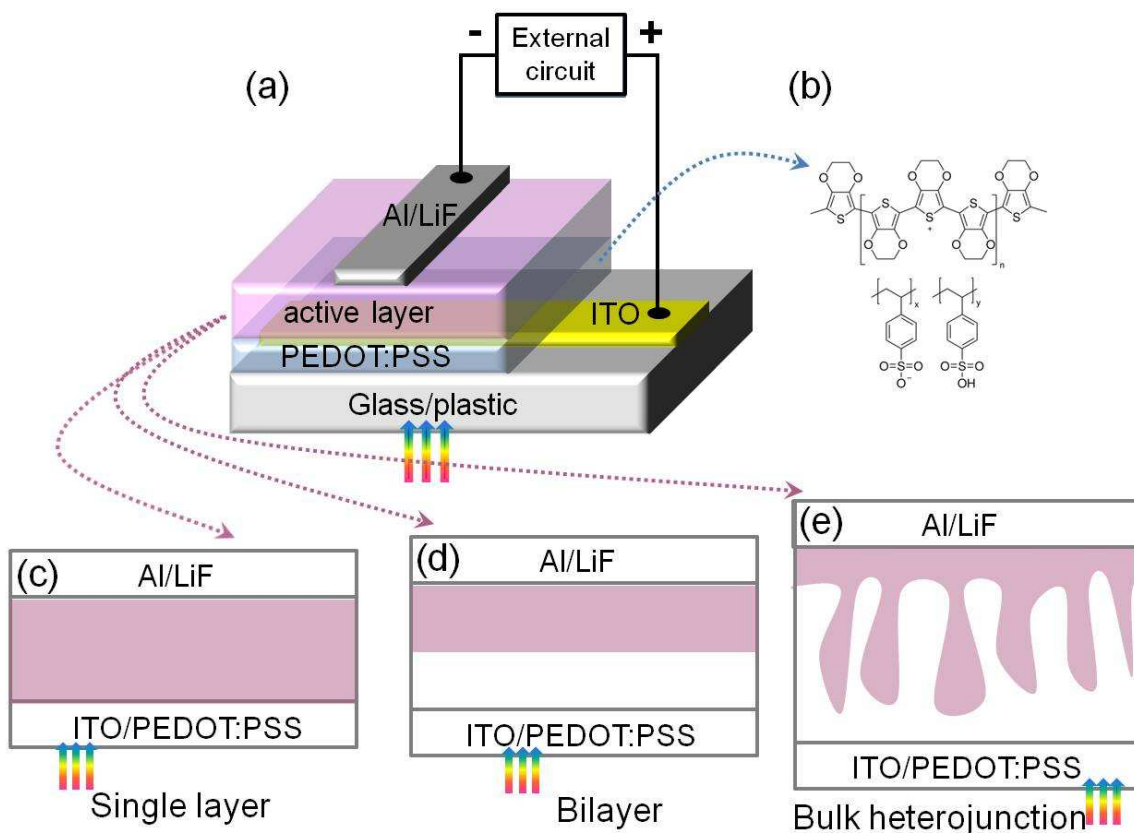


**Figure 1.4.** (a) Schematic of an organic solar cell device (b) the chemical structure of PEDOT:PSS (c-e) different solar cell device layouts: categorized by the architecture of the active layer. There are three configurations: (c) single layer (d) bilayer heterojunction and (e) bulk heterojunction.

Based on the morphology and number of components in the active layer, there are three basic device architectures: 1) single layer - one active component, 2) bilayer - two

active components (p-type and n-type) sequentially deposited, stacking on top of each other, and 3) bulk heterojunction - two active components (p-type and n-type) co-deposited as a mixture. (Figure 1.4 (c-e)) Their main differences lie in exciton dissociation and subsequent charge transport locations. As we previously discussed in the working principle section, the exciton dissociation/charge separation process is critical for the design of efficient solar cell devices. So here we will extend the concepts to these three architectures and briefly discuss their advantages and disadvantages.

(1) Single layer photovoltaic devices

The single layer organic solar cell is one of the earliest developed structures in organic photovoltaics history. It has the simplest configuration which is composed of, from the bottom to the top, ITO (or thin semi-transparent metal)/photoactive semiconducting material/metal. Upon illumination, the middle active layer absorbs photons and generates excitons. The excitons diffuse to the interface between semiconductor and metal electrode and get dissociated there. As shown in Figure 1.5, the potential drop and band bending creates a depletion region (w) near the contact interface providing the separation force for the exciton and driving the electrons towards the more energetically favorable low work function electrode. The difference of work function between the two electrodes builds up an electric field in the organic layer, assisting the charge separation and collection process. This metal-semiconductor interface with rectifying characteristics is called Schottky barrier; therefore devices based on this type of junction are also called Schottky solar cells.
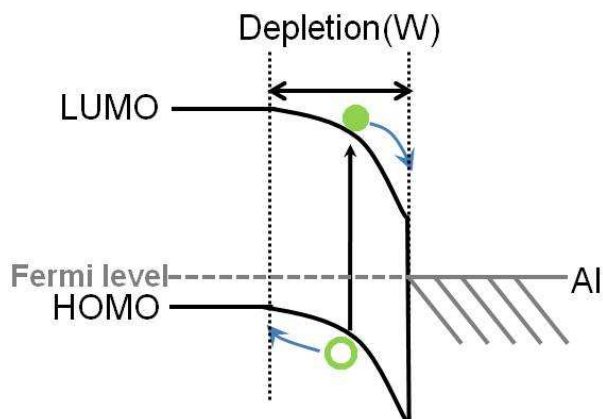
**Figure 1.5.** Schematic of energy band diagram for a single layer solar cell. Schottky device with p-type semiconductor and aluminum electrode is used for illustration. Green filled circle represents electrons and green hollow circle represents holes.

Advantages and disadvantages: this type of devices is relatively easy to fabricate with low production cost. Many materials, such as semiconducting polymers, small organic molecules and colloidal inorganic nanocrystals can be used as the active layer material.[17, 18] However, there are 4 main disadvantages: 1) as we previously discussed, the exciton diffusion length is shorter than 20nm, so that only excitons close to the interface can get dissociated and contribute to the photocurrent (exciton diffusion limited); 2) interfacial area is typically small; 3) the potential drop at the semiconductor-metal interface is not always sufficient to break the excitons; and 4) charge recombination probability is high because both electrons and holes transport within the single material. All these factors reduce the device efficiency.

(2) Bilayer heterojunction photovoltaic devices

In bilayer heterojunction devices, two active components (p-type and n-type semiconductor) are sequentially deposited between the electrodes. Both layers can absorb light and generate excitons. To promote effective exciton dissociation, a sharp potential drop at the donor (p-type) - acceptor (n-type) interface is created by choosing one component with high HOMO and LUMO and the other component with low HOMO and LUMO to form a type II heterojunction. Excitons diffuse to such interface and dissociate into opposite charges. (Figure 1.6)
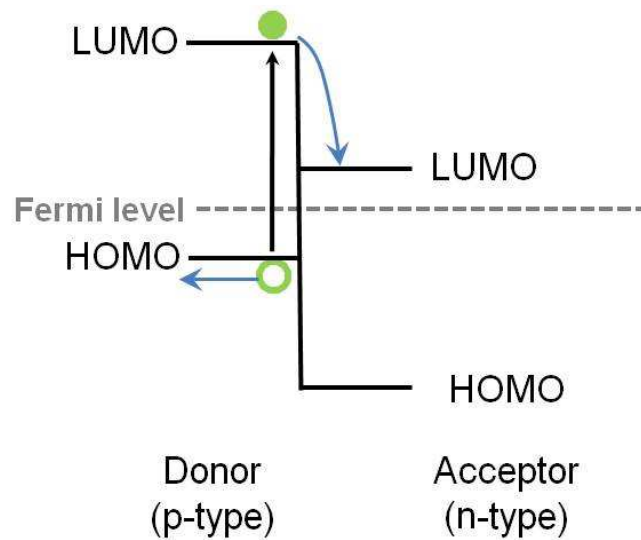


**Figure 1.6.** Schematic of energy band diagram for a bilayer layer solar cell. (Exciton generated in p-type semiconductor is used for illustration.) Green filled circle represents electrons and green hollow circle represents holes.

Advantages and disadvantages: compared with single layer devices, bilayer devices are more advanced because of 2 reasons: 1) electrons and holes can travel in different components after separation, which decreases the charge recombination probability; 2) two components can be carefully chosen to maximize total light absorption and to create

13

a large potential drop at p-n interface to promote more effective charge separation. However, such design still suffers from limited interfacial area and short exciton diffusion distance, both of which reduce the efficiency of exciton separation in the devices.

(3) Bulk heterojunction (BHJ) photovoltaic devices

In BHJ devices, two active components (p-type and n-type semiconductor) are mixed and co-deposited between the electrodes. The working mechanism is very similar to the bilayer heterojunction. (Same as shown in Figure 1.6) The main difference is that the donor and acceptor materials are intimately mixed; therefore, the heterojunctions are present at much larger areas within the bulk.

Advantages and disadvantages: compared with bilayer layer device, bulk heterojunction devices have several distinct advantages: 1) theoretically the donor/acceptor phase separation can be controlled within 10-20 nm scale so that most excitons are able to diffuse to the interface and get separated; 2) very large interfacial area; 3) without the exciton diffusion limitation, the thickness of bulk heterojunction devices can be increased to maximize light absorption. However, this type of devices requires fine control of mixing morphology at nanoscale level. In the ideal structure, the two components (donor and acceptor phases) need to form interpenetrating and bicontinuous percolation path for both holes and electrons to transport separately towards different electrodes. Phase separation of donor and acceptor materials and the presence of recombination sites cause reduction of device performance.

**1.2.3 Device Performance Measurements and Performance Parameters**

To make organic solar cell an affordable alternative to traditional fossil fuels, energy conversion efficiency is one of the most important parameter for solar cells besides cost consideration. The performance of a solar cell is measured by current-voltage (I-V) characterization. For measurement, the device is connected with a source-meter and current density is recorded against applied voltage in the dark and under illumination from a solar simulator. The standard light source adopted in solar cell research to measure device power conversion efficiency is Air mass 1.5 global (AM 1.5G) illumination (1 sun, 100 mW/cm$^2$), which mimics the sun light reached on the earth's surface at an incident angle of 48.2° at sea level. Figure 1.7 illustrates the I-V curves for a typical solar cell device. When operated in the dark, it behaves like diode with almost no current in the reverse bias (negative voltage) direction and turned on in the forward bias direction, where current density increases substantially. When operated under illumination, the solar cell device generates power in the fourth quadrant of the I-V curve. (Figure 1.7 (b)) Open circuit voltage ($V_{oc}$) and short circuit current ($I_{sc}$) are determined at intersections of x and y axes, respectively. $V_{oc}$ is the voltage across the cell under illumination with no current (an open circuit) , which is the maximum possible voltage of the solar cell. $I_{sc}$ is the current under illumination with no external resistance (short circuited), which is the maximum possible current that the solar cell can produce. The product of I and V (I*V) at any point on the curve equals the output power. The current and voltage that allow the maximum output power ($P_{out}$) are called $I_{max}$ and $V_{max}$. The ratio of $P_{out}$ and $I_{sc}*V_{oc}$ is defined as fill factor (FF). The overall energy conversion efficiency is calculated by the following equation:

$$\eta_{eff} = \frac{P_{out}}{P_{in}} = \frac{V_{max} * I_{max}}{P_{in}} = \frac{V_{oc} * I_{sc} * FF}{P_{in}} \qquad (1)$$

$$FF = \frac{V_{max} * I_{max}}{V_{oc} * I_{sc}} \qquad (2)$$

where $P_{out}$ is the maximal output power of device under illumination, $P_{in}$ is the input light power measured in $mW/cm^2$, $V_{oc}$ is the open circuit voltage measured in V, and $I_{sc}$ is the short circuit voltage measured in $mA/cm^2$.
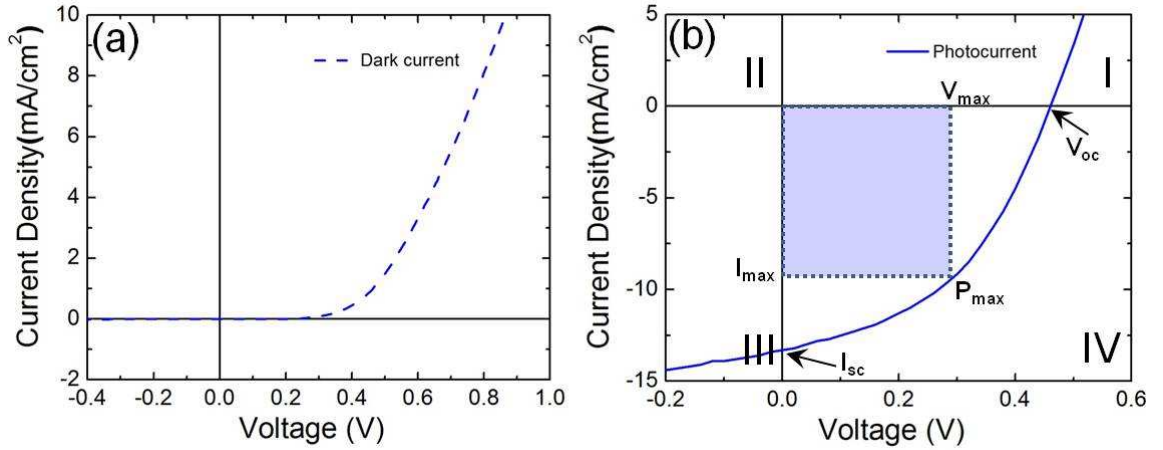


**Figure 1.7.** I-V characteristic curves of a solar cell (a) in dark and (b) under illumination. The square represents $P_{out}$ - the largest product of V*I. (Note: the solar cell device generates power in the fourth quadrant (IV). In the third quadrant (III), the illuminated device works as a photo-detector, consuming power to generate light-dependent photocurrent. In the first quadrant (I), the device also consumes power, entering light-emitting-diode operating region.)

To maximize the device performance, all three critical parameters ($V_{oc}$, $I_{sc}$, and FF) shall be optimized. The origin of $V_{oc}$ is still under much debate [19-21] and the $V_{oc}$ may be affected by many factors, such as energy levels of materials, charge recombination and electrode contacts. However, a generally accepted hypothesis is that the $V_{oc}$ is positively correlated with the difference between HOMO level of the donor and LUMO level of the acceptor.[19, 22] Therefore, using a donor material with low lying HOMO and/or using an acceptor material with high lying LUMO will in principle increase the $V_{oc}$. $I_{sc}$ measures the device's ability to convert photons to photocurrent. It can be improved by several strategies: 1) reducing optical bandgap and increasing absorption wavelength into the red and NIR region by extending effective conjugation length of organic molecules/polymers[23] or, in the case of nanocrystals, by adjusting quantum confined property[24]; 2) increasing the interfacial area to ensure that more excitons can reach the interface for dissociation[25], 3) optimizing energy levels of donor and acceptor to achieve efficient charge separation. It is estimated that the energy difference between the LUMO levels of donor and acceptor should be generally larger than 0.3 eV (the exciton binding energy in the donor polymer) for efficient charge separation[19, 26], 4) using materials with high mobility and bi-continuous percolation pathways to facilitate electron and hole transport and reduce charge recombination.[27, 28]

Besides $V_{oc}$ and $I_{sc}$, fill factor (FF) is another important parameter to determine the device efficiency. It measures the "squareness" of the I-V curve and reflects the internal loss of generated photocurrent for realistic solar cells. The shape of the I-V curve is affected by equivalent series resistance ($R_s$) and shunt (parallel) resistance ($R_{sh}$) between

the two electrodes. The current flow (I-V relationship) for this equivalent circuit can be described as

$$I = I_{sc} - I_0 \cdot \{\exp[\frac{e(V - IR_s)}{nkT}] - 1\} - \frac{V - IR_s}{R_{sh}} \quad (3)$$

where $I_0$ = reverse saturation current, e = elementary charge, n = diode ideality factor (1 for the ideal diode), k = Boltzmann's constant, T = absolute temperature, $R_s$ = series resistance, and $R_{sh}$ = shunt resistance.

The corresponding equivalent circuit is shown in Figure 1.8 (a). As depicted in Figure 1.8 (b,c), the high fill factor is achieved by reducing the equivalent series resistance ($R_s$) and increasing shunt (parallel) resistance ($R_{sh}$). The series resistance ($R_s$) is determined by the bulk resistance of active material and contact resistance between each layer to the current flow. Shunt resistance ($R_{sh}$) is a measurement of leakage current between the two electrodes, which is affected by the impurities and defects in the active semiconductor layer. Therefore, FF can be optimized by controlling the stacking/blending morphology of each component, modifying interface contact and thickness of each layer and reducing material/fabrication defects[29-31].
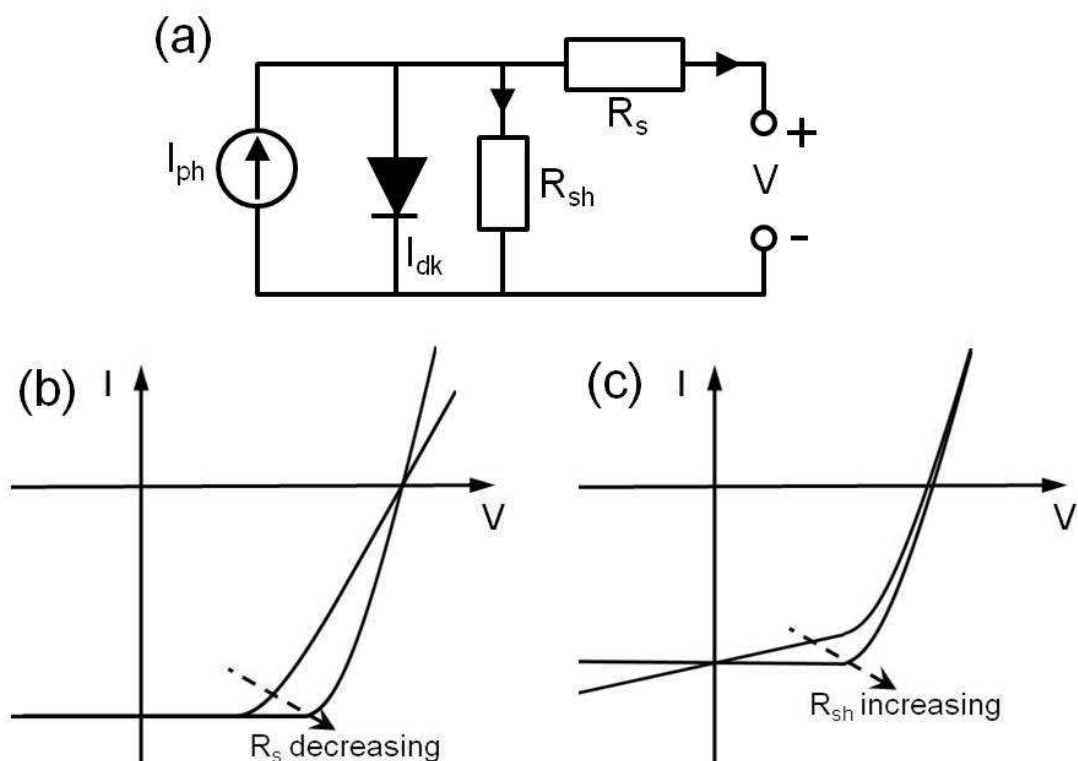
**Figure 1.8.** (a) Equivalent circuit for organic solar cells. The serial resistance represents the bulk resistivity of each layer and the contact resistivity, while the shunt resistivity $R_{sh}$ represents all the factors that influence shunts. And $I_{ph}$ and $I_{dk}$ represent photocurrent and dark current, respectively. (b,c) I-V characteristic curve of a solar cell showing effects of (b) decreasing series resistance ($R_s$), and (c) increasing shunt (parallel) resistance ($R_{sh}$). $R_s$ is estimated from the I-V curve inverse slope at large forward voltage and $R_{sh}$ is estimated from I-V curve inverse slope at zero forward voltage.

## 1.2.4 An introduction to Organic Solar Cells

Based on the materials of active layer, there are three main types of organic solar cells: 1) small organic molecule solar cells, 2) polymer solar cells – devices typically consisting

of conjugated polymers and fullerene derivatives, such as [6,6]-Phenyl-C61-butyric acid methyl ester (PCBM), and 3) hybrid solar cells – devices typically consisting of conjugated polymers and inorganic nanomaterials.

(1) Small organic molecule solar cells

The small organic molecule solar cell is one of the earliest types in organic photovoltaics research history (Figure 1.9). In 1975, Tang reported the first small organic molecule solar cells with chlorophyll a as the active component.[32] It was a single layer device exhibiting 0.001% efficiency. Later, metal phthalocyanine (Pc) complexes and merocyanine dye were used which improved device efficiency to 0.7%.[33] However, the single layer devices suffered from low charge separation efficiency and high recombination loss as discussed in section 1.2.2. So researchers shifted their focus to the development of bilayer planar heterojunction devices. In 1986, the first bilayer device was reported using Cu-phthalocyanine as donor and perylene-3,4,9,10-bis(benzimidazole) as acceptor, which achieved an efficiency of 0.95%.[34] To improve the charge transport and utilize incident light more efficiently, Leo and Maenning introduced a new device layout called "p-i-n", where p, i and n stand for a p-type semiconductor, an intrinsic absorber and a n-type semiconductor.[35] The p and n type materials are typically wide bandgap doped semiconductors and serve as transport layers exclusively for holes or electrons. The intrinsic layer is typically a bilayer or bulk heterojunction (blends) of two highly absorbing materials and only this layer absorbs visible light (the device structure is shown in Figure 1.9). The relative position of middle absorber can be optimized to form an optical interference pattern to enhance light absorbance in the photoactive region to have better light utilization and also reduce recombination loss at contacts. Based on this

p-i-n structure, Maenning reported a device efficiency of 1.9%, which represents a great

improvement of the energy conversion efficiency of small organic molecule solar cells.[35]
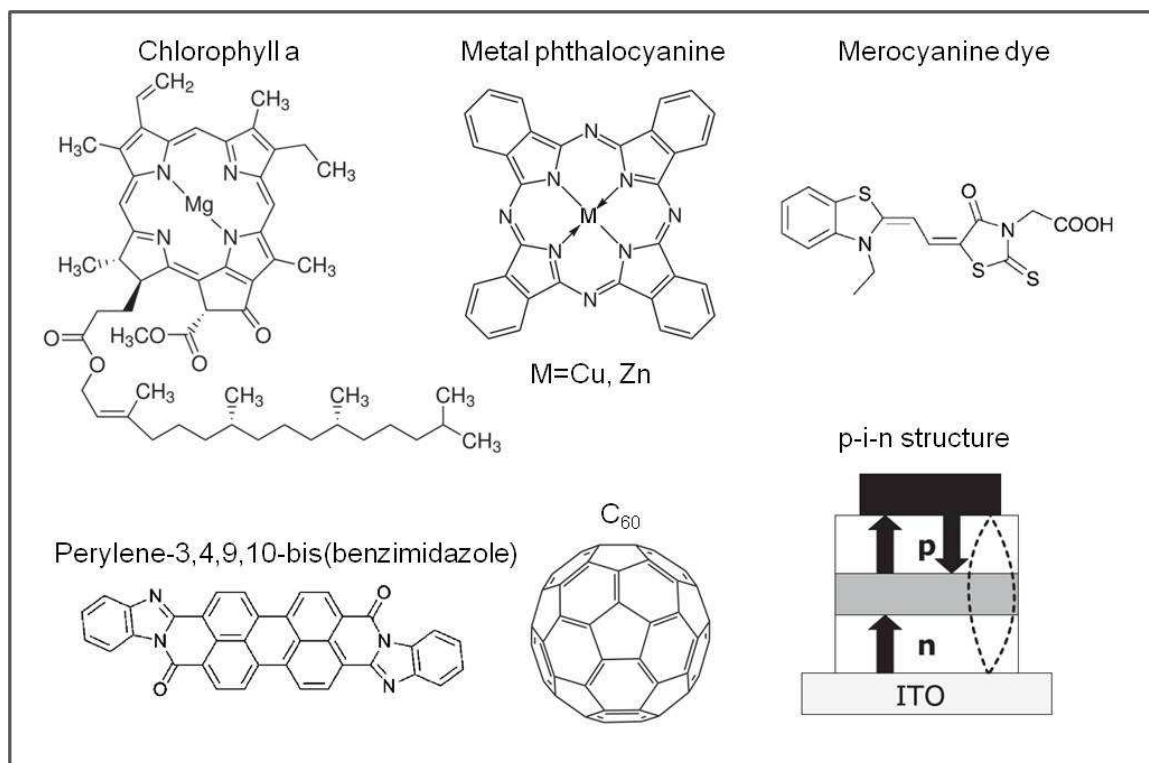


**Figure 1.9.** Chemical structures of commonly used small organic molecule materials for solar cells. The last schematic picture showing p-i-n structure is adapted from reference [34]. The black arrows show the light path including reflection at back electrode. The dotted lines represent the light intensity.

(2) Polymer solar cells

Many of the bilayer small molecule solar cells previously discussed are fabricated by vacuum deposition which incurs high fabrication cost. In contrast, semiconducting polymers possess the distinct advantage of solution processability and can be easily

coated on the plastic for flexible solar cells. The widely used conjugated polymers have excellent solubility in common solvents such as chloroform and chlorobenzene. However, the charge mobility in polymers is typically low and most polymers are dominantly p-type, which makes it only suitable as the donor materials. Therefore, fullerene derivatives such as PCBM are generally used as electron acceptor in combination with these p-type conducting polymer to fabricate bulk heterojunction solar cells because of its high electron affinity and excellent electron mobility. As we discussed before, the morphology control of the blends is critical. Many research efforts focuses on fine-tuning the processing conditions, such as adjusting the solvents, additives, and annealing conditions to optimize the phase separation to form the interpenetrating, and bicontinuous percolation path for both holes and electrons[16, 25, 36-40]. The first application of fullerenes as the acceptor material in solar cells was reported by Sariciftci and Heeger in 1992 using Poly[2-methoxy-5-(2-ethylhexyloxy)-1,4-phenylenevinylene] (MEH-PPV)[41], after which extensive research was conducted using MEH-PPV and other alternative polymers such as Poly[2-methoxy-5-(3′,7′-dimethyloctyloxy)-1,4-phenylenevinylene] (MDMO-PPV) and Poly(3-hexylthiophene-2,5-diyl) (P3HT) in combination with the fullerene derivative PCBM.[42] Among the commercially available polymers, P3HT exhibits a high hole mobility and a relatively broad absorption spectrum and has received the most attention. Broad topics have been explored and discussed to improve device efficiency, such as molecular weight, Polydispersity index (PDI), regioregularity of P3HT, PCBM weight ratio, solvent choice, annealing time and annealing temperature. The highest reported efficiency is 6.53% by Lee and Park[43]. However, the average efficiency of all reported value is only 3% based on a survey of results[44] from 388 publications in 2010, with a

wide spread from 0.1% to 5.5% due to the complexity of the polymer chemistry and device engineering. P3HT and PCBM are still the most attractive materials commercially available and continue to receive extensive research attention. In the last few years, a new strategy utilizing donor-acceptor copolymers to synthesize more conjugated, lower band gap polymers with extended overlap with the solar spectrum has been developed rapidly.[45-47] For example, an impressive device efficiency of 6.1% has been achieved with the alternating co-polymer, poly[N-9''-hepta-decanyl-2,7-carbazole-alt-5,5-(4',7'-di-2-thienyl-2',1',3'-benzothiadiazole) (PCDTBT) in the bulk heterojunction structure with PC$_{71}$BM.[48] Figure 1.10 summarizes the commonly used p-type and n-type materials for polymer solar cell applications.
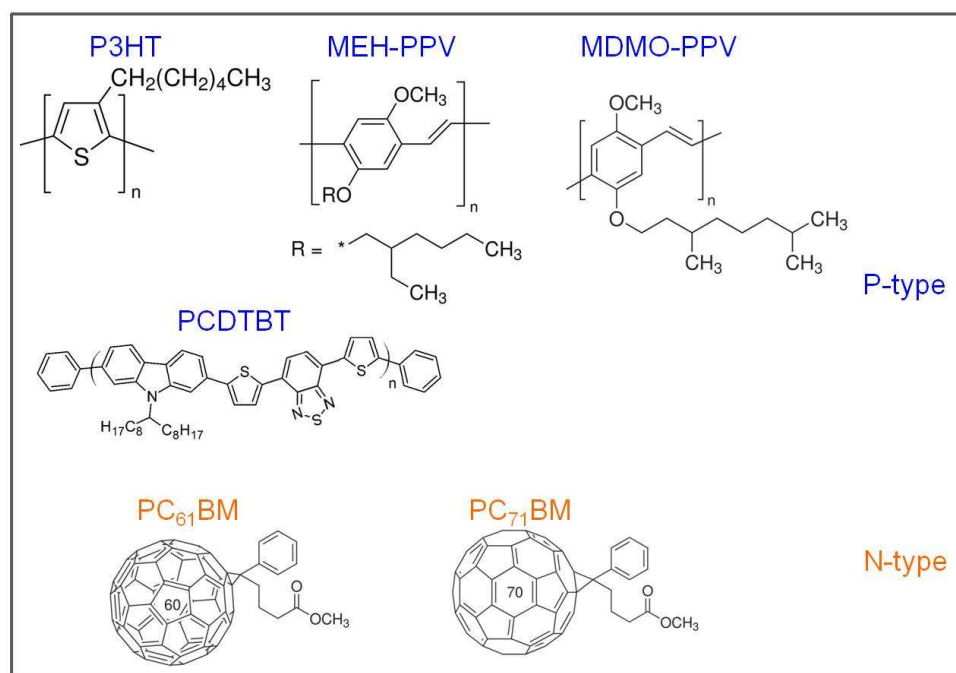


**Figure 1.10.** Chemical structures of commonly used commercial available p-type (P3HT, MEH-PPV, MDMO-PPV) and n-type (PCBM) material for polymer solar cells and the recently developed donor-acceptor copolymers PCDTBT (p-type).

(3) Hybrid solar cells

Organic-inorganic hybrid bulk heterojunction solar cells are considered to be one of the most promising candidates for the development of high efficiency photovoltaic devices due to their excellent morphological, optical and electrical property control of the inorganic components[38, 49-52]. Compared to the polymer solar cells, the electron acceptor material PCBM is replaced by inorganic nanomaterials, since PCBM contributes very little to light absorption and exciton generation despite its good electron transport properties and fast charge transfer when in combination with polymers. In contrast, inorganic colloidal semiconductor nanocrystals display excellent quantum confinement and tunable optical properties with absorption covering a broad spectrum of light, in addition to potentially higher electron mobility[53-56].

Many semiconductor nanocrystals, such as CdS, CdSe, CdTe, PbS, PbSe, Si, $TiO_2$, and ZnO nanocrystals have been incorporated into efficient hybrid devices in conjunction with semiconducting polymers for hybrid solar cell fabrication[37, 57-60]. Lead chalcogenide nanocrystals exhibits extended absorption in the NIR region and cadmium chalcogenide nanocrystals have strong absorption covering the main visible region, which makes them two promising candidates. Also, the elongated structure of inorganic components at 10-200 nm scale may provide an efficient percolation pathway for charge transport, such as nanorods[38] and branched nanoparticle[61]. CdSe nanocrystals were the first inorganic nanocrystal to be applied into hybrid solar cells. In 1996, Greenham reported the first CdSe nanocrystals based devices in combination with MEH-PPV with 0.1% efficiency.[57] The main practical challenge for preparing hybrid devices lies in the ligands used in the wet-synthesis process of inorganic nanocrystal. In general, long ligands, such as oleate,

are widely used for nanocrystal synthesis to facilitate shape control and also stabilize the nanocrystal in the synthesis and in stock solutions to prevent aggregation and phase separation. However, this layer works as an insulating layer and hinders electron transfer upon incorporation into solar cells. Two strategies have been used to overcome these disadvantages: 1) ligand exchange process, which uses shorter ligand to replace the long chain ligand after synthesis and 2) synthesizing elongated nanocrystal so the electron can hop less before reaching the electrode, which reduces the loss in charge carrier transport. In 2002, Huyuh reported the incorporation of pyridine ligand exchanged CdSe nanorods into P3HT and greatly enhanced the efficiency to 1.7%, which was a successful demonstration of the strategies mentioned above[38]. Nowadays, research in the hybrid solar cell field has two focuses: 1) ligand exchange treatment of nanomaterials and incorporation of nanocrystals with different morphology and 2) synthesis of polymers with longer conjugation length to have a better absorption match with the solar spectrum and high charge mobility.

Recent Developments and New Concepts

Besides the basic device layouts and materials discussed above, tandem solar cells become the most attractive candidate for organic photovoltaic device design, targeting 10-15% power conversion efficiency, which is considered the threshold efficiency for commercialization. The concept of tandem device is to combine two or more single solar cells with complementary absorption to enhance photon utilization, and therefore increase the device efficiency. As shown in Figure 1.11(a), a typical tandem solar cell has two sub-cells (heterojunction solar cells) stacking on top of each other with a highly transparent

intermediate layer (ultra thin metal, doped small molecule layers, metal oxides, metal carbonates or conducting polymer) in-between[62-66]. The two sub-cells have complementary absorption spectra so the light that is not absorbed by the bottom layer can be absorbed by the top layer (Figure 1.11 (a,b)). The two sub-cells are usually connected in series. As depicted in Figure 1.11(c), the function of the intermediate layer is to connect the top sub-cell and bottom sub-cell while align the LUMO level of the acceptor of one device with the HOMO level of the donor of the other device and allow sufficient charge recombination to prevent sub-cells from charging. To date, the highest record for organic tandem solar cell is 10.6%, reported by UCLA-Sumitomo Chemical, which utilized a new, infrared-absorbing polymer material provided by Sumitomo Chemical of Japan[67].

Instead of stacking geometry, Tvingstedt et al. developed a novel geometrical modification of a tandem solar cell, described as "folded reflective tandem cell"[68]. As sketched in Figure 1.11(d), the sub-cells are folded and form a specific angle which directs the reflected light from one device towards the other. This design has a few advantages over the traditional stacked tandem device[68]: 1) longer light path due to the incident light angle 2) more absorption because of light trapping 3) relatively easier to fabricate tandem solar cells in series or parallel connection since the two sub-cells are more independent than the stacked device.
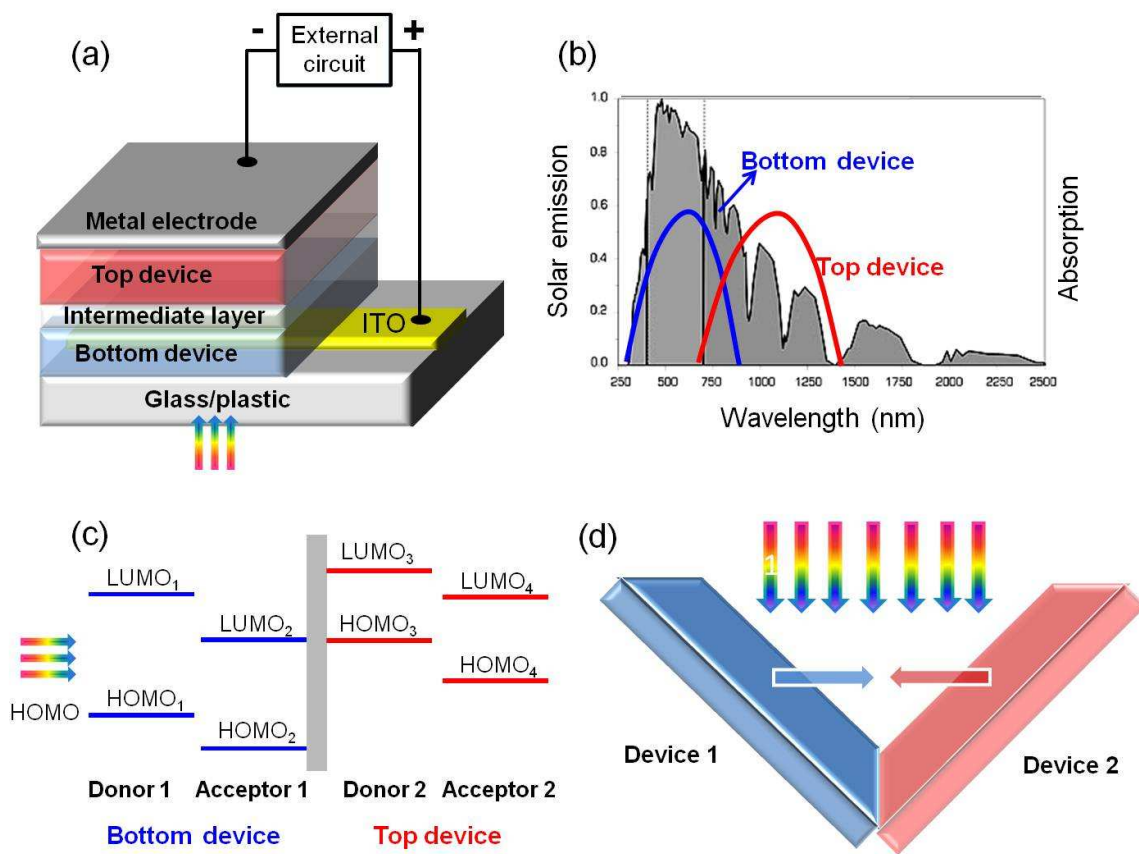
**Figure 1.11.** (a) Schematic of organic tandem solar cell device. (b) Complementary absorption spectra of top and bottom devices. (c) Energy diagram of sub-cells (d) schematic of "folded reflective tandem cell".

## 1.3 Thesis Outline

In this thesis, a broad range of topics is covered from synthesis of colloidal inorganic nanomaterials and semiconducting polymers to material characterization and implementation into organic solar cells with different architectures (Schottky single layer, bilayer heterojunction, and bulk heterojunction), with research emphasis on the mechanism underlying material and device optimization, which sheds light on future

material design for high efficiency solar cells and other organic electronic devices, such as OFET and OLED.

Chapter 1 briefly reviewed the history of photovoltaic devices development and discussed the working principle, design criteria, and important concepts of the architecture of organic solar cells.

In Chapter 2, the synthesis, characterization, and implementation of a new diketopyrrolopyrrole-based polymer (C12DPP-$\pi$-BT) with energy levels located between those of commonly used electron donor and electron acceptor materials are reported, with the novel ambipolar property of C12DPP-$\pi$-BT demonstrated in solution-processable organic photovoltaic application. Next, the importance of molecular weight of polymer, the processing condition and their influence on device performance are explored. In addition, the photoinduced charge separation and recombination mechanism in different donor-acceptor system are studied to understand the device performance parameters. Finally, preliminary results of polymers in OLED application and ambipolar transistor application of polymer:PCBM blends are demonstrated.

Part of this Chapter has been published as: Li, W., Lee, T.; Oh, S.; Kagan, C. R., Diketopyrrolopyrrole-based $\pi$-bridged Donor-Acceptor Polymer for Photovoltaic Applications, ACS Appl. Mater. Interfaces 2011, 3, 3874. Dr. Taegweon Lee contributed to the synthesis of C12DPP-$\pi$-BT polymer, NMR spectra, and GPC analysis. Soong Ju Oh contributed to spatially resolved photoconductivity, intensity and electric field dependent photoconductivity measurements. Prof. Cherie Kagan contributed to many helpful experiments discussions and manuscript preparation.

In Chapter 3, the synthesis and photovoltaic application of PbSe nanocrystals in combination with P3HT are explored. Photoluminescence quenching, current-voltage characterization and electrochemical measurements have been used to study the mechanism of photoinduced charge transfer between PbSe and P3HT. To remove long capping oleate ligands (insulating layer), both post-synthesis ligand exchange methods and direct synthesis of PbSe nanocrystal/nanowires in polymer P3HT solution without the use of oleic acid have been investigated.

In Chapter 4, the photovoltaic application of thiocyanate capped CdSe nanocrystals in combination with P3HT are demonstrated and the influences of factors such as nanocrystal size and bilayer interfacial mixing on the device performance have been explored. Currently, the reports about bilayer devices based on CdSe nanocrystals and organic material are very limited. In our study, the size of the nanocrystals was tuned to take advantage of quantum confinement, to optimize the short circuit current and open circuit voltage. Our bilayer solar cell with ligand exchanged CdSe nanocrystals and P3HT demonstrate decent efficiency (1.3%) with good tunability and optimization potential. We also fabricated inverted bilayer solar cells with high work function electrode to improve air stability of the devices. Benjamin Diroll contributed to the preparation of CdSe nanocrystals. Dr. Aaron Fafarman contributed to the development of the CdSe ligand exchange method.

## 1.4 References

1.      Guo, K. W. *International Journal of Energy Research* **2012,** 36, (1), 1-17.

2.      Lewis, N. S. a. C., George *Report of the Basic Energy Sciences Workshop on Solar Energy Utilization, April 18-21* **2005**.

3.      Becquerel, A. E. *Comptes Rendus* **1839,** 9, 7.

4.      Pochettino, A. *Acad. Lincei Rend.* **1906,** 15.

5.      Volmer, M. *Ann. Physik* **1913,** 40, 775.

6.      Einstein, A. *Annalen der Physik* **1905,** 322, (6), 132-148.

7.      Chapin, D. M.; Fuller, C. S.; Pearson, G. L. *Journal of Applied Physics* **1954,** 25, (5), 676-677.

8.      Gunawan, O.; Wang, K.; Fallahazad, B.; Zhang, Y.; Tutuc, E.; Guha, S. *Progress in Photovoltaics: Research and Applications* **2011,** 19, (3), 307-312.

9.      Würfel, P., *Physics of Solar Cells: From Basic Principles to Advanced Concepts*. 1 ed.; John Wiley & Sons: 2009 p256.

10.     Gregg, B. A.; Hanna, M. C. *Journal of Applied Physics* **2003,** 93, (6), 3605-3614.

11.     Nunzi, J.-M. *C. R. Physique* **2002,** 3, 20.

12.     Günes, S.; Neugebauer, H.; Sariciftci, N. S. *Chemical Reviews* **2007,** 107, (4), 1324-1338.

13.     Chiguvare, Z.; Dyakonov, V. *Physical Review B* **2004,** 70, (23), 235207.

14.     Coakley, K. M.; McGehee, M. D. *Chemistry of Materials* **2004,** 16, (23), 4533-4542.

15.     Tengstedt, C.; Crispin, A.; Hsu, C. H.; Zhang, C.; Parker, I. D.; Salaneck, W. R.; Fahlman, M. *Organic Electronics* **2005,** 6, (1), 21-33.

16.     Chen, L.-M.; Xu, Z.; Hong, Z.; Yang, Y. *Journal of Materials Chemistry* **2010,** 20, (13), 2575-2598.

17.     Luther, J. M.; Law, M.; Beard, M. C.; Song, Q.; Reese, M. O.; Ellingson, R. J.; Nozik, A. J. *Nano Letters* **2008,** 8, (10), 3488-3492.

18.     Loutfy, R. O.; Sharp, J. H. *The Journal of Chemical Physics* **1979,** 71, (3), 1211-1217.

19.     Scharber, M. C.; Mühlbacher, D.; Koppe, M.; Denk, P.; Waldauf, C.; Heeger, A. J.; Brabec, C. J. *Advanced Materials* **2006,** 18, (6), 789-794.

20.     Brabec, C. J.; Cravino, A.; Meissner, D.; Sariciftci, N. S.; Fromherz, T.; Rispens, M. T.; Sanchez, L.; Hummelen, J. C. *Advanced Functional Materials* **2001,** 11, (5), 374-380.

21.     van□Duren, J. K. J.; Yang, X.; Loos, J.; Bulle-Lieuwma, C. W. T.; Sieval, A. B.; Hummelen, J. C.; Janssen, R. A. J. *Advanced Functional Materials* **2004,** 14, (5), 425-434.

22.     Mihailetchi, V. D.; Blom, P. W. M.; Hummelen, J. C.; Rispens, M. T. *Journal of Applied Physics* **2003,** 94, (10), 6849-6854.

23.     Ko, S.; Hoke, E. T.; Pandey, L.; Hong, S.; Mondal, R.; Risko, C.; Yi, Y.; Noriega, R.; McGehee, M. D.; Brédas, J.-L.; Salleo, A.; Bao, Z. *Journal of the American Chemical Society* **2012,** 134, (11), 5222-5232.

24.     Yang, J.; Tang, A.; Zhou, R.; Xue, J. *Solar Energy Materials and Solar Cells* **2011,** 95, (2), 476-482.

25.     Graetzel, M.; Janssen, R. A. J.; Mitzi, D. B.; Sargent, E. H. *Nature* **2012,** 488, (7411), 304-312.

26.     Chen, H.-Y.; Hou, J.; Zhang, S.; Liang, Y.; Yang, G.; Yang, Y.; Yu, L.; Wu, Y.; Li, G. *Nat Photon* **2009,** 3, (11), 649-653.

27.     Lim, B.; Jo, J.; Na, S.-I.; Kim, J.; Kim, S.-S.; Kim, D.-Y. *Journal of Materials Chemistry* **2010,** 20, (48), 10919-10923.

28.     Street, R. A. *Applied Physics Letters* **2008,** 93, (13), 133308.

29.     Kim, M.-S.; Kim, B.-G.; Kim, J. *ACS Applied Materials & Interfaces* **2009,** 1, (6), 1264-1269.

30.     Gupta, D.; Mukhopadhyay, S.; Narayan, K. S. *Solar Energy Materials and Solar Cells* **2010,** 94, (8), 1309-1313.

31.     Guerrero, A.; Ripolles-Sanchis, T.; Boix, P. P.; Garcia-Belmonte, G. *Organic Electronics* **2012,** 13, (11), 2326-2332.

32.     Tang, C. W.; Albrecht, A. C. *The Journal of Chemical Physics* **1975,** 62, (6), 2139-2149.

33.     Ghosh, A. K.; Feng, T. *Journal of Applied Physics* **1978,** 49, (12), 5982-5989.

34.     Tang, C. W. *Applied Physics Letters* **1986,** 48, (2), 183-185.

35.     Maennig, B.; Drechsel, J.; Gebeyehu, D.; Simon, P.; Kozlowski, F.; Werner, A.; Li, F.; Grundmann, S.; Sonntag, S.; Koch, M.; Leo, K.; Pfeiffer, M.; Hoppe, H.; Meissner, D.; Sariciftci, N. S.; Riedel, I.; Dyakonov, V.; Parisi, J. *Applied Physics A: Materials Science & Processing* **2004,** 79, (1), 1-14.

36.     Li, G.; Shrotriya, V.; Huang, J.; Yao, Y.; Moriarty, T.; Emery, K.; Yang, Y. *Nat Mater* **2005,** 4, (11), 864-868.

37.     Chen, Y.; Li, F.; Shi, Y. *New Journal of Chemistry* **2012**.

38.     Huynh, W. U.; Dittmer, J. J.; Alivisatos, A. P. *Science* **2002,** 295, (5564), 2425-2427.

39.     Olson, J. D.; Gray, G. P.; Carter, S. A. *Solar Energy Materials and Solar Cells* **2009,** 93, (4), 519-523.

40.     Park, B.; Huh, Y. H.; Kim, M. *Journal of Materials Chemistry* **2010,** 20, (48), 10862-10868.

41.     Sariciftci, N. S.; Smilowitz, L.; Heeger, A. J.; Wudl, F. *Science* **1992,** 258, (5087), 1474-1476.

42.     Shaheen, S. E.; Brabec, C. J.; Sariciftci, N. S.; Padinger, F.; Fromherz, T.; Hummelen, J. C. *Applied Physics Letters* **2001,** 78, (6), 841-843.

43.     Lee, S.-H.; Kim, D.-H.; Kim, J.-H.; Lee, G.-S.; Park, J.-G. *The Journal of Physical Chemistry C* **2009,** 113, (52), 21915-21920.

44.     Dang, M. T.; Hirsch, L.; Wantz, G. *Advanced Materials* **2011,** 23, (31), 3597-3602.

45.     Yu, C.-Y.; Chen, C.-P.; Chan, S.-H.; Hwang, G.-W.; Ting, C. *Chemistry of Materials* **2009,** 21, (14), 3262-3269.

46.     Peng, Q.; Park, K.; Lin, T.; Durstock, M.; Dai, L. *The Journal of Physical Chemistry B* **2008,** 112, (10), 2801-2808.

47.     Wienk, M. M.; Turbiez, M.; Gilot, J.; Janssen, R. A. J. *Advanced Materials* **2008,** 20, (13), 2556-2560.

48.     Park, S. H.; Roy, A.; Beaupre, S.; Cho, S.; Coates, N.; Moon, J. S.; Moses, D.; Leclerc, M.; Lee, K.; Heeger, A. J. *Nat Photon* **2009,** 3, (5), 297-302.

49.     Zhou, Y.; Eck, M.; Kruger, M. *Energy & Environmental Science* **2010,** 3, (12), 1851-1864.

50.     Palaniappan, K.; Murphy, J. W.; Khanam, N.; Horvath, J.; Alshareef, H.; Quevedo-Lopez, M.; Biewer, M. C.; Park, S. Y.; Kim, M. J.; Gnade, B. E.; Stefan, M. C. *Macromolecules* **2009,** 42, (12), 3845-3848.

51.     Xu, T.; Qiao, Q. *Energy & Environmental Science* **2011,** 4, (8), 2700-2720.

52.     Fritz, K. P.; Guenes, S.; Luther, J.; Kumar, S.; Sariciftci, N. S.; Scholes, G. D. *Journal of Photochemistry and Photobiology A: Chemistry* **2008,** 195, (1), 39-46.

53.     Liu, Y.; Gibbs, M.; Puthussery, J.; Gaik, S.; Ihly, R.; Hillhouse, H. W.; Law, M. *Nano Letters* **2010,** 10, (5), 1960-1969.

54.     Lee, J.-S.; Kovalenko, M. V.; Huang, J.; Chung, D. S.; Talapin, D. V. *Nat Nano* **2011,** 6, (6), 348-352.

55.     Choi, J.-H.; Fafarman, A. T.; Oh, S. J.; Ko, D.-K.; Kim, D. K.; Diroll, B. T.; Muramoto, S.; Gillen, J. G.; Murray, C. B.; Kagan, C. R. *Nano Letters* **2012,** 12, (5), 2631-2638.

56.     Cho, K.-S.; Talapin, D. V.; Gaschler, W.; Murray, C. B. *Journal of the American Chemical Society* **2005,** 127, (19), 7140-7147.

57.      Greenham, N. C.; Peng, X.; Alivisatos, A. P. *Physical Review B* **1996,** 54, (24), 17628-17637.

58.      Xiaomei Jiang, R. D. S., Sergey B. Lee, Jeffrey M. Pietryga, Victor I. Klimov and Anvar A. Zakhidov   *Journal of Materials Research* **2007,** 22, 2204-2210

59.     Moon, S.-J.; Baranoff, E.; Zakeeruddin, S. M.; Yeh, C.-Y.; Diau, E. W.-G.; Gratzel, M.; Sivula, K. *Chemical Communications* **2011,** 47, (29), 8244-8246.

60.     Liu, C.-Y.; Holman, Z. C.; Kortshagen, U. R. *Nano Letters* **2008,** 9, (1), 449-452.

61.     Gur, I.; Fromer, N. A.; Chen, C.-P.; Kanaras, A. G.; Alivisatos, A. P. *Nano Letters* **2006,** 7, (2), 409-414.

62.     Zhao, D. W.; Sun, X. W.; Jiang, C. Y.; Kyaw, A. K. K.; Lo, G. Q.; Kwong, D. L. *Applied Physics Letters* **2008,** 93, (8), 083305.

63.     Janssen, A. G. F.; Riedl, T.; Hamwi, S.; Johannes, H.-H.; Kowalsky, W. *Applied Physics Letters* **2007,** 91, (7), 073519.

64.     Colsmann, A.; Junge, J.; Kayser, C.; Lemmer, U. *Applied Physics Letters* **2006,** 89, (20), 203506.

65.     Dou, L.; You, J.; Yang, J.; Chen, C.-C.; He, Y.; Murase, S.; Moriarty, T.; Emery, K.; Li, G.; Yang, Y. *Nat Photon* **2012,** 6, (3), 180-185.

66.     Dennler, G.; Prall, H.-J.; Koeppe, R.; Egginger, M.; Autengruber, R.; Sariciftci, N. S. *Applied Physics Letters* **2006,** 89, (7), 073502.

67.     http://www.nrel.gov/ncpv/images/efficiency_chart.jpg

68.     Tvingstedt, K.; Andersson, V.; Zhang, F.; Inganas, O. *Applied Physics Letters* **2007,** 91, (12), 123514.

**Chapter 2**

**Diketopyrrolopyrrole-Based Polymer for Photovoltaic Applications -**

**Functioning as Electron Donor with PCBM and Electron Acceptor with**

**P3HT**

**2.1 Introduction**

Organic photovoltaics (OPVs) continue to attract growing attention as candidates for the low-cost fabrication of high efficiency solar cells, to make future solar technology competitive with traditional energy resources[1-6]. The most promising and popular strategy is the design of bulk heterojunction (BHJ) OPVs with an active layer comprises a composite of a donor and an acceptor materials. The BHJ architecture requires the donor and acceptor materials to be tailored to provide: 1) strong and broad absorption of solar radiation, 2) a staggered energy level structure to drive charge separation, yet a large difference between the donor ionization energy and the acceptor electron affinity to maintain a large cell open circuit voltage, and 3) high hole and electron mobilities for facile charge collection. Here we adopted the strategy of designing a conjugated copolymer, which incorporates electron-rich donor and electron deficient acceptor segments that are linked by a bridging unit in the polymer backbone and applied it in the organic solar cell device. This structure provides an easy and efficient way to adjust the physical properties of the polymer by chemically modifying the donor, the acceptor and/or the linker group. Donor-acceptor copolymers are known for intrachain push-pull charge transfer, which has been used to synthesize more conjugated, lower band gap polymers having extended overlap with the solar spectrum[3, 7, 8]. However, materials with narrow bandgap sometimes suffer from low open circuit voltage ($V_{oc}$) arising from the reduction of the built-in potential between the Highest Occupied Molecular Orbital (HOMO) levels of the donor and Lowest Unoccupied Molecular Orbital (LUMO) of the acceptor. Fortunately, it is possible to adjust the aromaticity of the polymer, for instance,

by adjusting the linker group, to balance polymer absorption and $V_{oc}$ to optimize OPV performance[9, 10].

In this study, we have taken advantage of the recently developed diketopyrrolopyrrole (DPP) based polymer and designed a new conjugated copolymer (C12DPP-π-BT) containing the donor group bithiophene (BT) and the acceptor group 2,5-didodecylpyrrolo[3,4-c]pyrrole-1,4(2H,5H)-dione (C12DPP), bridged by a phenyl group (π). We chose electron rich bithiophene (BT) as the donor group because of its excellent electron donating ability and its electrochemical stability in PV devices[11]. For the choice of the acceptor group, the highly conjugated lactam planar structure of electron deficient diketopyrrolopyrrole (DPP) provides an idea building block, which results in strong π-π interactions for efficient charge transport. The first diketopyrrolopyrrole based polymer was reported by Yu[9, 12] group at University of Chicago and developed further by Tieke[13-15] group at University of Cologne. DPP has strong absorption in the visible spectrum and has been used as a donor material in the fabrication of BHJ OPVs in conjunction with PCBM[1, 8, 16, 17]. Its relatively low-lying HOMO and LUMO levels also make it a promising candidate as an acceptor material when blended with polymers possessing higher lying energy levels for application in hybrid solar cells[18]. To further optimize the energy levels, we chose a phenyl group instead of commonly used thiophene as the linker group to adjust the aromaticity to lower the HOMO level (to -5.4 eV) of the polymer. In addition, when the HOMO level lies well below the air oxidation threshold (-5.27 eV), it improves air stability[19]. We also introduce a dodecyl side group to increase the solubility of the polymer in common solvent systems to allow solution processability.

According to the literature, DPP containing polymers are used almost exclusively as an electron donor in photovoltaics[17, 20-23]. Janssen recently reported the application of DPP as acceptor materials in organic photovoltaics with the highest power conversion efficiency of 0.31%[18]. In comparison, by choosing the donor/acceptor pair and adjusting the linker group, the balanced conjugated structure of C12DPP-π-BT and the suitable HOMO/LUMO levels intermediate to the common electron donor (P3HT) and the electron acceptor (PCBM), offers this polymer unique property, so it may serve as either an electron donor or acceptor in blends with different semiconducting components to form efficient OPV devices. In this chapter we will explore the application of C12DPP-π-BT in OPV devices as well as OLED and transistor devices.

## 2.2 Experimental Section

### 2.2.1 Synthesis

All experiments were performed under nitrogen atmosphere by standard Schlenk techniques. THF was freshly distilled from sodium benzophenone under $N_2$ prior to use. After degassing with $N_2$ for 30 min, Pd(PPh$_3$)$_4$ (0.058 g, 0.05 mmol) was added to a stirred toluene solution (5 mL) of 3,6-bis(4-bromophenyl)-2,5-didodecylpyrrolo[3,4-c]pyrrole-1,4-dione (1, C12DPP-π-Br$_2$) (0.39 g, 0.5 mmol) and 5,5′-bis(trimethylstannyl)-2,2′-bithiophene (2) (0.25 g, 0.5 mmol). The reaction mixture was heated at 100 °C for 2 days under nitrogen. The raw product was precipitated with methanol and collected by filtration. The precipitate was dissolved in chloroform and filtered with Florisil® Adsorbent for Chromatography 60-100 mesh to remove the metal catalyst and inorganic

impurities. The final product C12DPP-$\pi$-BT was obtained by precipitating in methanol and washing with hexanes. Yield: 86%. $^1$H NMR (CDCl$_3$, 360 MHz): $\delta$ 0.86-0.88 (m, 6H, C-C$H_3$), 1.14-1.20 (m, 36H, C-C$H_2$), 1.58 (m, 4H, C-C$H_2$), 3.74 (m, 4H, N-C$H_2$), 6.98 (m, 2H, Th), 7.16 (m, 2H, Th), 7.40 (d, 4H, Ph), 7.62 (d, 4H, Ph). Gel permeation chromatographic (GPC) analysis: number-average molecular weight ($M_n$)= $5.88 \times 10^3$ g/mol, weight-average molecular weight ($M_w$) = $10.35 \times 10^3$ g/mol, and polydispersity index (PDI) = 1.76 (against polystyrene standard). A higher $M_n$ polymer was prepared using the same procedure as described for low $M_n$ C12DPP-$\pi$-BT, except that Pd$_2$(dba)$_3$/P($o$-tolyl)$_3$ was used instead of the Pd(PPh$_3$)$_4$ catalyst. Yield: 82%. GPC analysis: $M_n$ = $12.36 \times 10^3$ g/mol, $M_w$ = $17.68 \times 10^3$ g/mol, and PDI = 1.43 (against polystyrene standards).

All chemicals were purchased from Aldrich, Alfa Aesar, TCI, and used without further purification. Pd(PPh$_3$)$_4$,[24] 5,5′-bis(trimethylstannyl)-2,2′-bithiophene,[25, 26] and 3,6-Bis(4-bromophenyl)-2,5-didodecylpyrrolo[3,4-$c$]pyrrole-1,4-dione 1[27] were prepared according to literature procedures.

**2.2.2 Characterization**

$^1$H NMR spectra were recorded with a Bruker Avance (360 MHz) spectrometer. Molecular weights and polydispersity indices (PDIs) of the polymers were determined by gel permeation chromatography (GPC) analysis with a polystyrene standards calibration. Cyclic voltammograms were obtained employing a three electrode C3 cell stand and Epsilon electrochemical workstation (Bioanalytical Systems, Inc.). 0.01 M tetrabutylammonium hexafluorophosphate (TBAPF$_6$) was used as the supporting

electrolyte in acetonitrile. A platinum disk and platinum wire were selected as working and counter electrodes, respectively. A Ag/AgNO$_3$ (non-aqueous) electrode was used as the reference electrode. The redox couple ferrocene/ferrocenium ion (Fc/Fc$^+$) provided an external standard.

AFM (Atomic force microscopy) measurements were carried out using a Digital Instruments Multimode AFM operated in tapping mode. TEM (Transmission electron microscopy) images were obtained using a JEM-1400 (JEOL Ltd.).

Samples for both absorption and PL quenching experiments were made as spin-coated films of C12DPP-π-BT, P3HT, and C12DPP-π-BT:PCBM (weight ratio: 1:2) and C12DPP-π-BT:P3HT (weight ratio: 1:1) blends from chloroform solutions at 1500 rpm for 1 minute onto quartz substrates and annealed at 140°C for 20 minutes before measurement. Absorption spectra were measured using a Varian Cary 5000 UV-Vis-NIR spectrophotometer. Photoluminescence (PL) spectra were measured on a Fluorolog 3 spectrofluorometer (HORIBA Jobin Yvon, Ltd.) upon excitation at 550 nm.

Sample preparation for XRD measurement: Si/SiO$_2$ wafers were thoroughly cleaned by ultrasonication in acetone and isopropanol, rinsed with DI water, dried on a hot plate at 180°C for 30 min, and finally treated by UV-ozone for 30 min. 50 μL of pure C12DPP-π-BT solution (5 mg/mL), 50 μL of C12DPP-π-BT:PCBM blend solution (polymer: 5mg/mL; PCBM 10 mg/mL) were drop-cast from chloroform on the pre-cleaned silicon wafers and allowed to dry, followed by annealing at 140 °C for 20 minutes. XRD were performed using monochromatic CuKα beam radiation (wavelength: 0.154 nm) from a Rigaku SmartLab at 40 kV and 30 mA.

41

### 2.2.3 Fabrication and Characterization of Solar Cells

Polymer solar cells were fabricated on indium tin oxide (ITO) coated glass substrates (Delta Technologies, nominal coating thickness, 120-160 nm, sheet resistance, 5-15 $\Omega$/sq). The ITO on glass was first patterned by photolithography, thoroughly cleaned by ultrasonication in acetone and isopropanol, rinsed with DI water, dried on a hot plate at 180°C for 30 min, and finally treated by UV-ozone for 30 min. A 40 nm film of poly(3,4-ethylenedioxythiophene)/poly(styrene sulfonate) was deposited on the ITO by spin-coating from an aqueous PEDOT:PSS dispersion (PEDOT:PSS, Baytron P VP AI4083) at 2000 rpm in air. The PEDOT:PSS film was dried at 180°C for 20 min inside the $N_2$ glovebox. Subsequent processing steps were carried out in the $N_2$ glovebox. Either a C12DPP-$\pi$-BT:PCBM mixture (15mg/mL, weight ratio: 1:2) or a C12DPP-$\pi$-BT:P3HT (10mg/mL, weight ratio: 1:1) mixture was dissolved in chloroform, and in some cases 5 wt% diiodooctane was added to the C12DPP-$\pi$-BT:PCBM mixture. The blend solution was deposited by spin-coating on top of the PEDOT:PSS layer at 1500 rpm for one minute and then annealed at 140 °C for 20 min. The devices were transferred into the vacuum evaporation chamber and kept there for three hours under vacuum ($<10^{-6}$ Torr) prior to evaporating a back contact consisting of 1 nm LiF and 80 nm Al through shadow masks. The active device area of 9 mm$^2$ is defined by the overlapping area of the back LiF/Al contact and the front, lithographically pre-patterned, transparent, ITO contact.

Current-voltage characteristics of the photovoltaic cells were acquired using a Keithley 2400 source-meter under the illumination of AM 1.5G solar simulated light (1 sun, 100

mW/cm$^2$, Oriel instruments Model 96000, Newport Co.) in air. A reference cell and meter (Model: 91150, Newport Co.) were used to calibrate the light intensity.

Spatially resolved measurements of solar cell short circuit current were collected for C12DPP-π-BT:PCBM (with and without the diiodooctane additive) and C12DPP-π-BT:P3HT devices. 488 nm light from an Innova 70C Spectrum Ar:Kr laser was focused to a spot size of 0.4 µm using a modified Olympus BH2 microscope to illuminate devices through the transparent ITO contact. Devices were mounted on a piezo–controlled stage (Max 301, Thor Labs Nanomax) for photocurrent mapping. Local photocurrent data were acquired in 0.25 µm steps across 10 µm by 10 µm devices areas.

### 2.2.4 Fabrication and Characterization of Field Effect Transistors

FET device on Si substrate: Highly doped N-type Si wafers (100) ($\rho$<0.01 Ω-cm) with 250 nm thermally grown SiO2 were purchased from Si Inc. and served as the gate and gate dielectric layer of the field-effect transistors (FETs). Prior to device fabrication, the silicon wafers were cleaned by ultrasonication in acetone and isopropanol, rinsed with DI water, and subsequently dried on a hot plate at 100 °C for 5 min. The wafers were finally treated by UV-ozone for 20 min. The SiO$_2$ wafer surface was modified by octadecyltrichlorosilane (OTS) by placing the substrates in a Petri dish with a few drops of OTS in a separate dish in a vacuum desiccator, which was then evacuated for 4 minutes and placed on a hot plate at 120 °C for 3 hours. The wafers were thoroughly rinsed in isopropanol and then blown dry with N$_2$. The polymer and polymer blend was dissolved in chloroform (polymer:7 mg mL$^{-1}$; polymer:PCBM 1:2 1:4 weight ratio), filtered through a 0.2 µm PTFE syringe filter, and then spun at 1500 rpm for 60 s on the OTS-treated SiO$_2$/Si substrate. The devices were annealed at 140 °C for 20 minutes.

Finally, 20 nm Au source and drain electrodes were deposited by thermal evaporation through shadow masks to form top-contact, bottom-gate FETs with four different channel lengths (L): 30nm, 60nm, 90nm, and 120nm. The width to length ratio of the channels is 20 for all the devices.

Current-voltage characteristics of the polymer FETs were acquired using an Agilent 4156C semiconductor parameter analyzer in combination with a probe station mounted in a $N_2$ filled glove box.

### 2.2.5 Fabrication and Characterization of Organic Light Emitting Diode

Polymer LED were fabricated on thoroughly cleaned, and pre-patterned indium tin oxide (ITO) coated glass substrates (Delta Technologies, sheet resistance, 5-15 $\Omega$/sq). A 40 nm film of PEDOT:PSS film was deposited and dried at 180°C for 20 min inside the $N_2$ glovebox. Subsequent processing steps were carried out in the $N_2$ glovebox. C12DPP-$\pi$-BT was dissolved in chloroform (5-7mg/mL). The polymer solution was deposited by spin-coating on top of the PEDOT:PSS layer at 1500 rpm for one minute and then annealed at 140 °C for 20 min. The devices were transferred into the vacuum evaporation chamber and kept there for three hours under vacuum ($<10^{-6}$ Torr) prior to evaporating a back contact consisting of 1 nm LiF and 80 nm Al through shadow masks. The active device area of 9 mm$^2$ is defined by the overlapping area of the back LiF/Al contact and the front, lithographically pre-patterned, transparent, ITO contact.

Current-voltage characteristics of OLED devices were acquired using a Keithley 2400 source-meter under dark condition in air.

**2.2.6 Space Charge Limited Current (SCLC) Measurements**

For hole mobility measurements, devices were fabricated on photolithographically patterned ITO coated glass substrates, cleaned and coated with a 40 nm PEDOT:PSS film. Films of C12DPP-π-BT or P3HT were deposited by spin-coating followed by annealing. The same fabrication procedures were used as described above for solar cell fabrication, except 60 nm Pd back contacts were evaporated through shadow masks to characterize hole transport by SCLC measurements.

For electron mobility measurements, devices were fabricated on 2.5 cm x 2.5 cm glass slides, using the same cleaning procedures as for solar cells. 20 nm Al back contacts and 1 nm LiF and 60 nm Al front contacts were deposited by thermal evaporation. Films of C12DPP-π-BT or PCBM were similarly explored. Samples for hole and electron mobility measurements were fabricated side-by-side for comparison.

**2.2.7 Recombination Characterization by Photoconductivity Measurements**

On pre-cleaned quartz disks, 5 μm channel length, 75 μm channel width junctions were photolithographically defined and 1 nm Cr/19 nm Au was thermally evaporated to form bottom-contact, two-terminal devices for photoconductivity measurements. Films of C12DPP-π-BT, C12DPP-π-BT:PCBM (5 wt% diiodooctane added) and C12DPP-π-BT:P3HT were deposited by spin-casting from chloroform solutions. The devices were annealed at 140 °C for 20 minutes.

Photoconductivity measurements were performed in ambient air. The devices were illuminated by 488nm laser excitation from an Ar-Kr laser (Innova 70C Spectrum). Neutral-density filters were used to control excitation intensity. Bias voltage was applied and the photocurrent was recorded using a source-meter (Keithley model 2400).

## 2.3 Results and Discussion

### 2.3.1 Synthesis

Scheme 2.1 illustrates the synthetic procedure for the conducting polymer C12DPP-π-BT (poly 3-(4-(2,2'-bithiophen-5-yl)phenyl)-2,5-didodecyl-6-phenylpyrrolo[3,4-c]pyrrole-1,4(2H,5H)-dione) containing electron deficient C12DPP (2,5-didodecylpyrrolo[3,4-c]pyrrole-1,4(2H,5H)-dione) and electron rich bithiophene monomers, bridged by a phenyl group. 3,6-Bis(4-bromophenyl)-2,5-didodecylpyrrolo[3,4-*c*]pyrrole-1,4-dione (**1**, C12DPP-Br$_2$) was synthesized by a procedure similar to that of Tieke.[27] 5,5′-bis(trimethylstannyl)-2,2′-bithiophene (**2**) was reacted with 1 equivalent of **1** by Stille cross coupling in the presence of a catalytic amount of Pd(PPh$_3$)$_4$ in toluene to obtain C12DPP-π-BT. After work-up, a shiny light brown solid was acquired. GPC analysis indicates it has a $M_n$ of $5.88\times10^3$ g/mol, $M_w$ of $10.35\times10^3$ g/mol, and PDI of 1.76. Based on previous report, higher molecular weight conducting polymers are more favorable for the fabrication of efficient OPVs.[28] The catalyst system of Pd$_2$(dba)$_3$/P(*o*-tolyl)$_3$ was then adopted to yield C12DPP-π-BT material with doubled molecular weight - $M_n$ of $12.36\times10^3$ g/mol, $M_w$ of $17.68\times10^3$ g/mol, and polydispersity index (PDI) of 1.43. The low PDI of both polymers indicated a narrow distribution of individual molecular masses in these samples. Both polymers were readily soluble in common organic solvents such as toluene, chloroform and chlorobenzene.
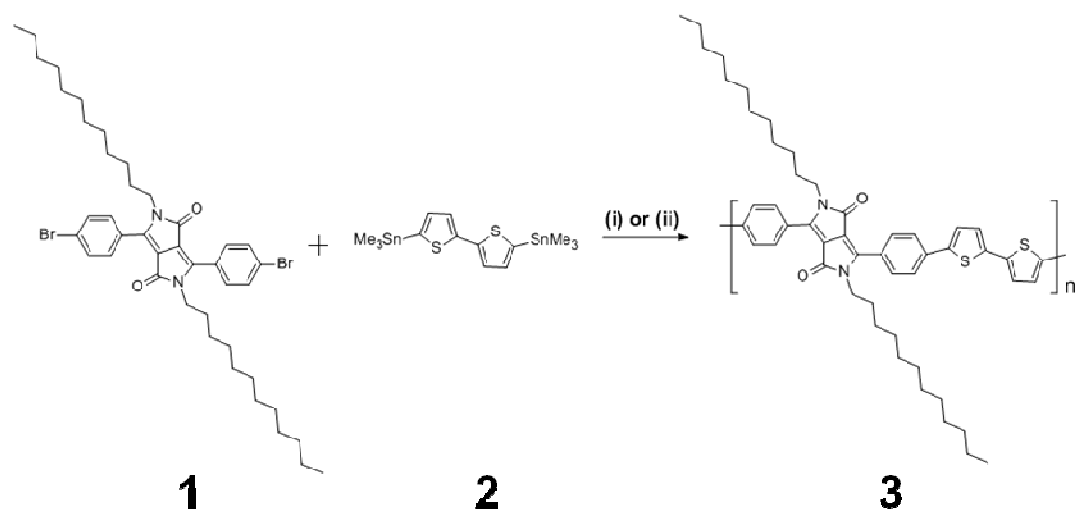
**Scheme 2.1**. Synthesis and structure of C12DPP-π-BT. (i) 0.05 mmol Pd(PPh$_3$)$_4$, toluene, 90 $^o$C for low molecular weight. (ii) 0.05 mmol Pd$_2$(dba)$_3$, 0.4 equiv of P(o-tolyl)$_3$, toluene, 90 $^o$C for high molecular weight.

### 2.3.2 Energy Level Measurements Using Cyclic Voltammetry Method

To achieve efficient charge separation and high conversion efficiency in a heterojuntion solar cell, the energy levels of the two components must be staggered and the energy difference between the ionization energy of the donor and the electron affinity of the acceptor must drive charge transfer of the photogenerated exciton and provide a sufficient built-in potential to attain a high open circuit voltage (V$_{oc}$).[29-31] Electrochemical measurements were used to study the electronic structure of C12DPP-π-BT, and to characterize the alignment of its energy levels relative to common organic photovoltaic materials used in bulk heterojunction devices: the electron donor P3HT and the electron acceptor PCBM. Figure 2.1(a-d) shows cyclic voltammograms collected for drop cast films of (a) high and (b) low M$_n$ C12DPP-π-BT, (c) PCBM and (d) P3HT on a platinum

47

working electrode. The potentials were recorded against the oxidation peak of ferrocene/ferrocenium (Fc/Fc$^+$) redox couple, which has a reported HOMO energy level of –4.8 eV and served as an external standard in our system[32]. Based on the onset of the oxidation peak at 0.6 V and reduction peak at -1.3 V of both low and high $M_n$ C12DPP-$\pi$-BT, we estimated the HOMO and LUMO levels of C12DPP-$\pi$-BT to be -5.4 eV and -3.5 eV, respectively. Similarly, from the cyclic voltammograms in Figure 2.1(c,d), we estimated the HOMO/LUMO energy levels of PCBM and P3HT to be -6.3 eV/-3.8 eV and -5.1 eV/-3.1 eV, respectively. The HOMO/LUMO levels for PCBM and P3HT are in agreement with literature reported values[33, 34]. The electrochemical bandgap, calculated from the difference between the HOMO and LUMO energies, is 1.9 eV for both the high and low $M_n$ polymers. The electrochemical bandgaps are consistent with the optical band gaps of 1.8 eV for both polymers, calculated from the onset in optical absorptions, described in detail in the next section. The 0.1 eV (1.9 eV-1.8 eV) measured difference between the electrochemical bandgap and the optical bandgap reflects the influences of solvents, ions, and surface effects present in electrochemical measurements and influence of Coulomb binding energy of the exciton present in optical absorption spectroscopy[35]. The results are summarized in Table 2.1.
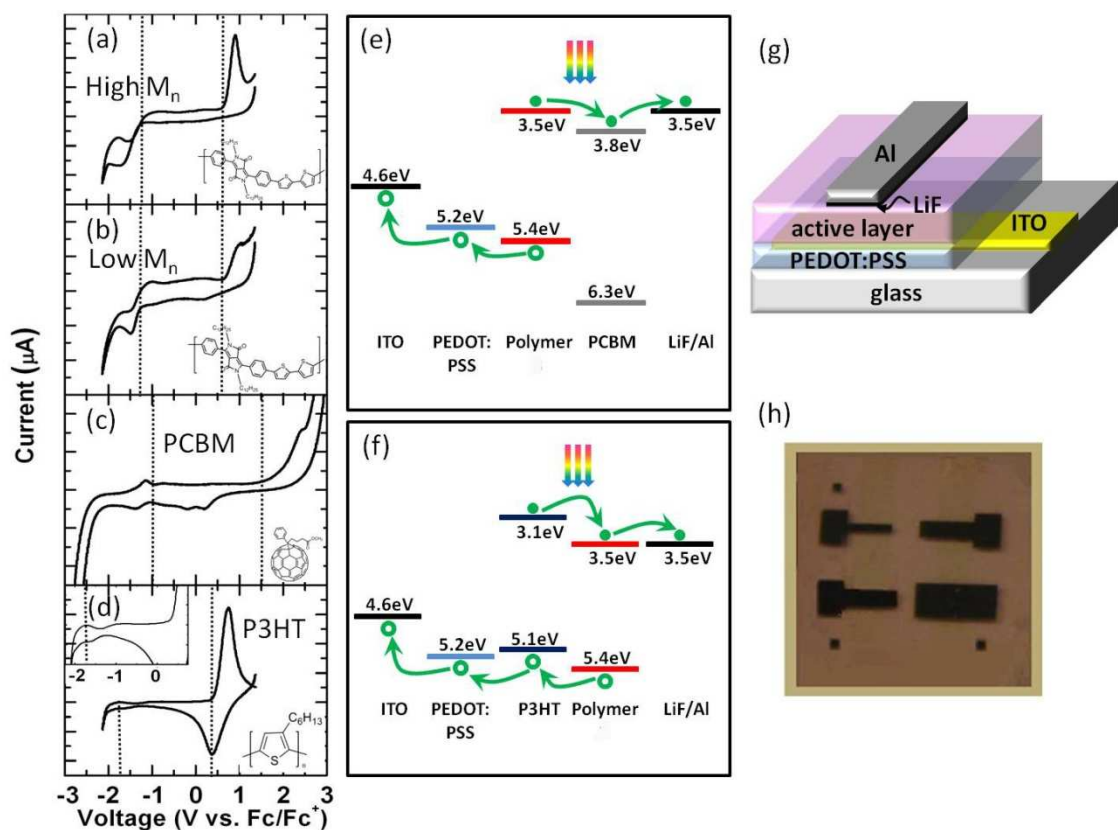
**Figure 2.1**. Cyclic voltammograms, energy level alignment of active layer components and schematic and optical micrographs of polymer photovoltaic devices. Cyclic voltammograms of (a) high $M_n$ C12DPP-$\pi$-BT, (b) low $M_n$ C12DPP-$\pi$-BT, (c) PCBM and (d) P3HT films on a platinum working electrode in an acetonitrile solution of 0.01 M TBAPF$_6$ at a scan rate of 50 mV/s. Redox couple ferrocene/ferrocenium (Fc/Fc$^+$) was used as an external standard. (e,f) Energy level alignment of active layer components derived from cyclic voltammograms and electrode materials from literature reported values, in reference to vacuum. (g,h) Schematic and optical micrographs of polymer photovoltaic devices.

49

**Table 2.1**. Optical and Electrochemical Properties of the C12DPP-π-BT, P3HT and PCBM

| | UV - Vis Absorption | | | | Cyclic Voltammetry | | |
| | solution | film | | | p-doping | n-doping | |
| Composites | $\lambda_{max}$ (nm) | $\lambda_{max}$ (nm) | $\lambda_{onset}$ (nm) | $E_g^{opt}$ (eV) | $E_{on}^{ox}$/HOMO (V)/(eV) | $E_{on}^{red}$/LUMO (V)/(eV) | $E_g^{EC}$ (eV) |
|---|---|---|---|---|---|---|---|
| High $M_n$ C12DPP-π-BT | 557 | 580 | 690 | 1.80 | 0.6 eV/-5.4eV | -1.3 eV/-3.5eV | 1.9 |
| Low $M_n$ C12DPP-π-BT | 548 | 580 | 690 | 1.80 | 0.6 eV/-5.4eV | -1.3 eV/-3.5eV | 1.9 |
| P3HT | 450 | 525 | 650 | 1.91 | 0.3 eV/-5.1eV | -1.7eV/-3.1eV | 2.0 |
| PCBM | | | | | 1.5 eV/-6.3eV | -1.0 eV/-3.8eV | 2.5 |

\* PCBM film has a broad absorption in the visible region (350–750 nm) without a distinguishable peak.

Figure 2.1(e,f) shows the schematic of the energy level diagram constructed from the reported work functions of electrode materials LiF/Al and ITO/PEDOT:PSS,[36, 37] and the HOMO and LUMO energies derived from cyclic voltammograms for C12DPP-π-BT, PCBM and P3HT. The energy level alignment is critical to the success of bulk heterojunction solar cell fabrication. It should suffice 1) formation of a staggered type II heterojunction between two materials to allow electron and hole transport within different material to avoid recombination loss 2) offering sufficient LUMO offsets since empirically, the LUMO offset should be equal or larger than 0.3 eV to overcome the binding energy of exciton to separate the electron and hole efficiently, 3) providing large built-in potential. As generally accepted, built-in potential is directly related to the theoretical maximum value of open circuit voltage, which can be estimated by the energy difference between the HOMO level of the donor and LUMO level of the acceptor (or equivalently the energy difference between the ionization potential of the donor and the

electron affinity of the acceptor) [29]. As shown in Figure 2.1 (e,f), the HOMO and LUMO of C12DPP-π-BT are higher compared with those for PCBM, which indicates C12DPP-π-BT serving as an electron donor in C12DPP-π-BT:PCBM blends, while in contrast, the HOMO and LUMO of C12DPP-π-BT lies below those of P3HT, which suggests that C12DPP-π-BT can act as an electron acceptor in C12DPP-π-BT:P3HT blends. The LUMO offsets in C12DPP-π-BT:PCBM and C12DPP-π-BT:P3HT system are 0.3 eV and 0.4 eV, respectively, which offers substantial potential drop for sufficient charge transfer and separated effectively at the interface between C12DPP-π-BT and either P3HT or PCBM[38, 39]. In addition, C12DPP-π-BT exhibits a larger built-in potential (1.6 eV) whether blended to form an acceptor with P3HT or blended to form a donor with PCBM [Table 2.1, Figure 2.1(e,f)]. This value is much larger than the extensively studied system P3HT:PCBM with built-in potential of 0.7-1.3 eV (calculated from the reported ranges for the HOMO level of P3HT and the LUMO level of PCBM) [24, 38, 40]. Therefore, it should provide potentially larger $V_{oc}$, which is critical to improve device performance. In conclusion, C12DPP-π-BT demonstrates the optimum HOMO and LUMO levels, which can form type II heterojunction with either PCBM or P3HT with sufficient exciton separation force and large built-in potential for high $V_{oc}$.

### 2.3.3 Optical Properties

The UV/Vis absorption spectra for both the pristine low $M_n$ and high $M_n$ C12DPP-$\pi$-BT, shown in Figure 2.2(a), exhibit the maximum absorption peaks at 580 nm with absorption onset around 690 nm. In comparison, the commonly used P3HT shows absorption peak at 525 nm with absorption onset around 650 nm. This result indicates that C12DPP-$\pi$-BT polymer can extend the absorption onset to the longer wavelength region than the most commonly used polymer P3HT, hence provide potentially better light utilization. Figure 2.2(b) shows the absorption spectra for the blends of C12DPP-$\pi$-BT:PCBM and C12DPP-$\pi$-BT:P3HT in film. The absorption of high $M_n$ C12DPP-$\pi$-BT mixture with PCBM is broader into the red region. The exact mechanism is not very clear yet. We hypothesize that this may be due to more effective packing of chains in the high $M_n$ polymer:PCBM blends than in the low $M_n$ polymer:PCBM blends[41, 42].

To study photoinduced charge transfer at donor-acceptor interface for both C12DPP-$\pi$-BT:PCBM and C12DPP-$\pi$-BT:P3HT system, PL quenching experiment was conducted[43]. It is worth noting that we measured both high and low $M_n$ polymers and they demonstrate the same characteristics. So here we only plotted the PL spectra for high $M_n$ polymer and corresponding polymer:PCBM and polymer:polymer blends for the simplicity of illustration. In Figure 2.2(c), the PL spectra of the pristine C12DPP-$\pi$-BT film and a blend of C12DPP-$\pi$-BT and PCBM showed that PL of the donor material C12DPP-$\pi$-BT is completely quenched when mixed with acceptor PCBM, indicating effective charge transfer between the two components. In contrast, in Figure 2.2(d), the PL spectra of P3HT and the C12DPP-$\pi$-BT:P3HT blended films show only partial quenching of PL of

the donor material P3HT. However, in the C12DPP-π-BT:P3HT system, the mechanism for PL quenching is more complicated because there exists two major competing relaxation process – electron transfer and energy transfer that can cause PL quenching in this system. In the polymer-polymer blend, the P3HT emission overlaps with the C12DPP-π-BT absorption in the spectral range of 600 nm to 700 nm. This spectral overlap may give rise to possible energy transfer from donor to acceptor. In this case, upon illumination, the excitation energy may be transferred from the exciton donor (in this case, P3HT) to the exciton acceptor (C12DPP-π-BT), which would decrease the luminescence of P3HT, and enhance the luminescence of C12DPP-π-BT (Figure 2.2(d)). Possible energy transfer from P3HT to C12DPP-π-BT provides a potentially competing pathway to charge separation in the polymer-polymer blend[44]. To include kinetics consideration, in polymer-polymer blends of C12DPP-π-BT:P3HT, energy transfer rate (~1 ps) is faster than charge transfer rate (~10s of ps) as reported in the literature[45]. The slower charge transfer is believed to be limited by larger donor-acceptor intermolecular distance caused by the solubilizing, long alkyl side chains, which can negatively affect charge transfer rate more dramatically than energy transfer[45]. As comparison, in polymer-PCBM blends, charge transfer rates are reported to be considerably faster (<ps) as the small size of PCBM is anticipated to allow the acceptor to more closely approach the main polymer chain (donor)[45, 46]. In conclusion, from the optical measurement result and kinetic aspects of photoinduced energy and electron transfer processes, we hypothesize that efficient charge transfer dominates in C12DPP-π-BT:PCBM system, while both charge transfer and energy transfer exists in C12DPP-π-BT:P3HT system.
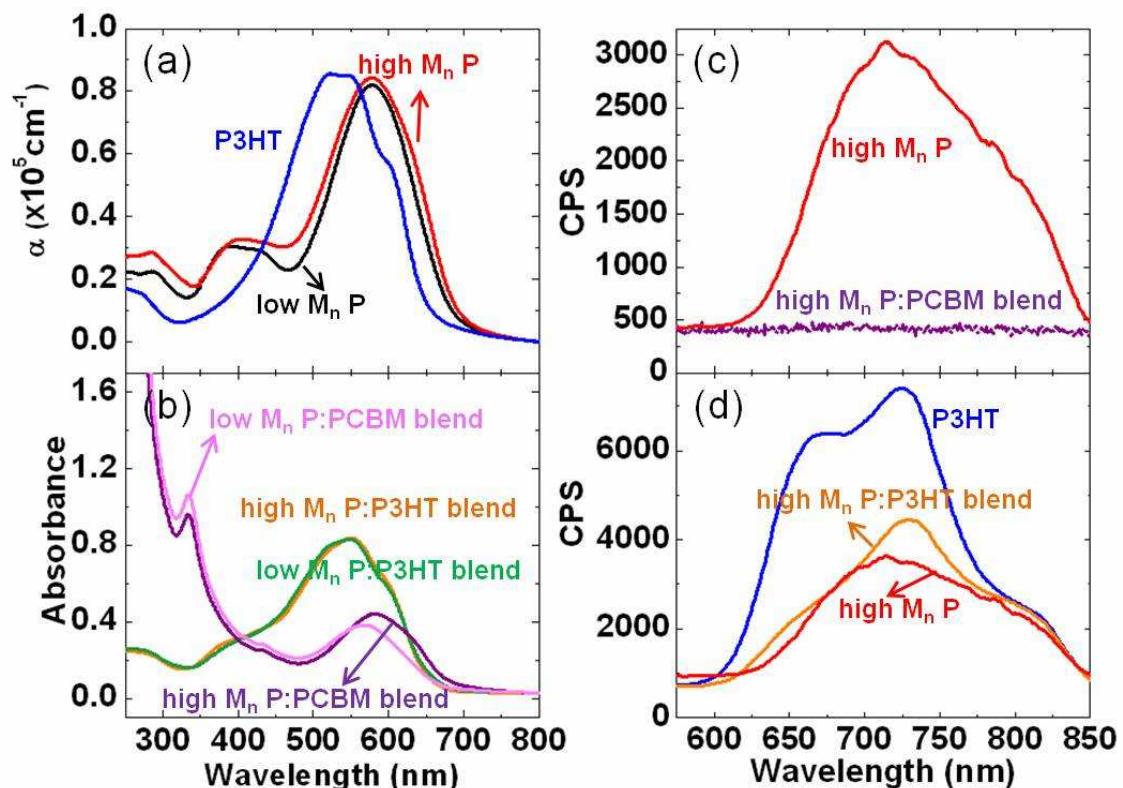
**Figure 2.2.** UV-Vis absorption spectra and photoluminescence spectra: (a) UV-Vis absorption spectra of pristine high (red line), low (black line) $M_n$ C12DPP-$\pi$-BT and P3HT (blue line) in thin films. (b) UV-Vis absorption spectra of high $M_n$ C12DPP-$\pi$-BT:PCBM (weight ratio 1:2) (purple line), low $M_n$ C12DPP-$\pi$-BT:PCBM (weight ratio 1:2) (pink line), high $M_n$ C12DPP-$\pi$-BT:P3HT (weight ratio 1:1) (orange line), low $M_n$ C12DPP-$\pi$-BT:P3HT (weight ratio 1:1) (green line) in thin films. (c) The photoluminescence of pristine high $M_n$ C12DPP-$\pi$-BT thin film (red line) is completely quenched in the presence of PCBM shown by the photoluminescence from high $M_n$ C12DPP-$\pi$-BT:PCBM (weight ratio 1:2) thin film (purple line). (d) The photoluminescence of pristine P3HT thin film (blue line) is partially quenched in the

presence of C12DPP-$\pi$-BT (red line) shown by the photoluminescence from high $M_n$ C12DPP-$\pi$-BT:P3HT (weight ratio 1:1) thin film (orange line).

### 2.3.4 X-ray Diffraction (XRD) Studies

To monitor the crystallinity change of C12DPP-$\pi$-BT before and after blending with PCBM and P3HT and explore the interaction between different components, x-ray diffraction (XRD) studies of pure C12DPP-$\pi$-BT and the two blends have been conducted (Figure 2.3). High $M_n$ polymer and blends are used here for demonstration. Low $M_n$ polymer exhibited the same trend of crystallinity change. For C12DPP-$\pi$–BT alone, XRD reveal a strong (100) diffraction peak intensity around $2\theta = 4.3°$ indicating good semi-crystallinity for the pure polymer films. After blending with PCBM or P3HT, a dramatic decrease of the peak intensity was observed, which indicates reductions in polymer crystallinity[42]. In addition, the interlayer distance (d1 spacing) for pure C12DPP-$\pi$–BT is 20.3 Å, which increased to 26.0 Å after blending with PCBM, implying PCBM disrupted the interlayer ordering. In contrast, C12DPP-$\pi$-BT:P3HT blends showed a decreased interlayer distance of 17.0 Å, which could be attributed to the short hexyl side chain of P3HT and this peak represents the average of C12DPP-$\pi$–BT (100) diffraction peak and P3HT (100) diffraction peak[47]. The peaks at higher angles ((010) diffraction peak) reveal small $\pi$–$\pi$ stacking distance between polymer backbones, 4.9 Å for pure C12DPP-$\pi$–BT, 4.6 Å for C12DPP-$\pi$-BT/PCBM, and 5.5 Å for C12DPP-$\pi$-BT:P3HT, indicating strong intermolecular interaction. We noticed a negative correlation of interlayer distance and $\pi$–$\pi$ stacking distance. This phenomena could be attributed to the unfavorable straightening

of side chains (increase of d-spacing), when $\pi$–$\pi$ stacking is closer. In conclusion, pristine C12DPP-$\pi$-BT polymer showed good semi-crystallinity, which was disrupted after blending with either PCBM or P3HT. And comparing the two blends, C12DPP-$\pi$-BT:PCBM exhibited a closer $\pi$–$\pi$ stacking, which is more favorable for charge transport along the stacking direction[48].
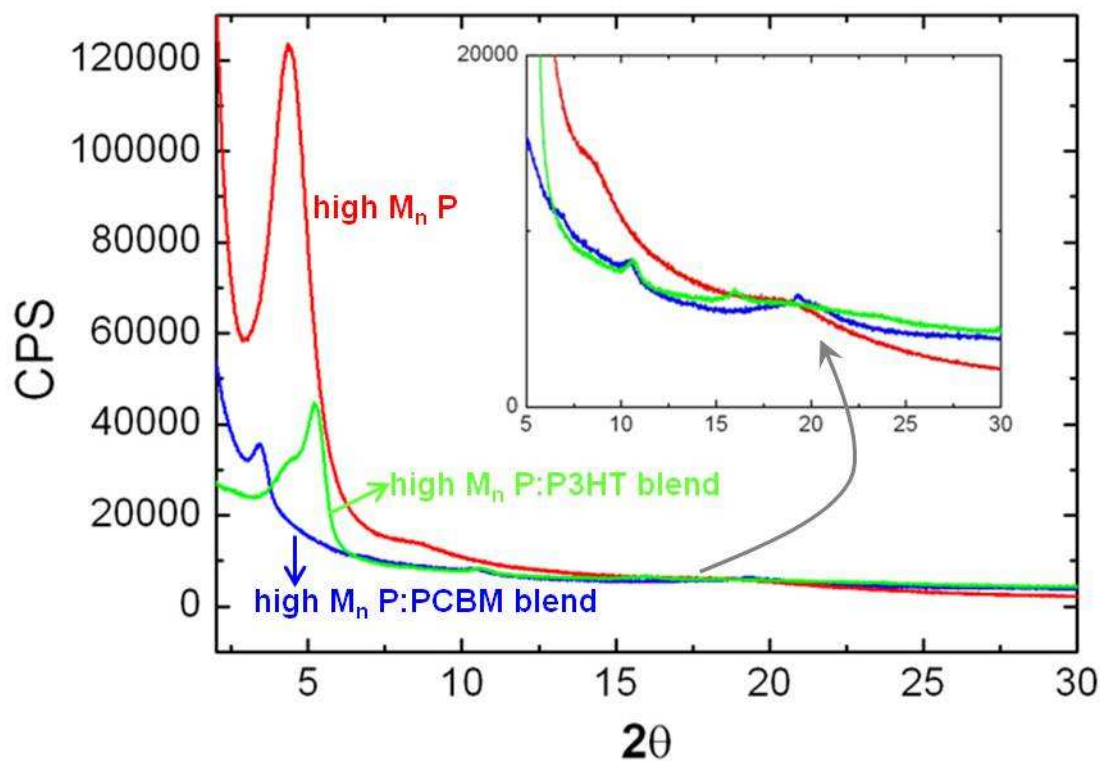


**Figure 2.3.** XRD analysis of C12DPP-$\pi$-BT before and after blending. Shown in the figure are XRD patterns of high $M_n$ C12DPP-$\pi$-BT (red line), high $M_n$ C12DPP-$\pi$-BT:PCBM (blue line) and high Mn C12DPP-$\pi$-BT:P3HT (green line).

### 2.3.5 Optimizing C12DPP-π-BT:PCBM Blend Intermixing Using Diiodooctane as Additive

The control over mixing of the different components in the blended films is crucial for bulk heterojunction solar cell fabrication[49]. In order to effectively separate charge carriers, it is critical to structure the semiconductor to have a large area donor-acceptor interface spaced by distances less than the exciton diffusion length, which is typically 5-20 nm[50] for organic semiconductors. Several strategies have been used in this field to structure a favorable interpenetrated network, including: thermal annealing, chemical modification of the donor materials, and the use of additives to improve the miscibility of different components[51]. To improve C12DPP-π-BT:PCBM miscibility and prevent large-scale phase separation, we added a small amount (5 wt%) of diiodooctane as additive to the C12DPP-π-BT and PCBM mixture solution. Bulk heterojunction solar cells were fabricated and optimized with the device structure of ITO/PEDOT:PSS/C12DPP-π-BT:PCBM/LiF/Al, where PEDOT:PSS serves as a hole extraction layer, while LiF lowers the work function of Al and serves as an electron extraction layer[52]. The overall device efficiency increased significantly with enhancement on short circuit current ($I_{sc}$), open circuit voltage ($V_{oc}$) and fill factor (FF), comparing with the devices without the diiodooctane additive (Figure 2.4).
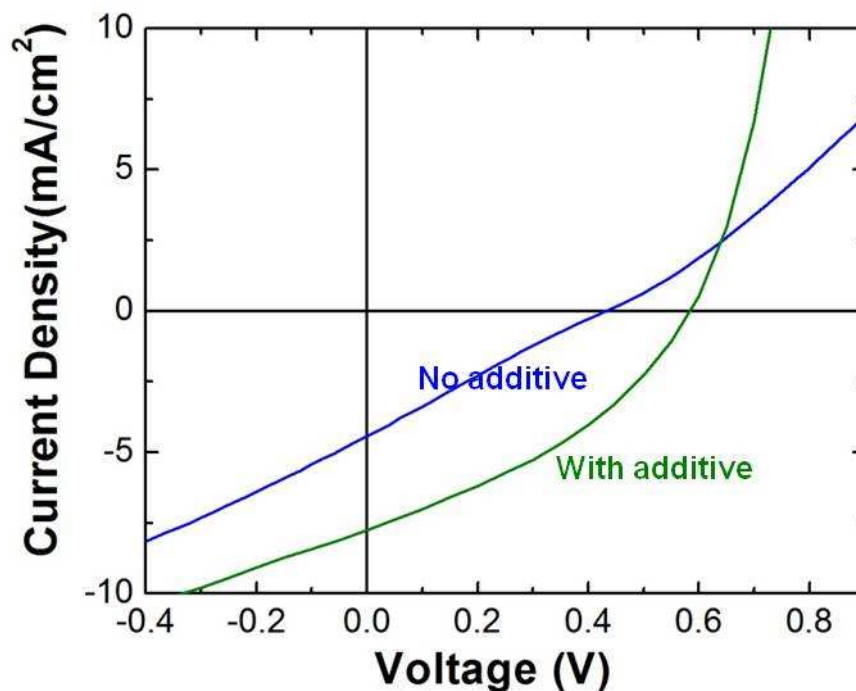
**Figure 2.4.** I-V curves of high $M_n$ C12DPP-π-BT:PCBM bulk heterojunction solar cells with (green line) and without (blue line) additives. Devices were annealed at 140°C for 20 minutes and measured under the illumination of AM 1.5G, 100 mW/cm$^2$

To further understand the effects of the additive and to quantify the uniformity of the devices, spatially resolved photoconductivity was used to map the $I_{sc}$ of solar cells through the transparent ITO back contact. For comparison between different devices, the recorded $I_{sc}$ was normalized to the maximum current in each device with the high current regions indicated by bright yellow and low current regions by black. As shown in Figure 2.5, for C12DPP-π-BT:PCBM devices, across the entire examined area (10 µm by 10 µm), the photocurrent maps obtained for devices (a) without any additive shows non-uniformities, whereas maps for devices (b) with the diiodooctane additive are significantly more uniform, consistent with a more homogeneous blend. The histogram of

the spatially resolved photocurrents for C12DPP-π-BT:PCBM cells without the diiodooctane additive (Figure 2.5(a)) revealed a broad and random distribution, consistent with our conclusion of more varied performance across the device area. Photocurrent histograms for high $M_n$ C12DPP-π-BT:PCBM devices with the additive (Figure 2.5(b)) showed a narrow quasi-normal distribution peaked at 95% of the photocurrent maximum value. All C12DPP-π-BT:P3HT devices, fabricated similarly, showed a very uniform photocurrent without any additive (Figure 2.5(c)), due to good miscibility of C12DPP-π-BT and P3HT, which may be a result of the presence of similar thiophene containing chemical structure in both polymers and their good solubility in the chloroform solvent[53, 54].
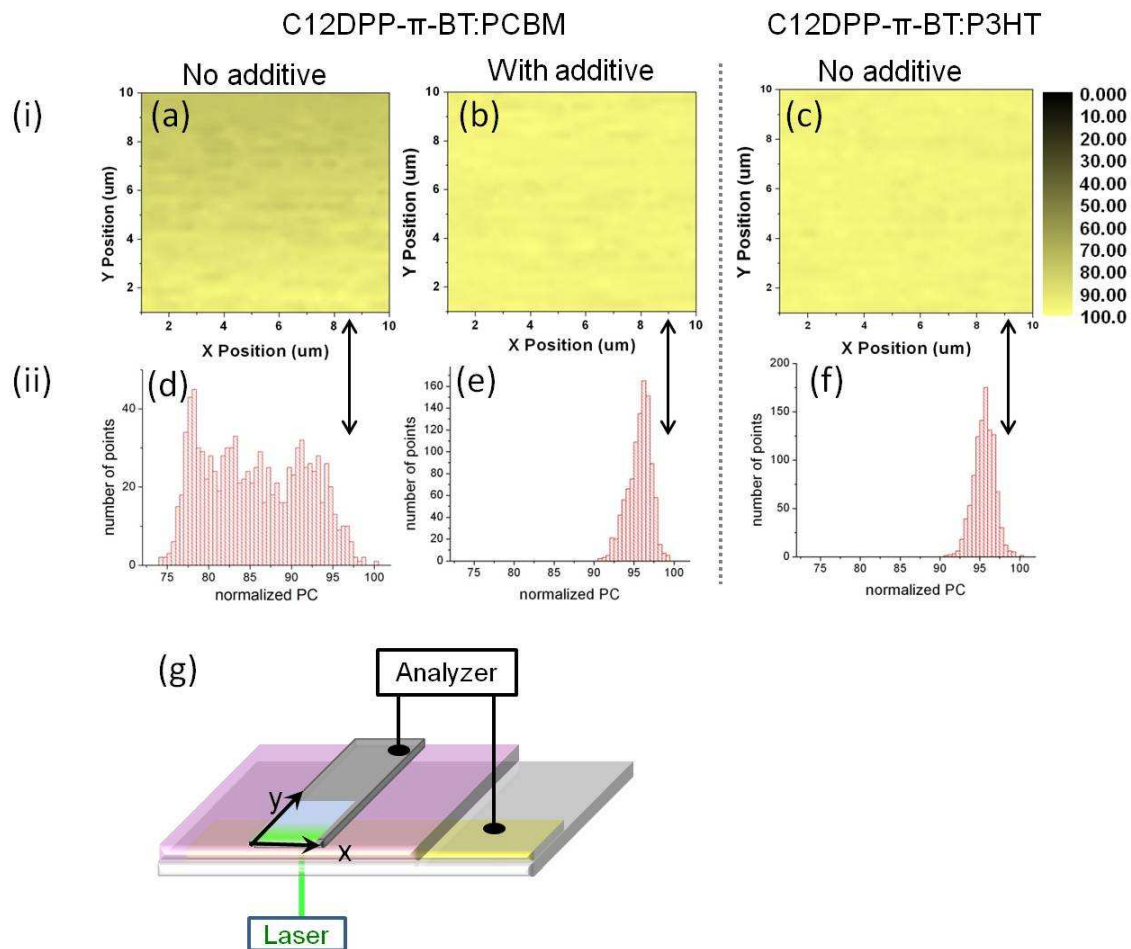
**Figure 2.5.** Spatially–resolved maps (i) and histograms (ii) of short circuit current: for high $M_n$ C12DPP-π-BT:PCBM solar cells (a,d) without additive, and (b,e) with the 5 wt% diiodooctane additive added to the active layer and for (c,f) high $M_n$ C12DPP-π-BT:P3HT device without additive. (g) Spatially-resolved photoconductivity measurement set-up (488 nm light from Ar:Kr laser was focused to a spot size of 0.4 µm to illuminate devices through the transparent ITO contact. Devices were mounted on a piezo–controlled stage for photocurrent mapping.)

### 2.3.6 Current-Voltage Characterization

Bulk heterojunction solar cells were fabricated and characterized with the device structure of ITO/PEDOT:PSS/C12DPP-π-BT:PCBM (or C12DPP-π-BT:P3HT)/LiF/Al. Diiodooctane was added to all the C12DPP-π-BT:PCBM blends in chloroform solution for better intermixing. Figure 2.6 shows the I-V curves of the devices with the best photovoltaic performance. We report and compare C12DPP-π-BT:PCBM blends with a weight ratio of 1:2 as we observed higher PCBM loadings gave better solar cell performance, consistent with the observation that higher PCBM loadings providing a more continuous pathway for electron transport[55]. The devices based on the high $M_n$ C12DPP-π-BT:PCBM demonstrated a high power conversion efficiency of 1.67% with $I_{sc}$ of 7.8 mA/cm$^2$ and $V_{oc}$ of 0.58 V. This is nearly a 50% improvement compared with the power conversion efficiency (1.12%) of the same polymer with a lower $M_n$, which had $I_{sc}$ of 6.4 mA/cm$^2$ and $V_{oc}$ of 0.50 V. On the basis of the measurements of four different devices made under the same fabrication conditions, the average efficiency for high and low $M_n$ polymer:PCBM devices is 1.53 and 1.03%, respectively. The best devices based on high $M_n$ C12DPP-π-BT:P3HT showed a moderate power conversion efficiency of 0.84% with $I_{sc}$ of 2.6 mA/cm$^2$ and $V_{oc}$ of 0.92 V, representing 15% efficiency enhancement over lower $M_n$ polyer:P3HT device (0.73% efficiency with $I_{sc}$ of 2.4 mA/cm$^2$ and $V_{oc}$ of 0.89 V).  The average efficiency for high and low $M_n$ polymer:P3HT devices is 0.76% and 0.62%, respectively, calculated for five different devices for each $M_n$. The statistics of device performance is summarized in Table 2.2.
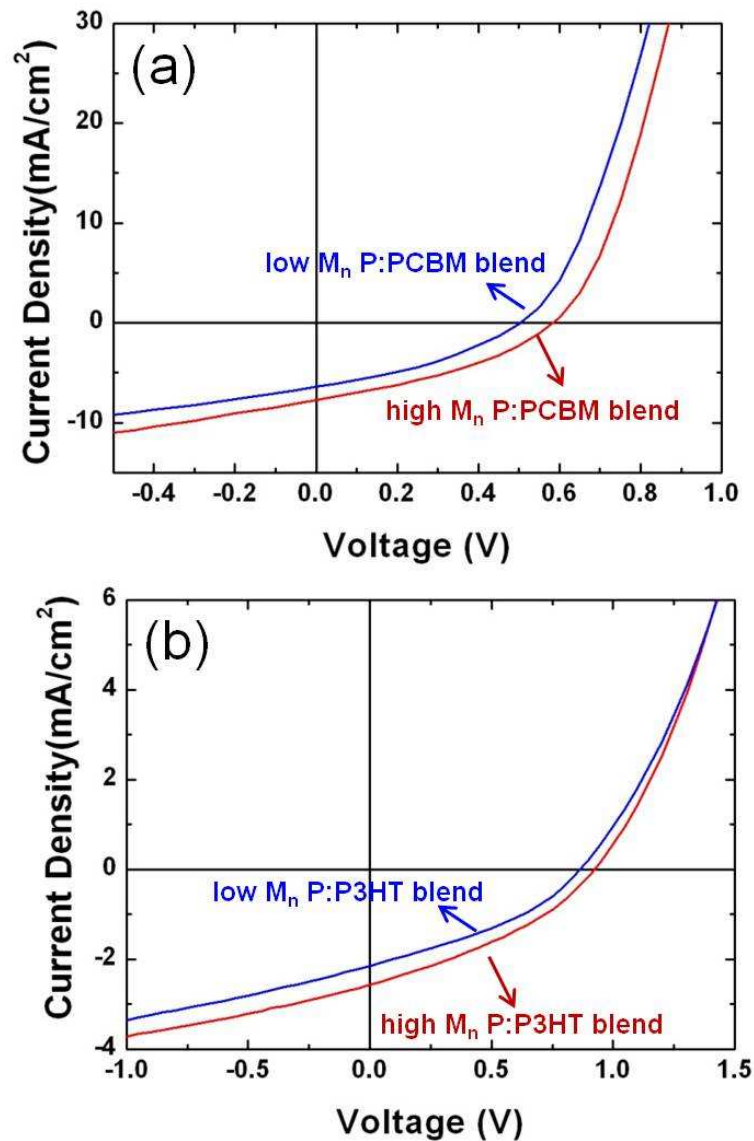
**Figure 2.6.** Current-voltage characteristics of C12DPP-π-BT containing BHJ solar cells. (a) C12DPP-π-BT:PCBM (weight ratio 1:2) bulk heterojunction solar cells with high (red) and low (blue) $M_n$ C12DPP-π-BT and (b) C12DPP-π-BT:P3HT (weight ratio 1:1) solar cells with high (red line) and low (blue line) $M_n$ C12DPP-π-BT under the illumination of AM 1.5, 100 mW/cm$^2$.

**Table 2.2**. Performance parameters of the C12DPP-π-BT:PCBM and C12DPP-π-BT:P3HT bulk solar cells, under AM 1.5G illuminations.

| Donor | Acceptor | | $I_{sc}$ (mA/cm$^2$) | $V_{oc}$ (V) | FF | Efficiency (%) |
|---|---|---|---|---|---|---|
| High $M_n$ P | PCBM | best | 7.8 | 0.58 | 0.37 | 1.67 |
| | | average | 7.2±0.6 | 0.58±0.01 | 0.37±0.01 | 1.53±0.15 |
| Low $M_n$ P | | best | 6.4 | 0.50 | 0.35 | 1.12 |
| | | average | 6.0±0.5 | 0.50±0.02 | 0.35±0.01 | 1.03±0.07 |
| P3HT | High $M_n$ P | best | 2.6 | 0.92 | 0.35 | 0.84 |
| | | average | 2.4±0.1 | 0.91±0.01 | 0.35±0.004 | 0.75±0.06 |
| | Low $M_n$ P | best | 2.4 | 0.89 | 0.34 | 0.73 |
| | | average | 2.1±0.3 | 0.88±0.02 | 0.34±0.01 | 0.62±0.09 |

In order to analyze the contribution of absorption at each wavelength to the photocurrent generation, the spectral response/incident photon conversion efficiency (IPCE) of the devices as a function of excitation energy was measured (Figure 2.7). The devices exhibit high external quantum efficiencies over 30% for the high $M_n$ C12DPP-π-BT:PCBM blends. The shape of IPCE curves matches the absorption spectra of the respective blends, which indicates light absorption being the dominant factor for the photocurrent. Similar results have been observed for diketopyrrolopyrrole-based polymer:PCBM blends spin-coated from chloroform solutions.[8] C12DPP-π-BT:P3HT devices maintain external quantum efficiency around 15% over a broad spectral range from 400 nm to 600nm, which indicates the high-energy spectral components contribute more significantly to the IPCE. We hypothesize this may indicate two polymers contribute differently to the photocurrent in C12DPP-π-BT:P3HT device. Although both

polymer can generate exciton, P3HT absorbs more in the shorter wavelength region than C12DPP-π-BT. Pure P3HT has a closer π–π stacking distance (3.8 Å)[56] than C12DPP-π-BT (4.9 Å) and shorter side chain, which may result in more facile charge transport in P3HT grain[57] and lead to a more significant contribution of P3HT than C12DPP-π-BT to photocurrent generation. The difference of charge recombination at different wavelength region may also play a role here although the mechanism is not quite clear.
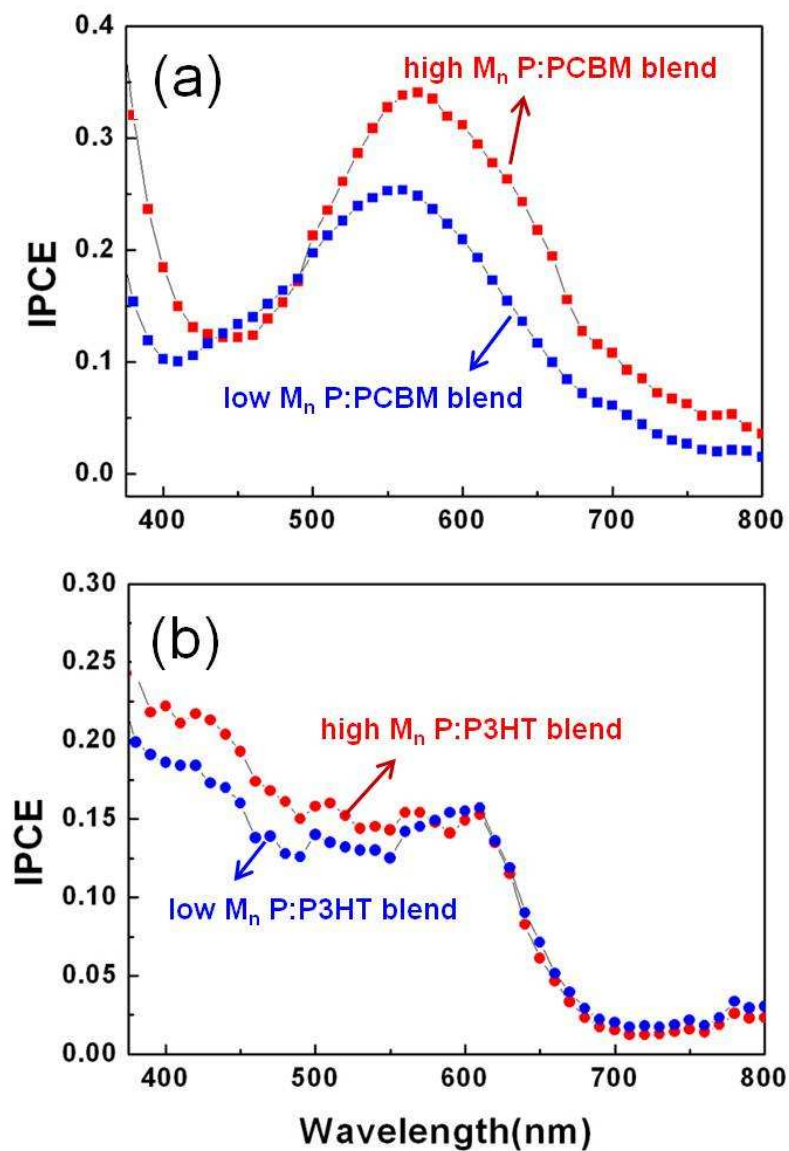
**Figure 2.7.** IPCE analysis: (a) IPCE of C12DPP-π-BT:PCBM (weight ratio 1:2) thin film solar cells for (red square) high $M_n$ and (blue square) low $M_n$ C12DPP-π-BT. (b) IPCE of C12DPP-π-BT:P3HT (weight ratio 1:1) thin film solar cells for (red circle) high $M_n$ and (blue circle) low $M_n$ C12DPP-π-BT.

**2.3.7 Space Charge Limited Current Measurements**

For the photovoltaic application, C12DPP-π-BT can function as either an electron donor when mixed with PCBM or an electron acceptor when blended with P3HT. To further confirm the ambipolar transport properties of C12DPP-π-BT, the hole and electron mobilities of the polymer were characterized by the space charge limited current (SCLC) model, which is a commonly used tool by checking the space charge limited current through the semiconductor in the dark in a sandwich structure[58, 59]. In order to investigate hole transport through the device, high work function electrodes ITO/PEDOT:PSS and palladium (Pd) were used to block electron injection. These electrodes form barriers to electron injection of 1.7 eV with C12DPP-π-BT. In contrast, for the electron mobility analysis, Al and LiF/Al were used as hole-blocking contacts with a hole injection barrier of 1.2 eV between polymer and the Al contact, and 1.9 eV between polymer and the LiF/Al contact. The current-voltage data are shown in Figure 2.8, fitted to the following equation[60, 61]:

$$J_{e(h)} = \frac{9}{8}\varepsilon\varepsilon_0\mu_{0e(h)}\exp(0.891\gamma_{e(h)}\sqrt{\frac{V}{d}})\frac{V^2}{d^3} \qquad (1)$$

where $\mu_{0e(h)}$ is the zero-field electron/hole mobility, $\gamma_{0e(h)}$ is the field activation factor, V is the applied potential and d is the thickness of the active layer. $\mu_{0e(h)}$ and $\gamma_{0e(h)}$ were evaluated by fitting the current-voltage characteristics. At room temperature, a zero-field hole mobility of $2.1 \times 10^{-4}$ cm$^2$/Vs and electron mobility of $4.7 \times 10^{-5}$ cm$^2$/Vs were obtained for the high $M_n$ C12DPP-π-BT only device. Similarly, a zero-field hole mobility of $4.2 \times 10^{-5}$ cm$^2$/Vs and electron mobility of $2.5 \times 10^{-5}$ cm$^2$/Vs were obtained for the low $M_n$

polymer only device. This indicates good charge transport for both electrons and holes with the hole transport slightly better than the electron. Also, high $M_n$ C12DPP-$\pi$-BT exhibits higher charge carrier mobility than low $M_n$ C12DPP-$\pi$-BT in either hole or electron. As a comparison, P3HT showed a hole mobility of $2.2\times10^{-5}$ cm$^2$/Vs, which is consistent with the literature reported value of $3\times10^{-5}$ cm$^2$/Vs[62].
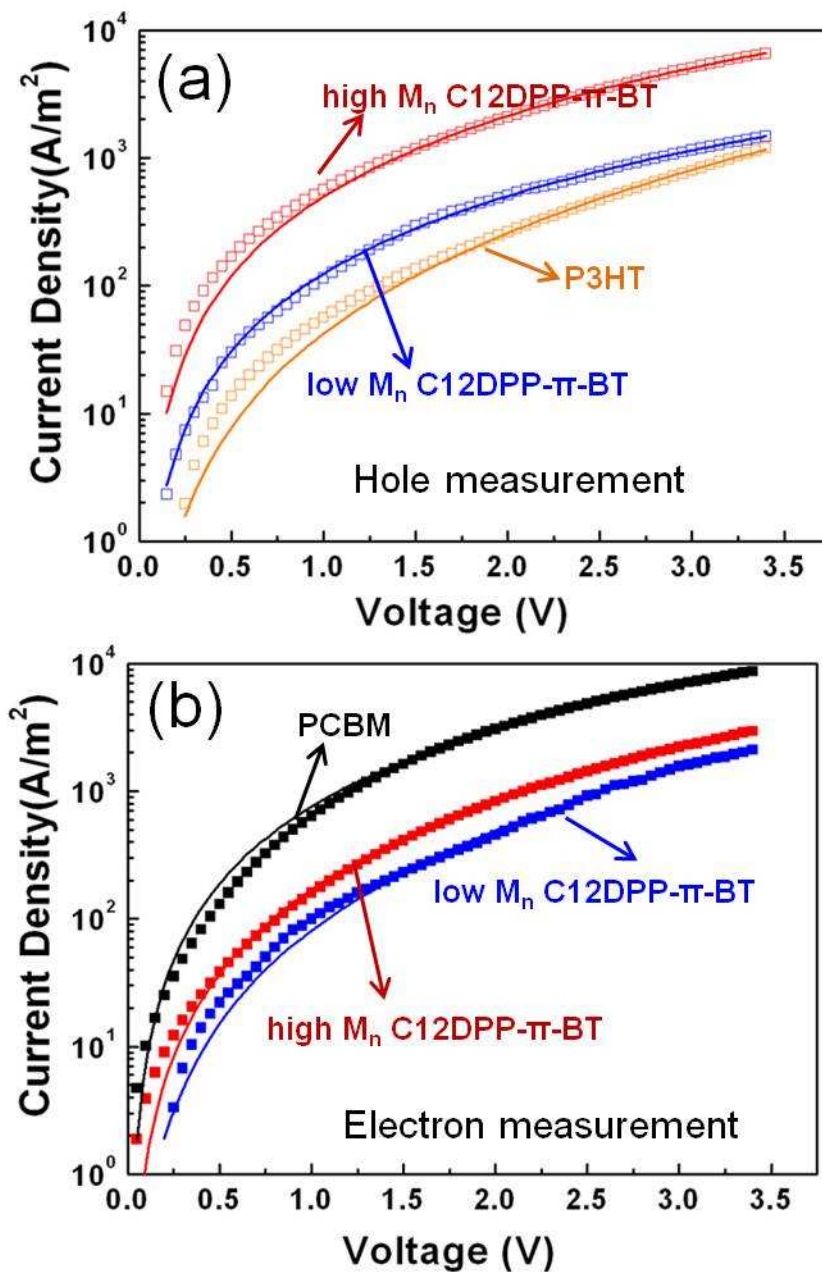
**Figure 2.8.** SCLC measurements: (a) hole mobility for high $M_n$ C12DPP-π-BT only thin films (red square), low $M_n$ C12DPP-π-BT only thin films (blue square), and P3HT (orange square) ; (b) electron mobility for high $M_n$ C12DPP-π-BT only thin films (filled red square), low $M_n$ C12DPP-π-BT only thin films (filled blue square), and PCBM (filled black square). Solid lines represent simulation results.

## 2.3.8 Morphological characterization by AFM

In addition to the optical and electrical characterization, the surface morphology of the blended films was also investigated by atomic force microscopy (AFM) to study the structural difference between high and low $M_n$ polymer blends (Figure 2.9). The morphology and phase images suggest that the higher $M_n$ polymer forms larger grains in either blends with PCBM or blends with P3HT, reducing the number of grain boundaries that may trap charges, and hence provides more facile pathways for carrier transport[28], which will effectively increase the short circuit current.
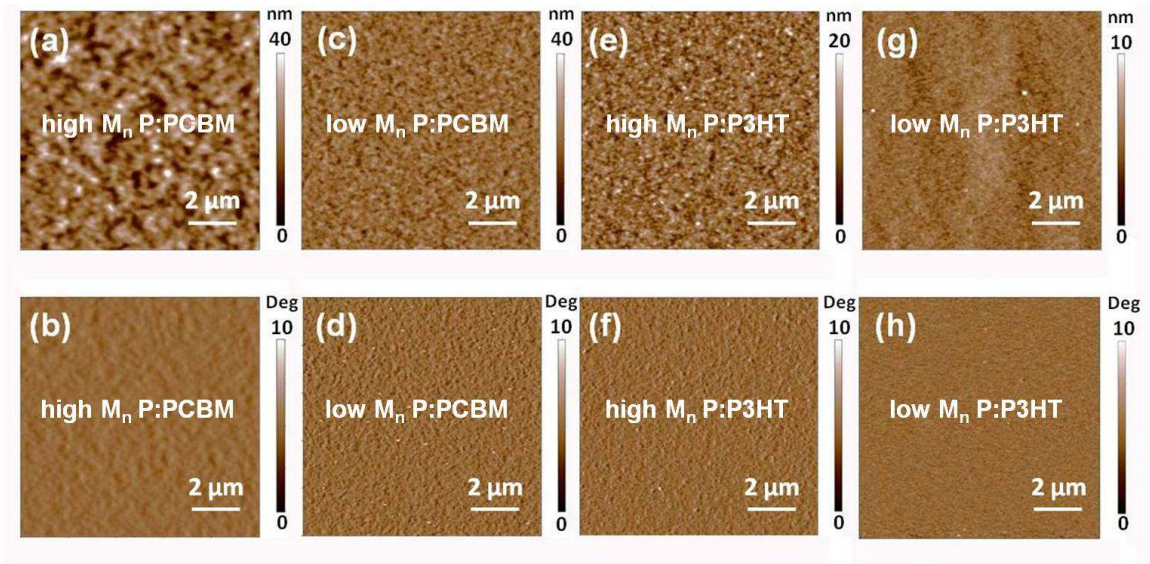


**Figure 2.9.** AFM topography (upper) and phase (lower) images: (a, b) high $M_n$ C12DPP-π-BT:PCBM (weight ratio 1:2) (c, d) low $M_n$ C12DPP-π-BT:PCBM (weight ratio 1:2), (e, f) high $M_n$ C12DPP-π-BT:P3HT (weight ratio 1:1), and (g, h) low $M_n$ C12DPP-π-BT:P3HT (weight ratio 1:1) with scan range (10µm by 10 µm). All samples were annealed at 140°C for 20 minutes.

**2.3.9 Photovoltaic Performance Discussion**

To briefly summarize, higher $M_n$ polymer displays higher efficiency for both C12DPP-π-BT:PCBM devices and C12DPP-π-BT:P3HT devices than lower $M_n$ polymer. The major contributor is more efficient charge carrier transport, which is revealed by SCLC measurements. And this enhancement on charge transport is consistent with AFM results (larger grain size for high $M_n$ polymer) and IPCE results (greater photocurrent generation for high $M_n$ polymer). Another factor is light absorption. In C12DPP-π-BT:PCBM blends, higher $M_n$ C12DPP-π-BT:PCBM absorbs further to the red as compared with low $M_n$ C12DPP-π-BT:PCBM mixture, which is reflected in a ~9% higher peak IPCE efficiency and the red extended IPCE spectrum extends.

Overall, devices based on C12DPP-π-BT:PCBM exhibits higher efficiency than C12DPP-π-BT:P3HT devices, which is attributed to the more effective charge transfer between C12DPP-π-BT and PCBM, as suggested by the PL quenching experiment.

It is interesting to point out that the C12DPP-π-BT:P3HT devices showed much higher $V_{oc}$ (~ 0.9 V) than C12DPP-π-BT:PCBM devices(~ 0.6 V), even though the built-in potentials calculated from electrochemical measurements are the same (1.6 eV) for both configurations. Although the reason for such difference is not exactly clear, in practice the obtainable $V_{oc}$ is always lower than the upper limit value derived from isolated materials characteristics and thermodynamic considerations because of electrode-active layer and donor-acceptor interfacial energetics and non-radiative recombination losses. Several possible reasons for the observed lower than theoretical (maximum) $V_{oc}$ (and the difference between C12DPP-π-BT:P3HT and C12DPP-π-BT:PCBM devices) include:

(1) The HOMO and LUMO are determined by electro-chemical method, which may not represent the precise energy levels when it is in solid film as mixture. Measurement influences of solvents, ions, and surface effects in electrochemical measurements, which play an important role for band alignment[63], are hard to quantify when derive the HOMO and LUMO value.

(2) Different interfacial dipoles may exist at the C12DPP-π-BT:PCBM and C12DPP-π-BT:P3HT interfaces, which can alter the effective Coulombic binding energy of the exciton and therefore affect the $V_{oc}$ of solar cells[64]. In addition, energy loss occurs when the electron transferred from donor LUMO to acceptor LUMO. The loss is estimated to be around 0.3 eV, empirically for polymer:PCBM heterojunction solar cells[38]. These factors might affect C12DPP-π-BT:PCBM and C12DPP-π-BT:P3HT differently.

(3) Non-Ohmic contact between active layer and electrodes will reduce the $V_{oc}$. In general, to maximize $V_{oc}$ for heterojunction solar cells, Ohmic contacts are preferred, imposing energy level alignment of the HOMO level of the electron donor with the Fermi level of the hole collecting PEDOT:PSS/ITO electrode and of the LUMO level of the electron acceptor with the Fermi level of the electron collecting LiF/Al electrode[65]. For the cathode side, a thin layer of LiF reduces the work function of Al from 4.2 eV to 3.5 eV,[37] aligning it with the LUMO levels for both PCBM and C12DPP-π-BT and forming Ohmic contacts. However, for the anode side, the PEDOT:PSS electrode has a work function of 5.1±0.2 eV[66]. The contact effects will limit the $V_{oc}$ if the donor polymer has a HOMO level more negative

than -5.3 eV versus vacuum[65]. In the case of C12DPP-$\pi$-BT:PCBM devices, the HOMO level of donor (C12DPP-$\pi$-BT) is -5.4 eV, which may form a non-Ohmic contact at the interface and hence lower the $V_{oc}$. In contrast, for the C12DPP-$\pi$-BT:P3HT system, the donor polymer P3HT has a HOMO level around -5.1 eV, which forms a suitable Ohmic contact with PEDOT:PSS electrode. Therefore energy loss is reduced and $V_{oc}$ reduction is lower than C12DPP-$\pi$-BT:PCBM system.

(4) In addition, according to Shockley and Queisser's paper, the maximum thermodynamic $V_{oc}$ value can only be reached in the absence of non-radiative recombination[67]. In theory, the recombination mechanism will affect the highest achievable $V_{oc}$.

## 2.3.10 Recombination Mechanism

Despite the uncertainty factors in electro-chemical measurements and possible interfacial interaction between active components, we hypothesize that the 3$^{rd}$ and the 4$^{th}$ reasons mentioned above contributes to the observed difference of $V_{oc}$ between C12DPP-$\pi$-BT:PCBM and C12DPP-$\pi$-BT:P3HT. To better understand charge generation and recombination process (4$^{th}$ reason in last section) in these systems and hence their effects on device performance, the light intensity dependence of photoconductivity[68] was characterized. Figure 2.10 shows the photocurrent versus relative intensity of 2.43 eV (488 nm) excitation at different electric fields for (a) high $M_n$ C12DPP-$\pi$-BT, (b) high $M_n$ C12DPP-$\pi$-BT:PCBM blends and (c) high $M_n$ C12DPP-$\pi$-BT:P3HT blends films. Fitting the curves to $i_{pc} \propto I_0^n$ showed that the exponent $n$ for the pure C12DPP-$\pi$-BT polymer

sample is ~0.4, indicating a bimolecular nature of recombination that has a square-root dependence on intensity. For C12DPP-π-BT:P3HT devices, the exponent $n$ remains at ~0.5; this is characteristic of bimolecular recombination, indicating the absence of deep traps in the film. In contrast, after blending with PCBM, the mixed sample showed an increase in $n$ to ~0.7. This reveals the existence of both bimolecular recombination and monomolecular recombination, a competing process that has a linear dependence on excitation intensity. The first-order recombination kinetics suggest the presence of more recombination centers in the C12DPP-π-BT:PCBM mixture than in pure C12DPP-π-BT and in the C12DPP-π-BT:P3HT mixture, such as charge carrier traps at the interface of the two materials[69]. Such trap-assisted recombination would cause the $V_{oc}$ measured in C12DPP-π-BT:PCBM devices to be lower than the value deduced from the difference between acceptor LUMO and donor HOMO[70], and lower than that in C12DPP-π-BT:P3HT devices. In addition, the existence of charge traps can increase the recombination of electrons and holes thereby reducing the fill factor, which in turn limits device efficiency[69, 71].
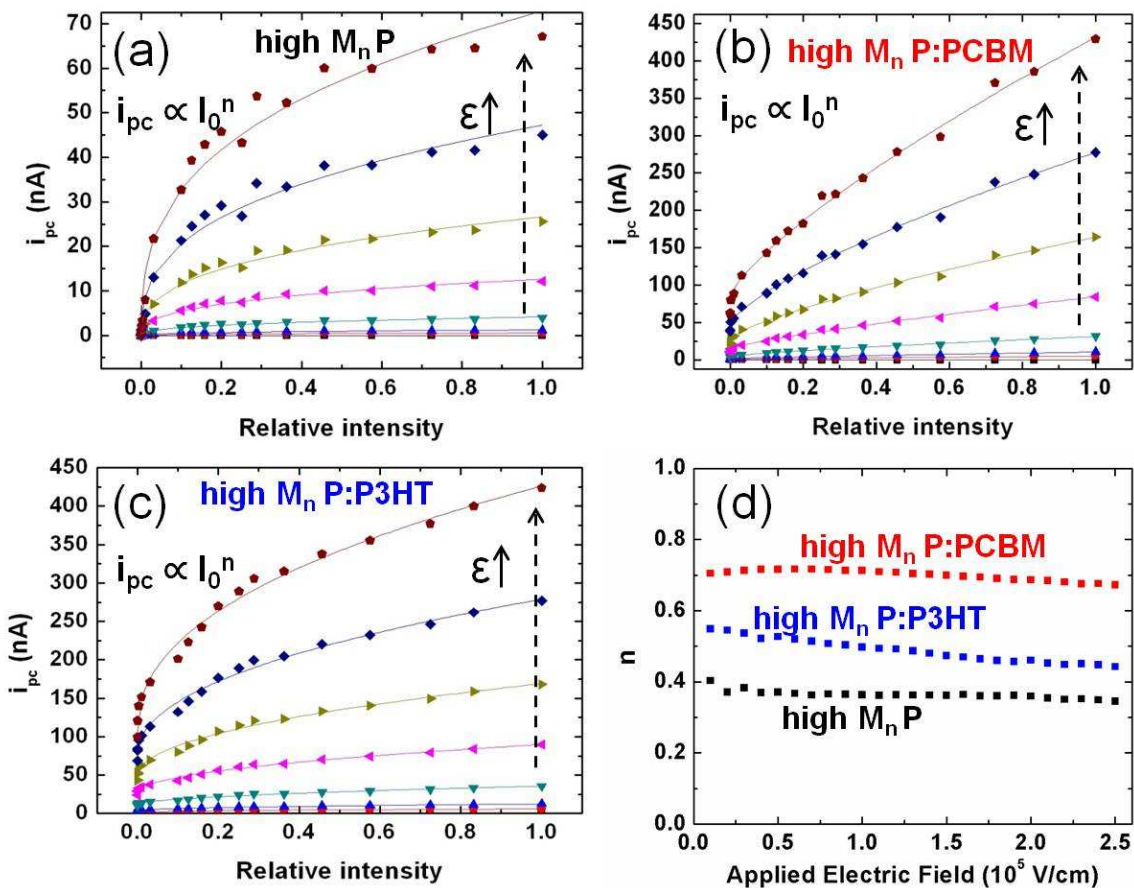
**Figure 2.10.** Intensity dependence of the photocurrent: (a) high $M_n$ C12DPP-$\pi$-BT only thin films (b) high $M_n$ C12DPP-$\pi$-BT:PCBM blend thin films and (c) high $M_n$ C12DPP-$\pi$-BT:P3HT blend thin films at applied electric fields of (■) 0 (●) 0.1(▲) 0.2(▼) 0.5(◀) 1.0 (▶) 1.5 (♦) 2.0 (●) $2.5 \times 10^5$ V/cm. (d) Power values, *n*, of the function $i_{pc} \propto I_0^n$ vs electric field for (■) the high $M_n$ C12DPP-$\pi$-BT only, (■) the high $M_n$ C12DPP-$\pi$-BT:PCBM blend and (■) high $M_n$ C12DPP-$\pi$-BT:P3HT blend. Laser: 488nm, 19.8A, 0.291W; intensity at the sample: 16.6W/cm$^2$ for the largest intensity (Relative intensity=1)

## 2.3.11 OLED application with C12DPP-π-BT

C12DPP-π-BT has been demonstrated to operate as either an electron donor or an electron acceptor in the photovoltaic devices and confirmed to have good hole and electron transport properties by SCLC and strong photoluminescence. Therefore, C12DPP-π-BT was expected to also be a promising candidate for organic/polymer light emitting diodes. To test its potential for OLED, we have incorporated C12DPP-π-BT in a single layer sandwich structure of ITO/PEDOT:PSS/C12DPP-π-BT/LiF/Al (Figure 2.11 (a)), in which C12DPP-π-BT served as emissive and charge transport layer. During operation, a voltage was applied across the electrodes. Electrons are injected into the LUMO of C12DPP-π-BT at cathode (Al/LiF) while holes are injected into the HOMO of C12DPP-π-BT through anode (ITO/PEDOT:PSS). Electrons and holes are driven towards each other by electrostatic Coulomb force. The charge recombination forms an exciton and the decay of exciton (excited state) results in a relaxation of the energy levels of the electron accompanied by light emission. (Figure 2.11 (b)) Without any optimization, OLEDs based on the pure polymer exhibited good preliminary results: the device demonstrated high current density, bright red emission and low diode turned on voltage (~ 3V). (Figure 2.11 (c-f))
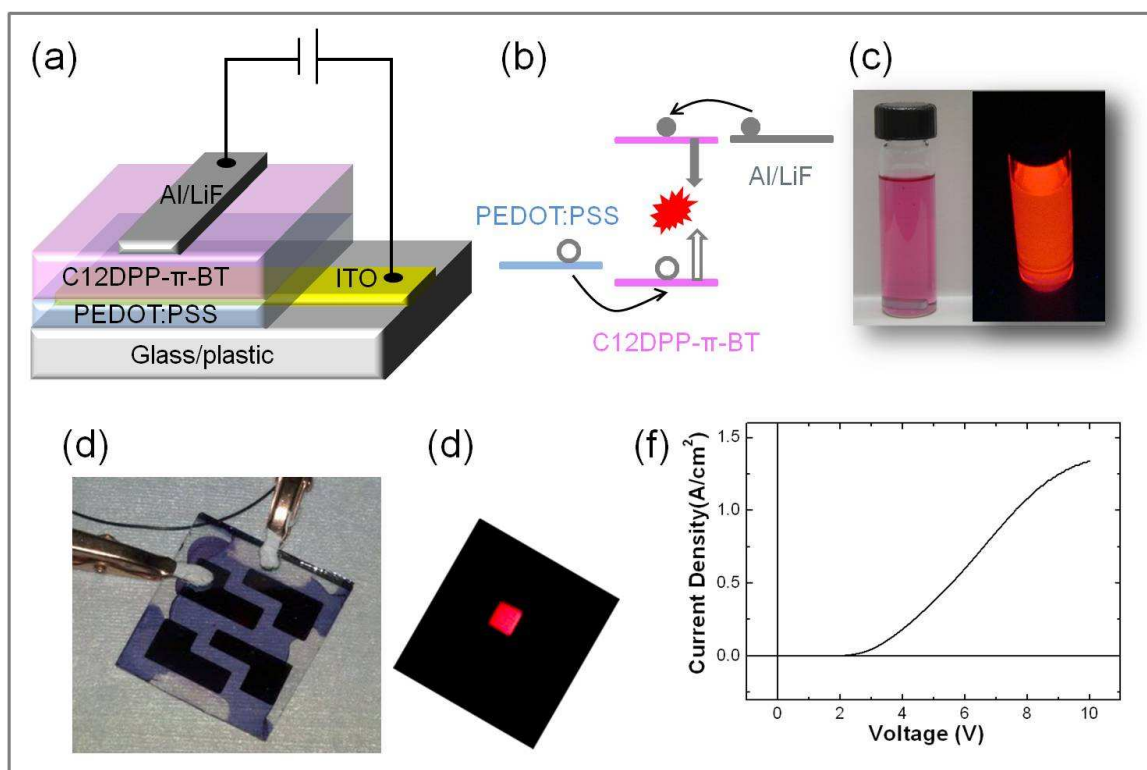
**Figure 2.11.** . (a) Schematic of C12DPP-π-BT OLED device layout (b) Schematic of energy diagram of active layer and electrodes, showing electron-hole recombination and light emitting (c) photo of photoluminescence upon excitation by UV lamp (254 nm) (d) photo of OLED device (e) photo of OLED device turned on in operation in dark (f) I-V Characterization of OLED devices with C12DPP-π-BT

**2.3.12 Polymer Field Effect Transistor Based on C12DPP-π-BT**

In this section, charge transport characteristics and organic field effect transistor (OFET) application of C12DPP-π-BT are discussed. Top contact bottom gate (TC-BG configuration) OFETs were fabricated on heavily doped silicon wafers with 250 nm thermally grown $SiO_2$, which served as the gate electrode and gate dielectric layer, respectively. Self-assembled monolayers (SAMs) of octadecyltrichlosilane (OTS) were used for surface modification to increases surface hydrophobicity and improve molecular order and mobility[72]. C12DPP-π-BT was spin cast from solution as the semiconductor layer followed by the vacuum deposition of source and drain electrodes (Au).

Figure 2.12(a) illustrates the layout of polymer FET devices. Figure 2.12 (b, c) shows the representative transfer and output characteristics of FET devices with different molecular weights. All devices featured hole dominated transfer behavior. The mobility can be extracted from hole saturation regimes based on the following equation, which is originally developed for Si MOSFETs.

Assuming mobility is gate voltage independent, in the saturation regimes when $V_G \leq V_{th} < 0 \; and \; V_G - V_{th} > V_D$, mobility can be estimated by the following equation[73]:

$$I_D = \frac{WC\mu}{2L}(V_G - V_{th})^2 \qquad (1)$$

$$\Rightarrow \mu = \frac{2L}{WC}(\frac{d\sqrt{I_D}}{dV_G}) \qquad (2)$$

where µ is the charge-carrier effective mobility, W is the channel width, L is the channel length, C is the gate oxide capacitance per unit area, $V_G$ is gate-to-source voltage and $V_{th}$ is the threshold voltage, and $I_D$ is source-drain current.

The top-contact, bottom-gate (TC-BG) transistors with C12DPP-π-BT semiconducting channels exhibited field-effect hole mobilities of $0.04\pm0.004$ cm$^2$V$^{-1}$s$^{-1}$ for high $M_n$ polymer and $0.03\pm0.005$ cm$^2$V$^{-1}$s$^{-1}$ for low $M_n$ polymer, showing a slightly better transport for the higher $M_n$ polymer, which is consistent with the previous SCLC results of high hole mobility and better OPV performance for high $M_n$ polymer. This could be a result of smaller number of well defined crystalline domains and hence fewer boundaries in the higher $M_n$ polymer as suggested by AFM topography images in Figure 2.9. Moreover, the higher $M_n$ polymer offers longer chains for the charge carrier to travel along the polymer chain and reduced inter-chain hopping[74]. All devices showed a very linear $I_D$ -$V_{DS}$ characteristics at lower voltages for hole currents. This could be attributed to two factors: 1) low contact resistance due to the large charge injection area under TC-BG configuration compared to a bottom contact devices 2) lower access resistance due to gold electrode metal penetration into the polymer thin film[75].

It is important to understand the relationship between channel dimension and device property in organic FET in order to evaluate the materials and optimize devices. To this end, the mobility dependence on the channel length was investigated by varying the channel length while keeping the W/L ratio constant. First, we shall briefly discuss the common short-channel effects, which can be applied towards organic FETs using the following equations[76]:

$$R_{Total} = R_{Contact} + R_{Channel} = R_{Contact}^{Sheet} * \frac{1}{W} + R_{Channel}^{Sheet} * \frac{L}{W} \qquad (3)$$

Assuming Ohmic relationship between current (I) and total resistance (R$_{Total}$),

$$I = \frac{V}{R_{Total}} = \frac{V}{R_{Contact}^{Sheet} * \frac{1}{W} + R_{Channel}^{Sheet} * \frac{L}{W}} = \frac{V * (\frac{W}{L})}{R_{Contact}^{Sheet} * \frac{1}{L} + R_{Channel}^{Sheet}} \qquad (4)$$

where $R_{Total}$ is the total resistances, $R_{Contact}$ and $R_{Channel}$ represent two resistance sources from contact interface and channel material, and W, and L represent channel width and length, and W/L ratio is a constant in all our silicon substrate based FET devices. The sheet resistance is determined by materials properties and is a constant. The total resistance ($R_{Total}$) decreases with increasing channel W (or L) since $R_{Channel}$ is constant with a fixed W/L and $R_{Contact}$ is inversely proportional to W (or L). Therefore the current and mobility will typically decrease with decreasing channel width (length), which poses a challenge for device scaling. However, opposite to the trend in amorphous Si FETs[77, 78], the hole mobility of polymer FET devices using C12DPP-π-BT increased with decreasing channel lengths. Two factors may contribute to the observed inverse relationship between mobility and channel length: 1) the intrinsic resistance of polymers is high, which will weaken the effect of contact resistance to some extent when $R_{Contact}$/L is considerably small compared with $R_{Channel}$ in equation 4. In addition, for organic FETs, shorter channel lengths may reduce the number of grains and grain boundaries, which in turn may increase charge mobility[79, 80]; 2) the increased drift mobility is positively correlated with increasing electric-field, which has been observed in many organic materials[81]. A shorter channel length increases the longitudinal electric field when the applied voltage $V_{DS}$ is constant, therefore increasing the drift mobility and the measured hole mobility. The statistics of device performance is summarized in Figure 2.12(d,e). Here we noticed that

all devices featured hole dominated transport behavior, which is contrary to what we expect since C12DPP-π-BT shows the ability to transport both electrons and holes in solar cells, OLED and SCLC measurements. A few reasons might be attributed to the absence of electron transport: 1) electron traps at the dielectric-semiconductor, which is common for organic semiconductor; 2) possible high injection barriers for electrons at the metal-semiconductor interface; 3) anisotropic conductivity of the polymer may cause different conductivity behavior in a vertical device (solar cells and OLEDs, in which current flows in a direction perpendicular to the substrate) than in a lateral device (OFET, in which current flows parallel to the substrate). Further optimization strategies, such as using different Si surface treatment and applying a different dielectric layer to avoid electron traps and defects, modifying source and drain electrodes to reduce the electron injection barrier to improve the charge injection, shall be investigated.
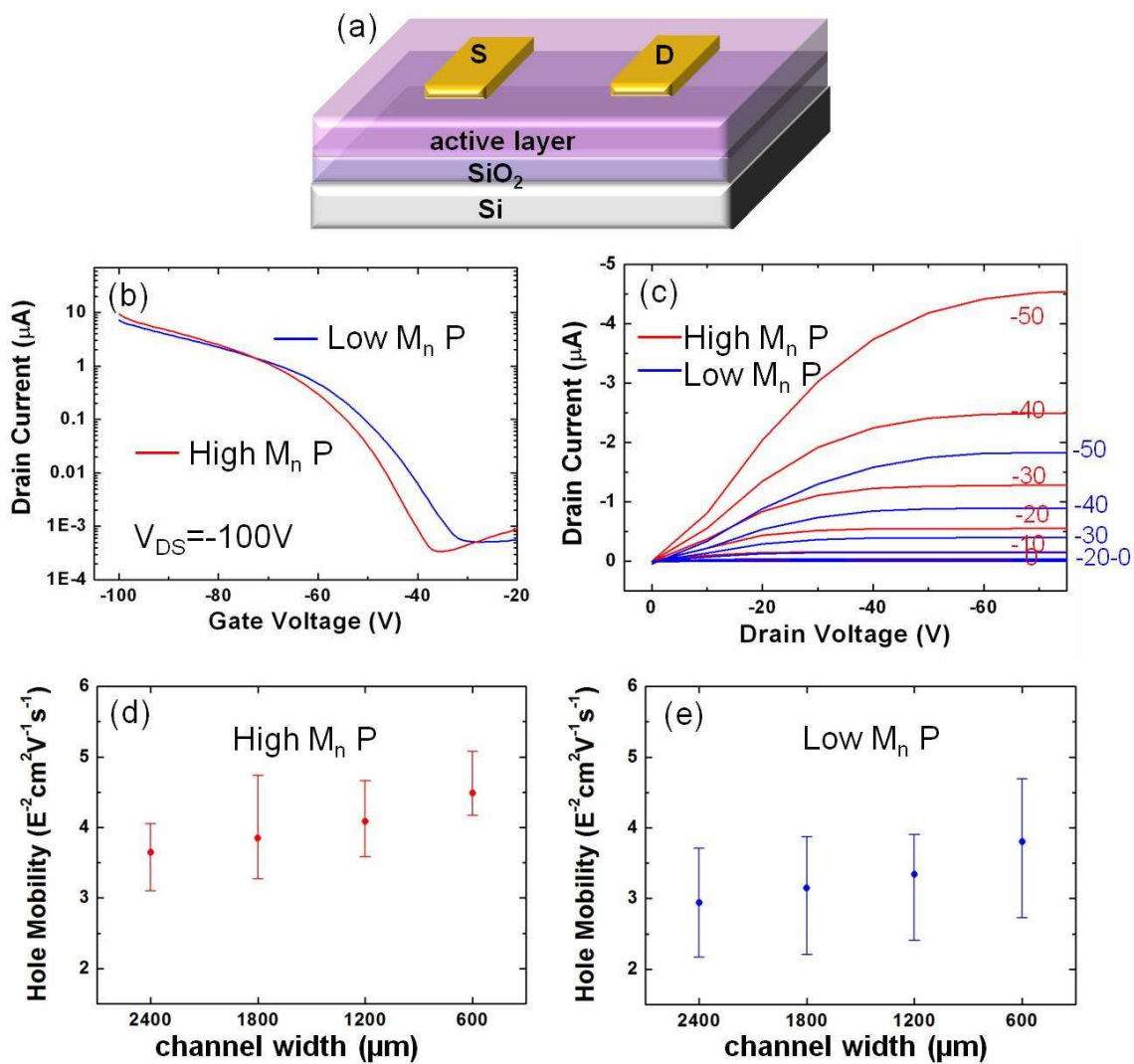
**Figure 2.12.** (a) Schematic of polymer FET devices with top contact bottom gate configuration, (b) transfer characteristics ($I_D$-$V_G$) ($V_{DS}$: -100V) and (c) output characteristics ($I_D$-$V_{DS}$) for high $M_n$ C12DPP-$\pi$-BT (red line) and low $M_n$ C12DPP-$\pi$-BT (blue line) in the hole accumulation regimes. Channel length is 60 µm and channel width is 1200 µm for silicon substrate devices. (d-e) Hole mobility dependence on channel width for (d) high $M_n$ C12DPP-$\pi$-BT and (e) low $M_n$ C12DPP-$\pi$-BT polymer FET. (W/L is fixed at 20.)

**2.3.13 Organic Field Effect Transistor Based on C12DPP-π-BT/PCBM blends**

Charge transport is a key factor for tuning the transfer characteristics of transistors. In addition, FET mobility measurements will provide useful information regarding the electron and hole transport which assists the design of donor and acceptor with balanced charge transport to improve the efficiency of solar cells. To that end, FETs based on C12DPP-π-BT and PCBM blends have been fabricated and characterized to study charge carrier transport. The devices were fabricated following the same procedure as pure polymer FET devices. Different blends ratios have been used to explore the dependence of hole/electron current under these fabrication conditions. As discussed previously, the pure polymer indicated hole dominated transfer characteristics. After blending with PCBM, electron injection was significantly improved because the LUMO of PCBM is closer to the work function of Au. As a result, the organic FET device based on the blends (C12DPP-π-BT:PCBM 1:2 weight ratio) demonstrates ambipolar FET properties as shown in Figure 2.13 (a). Previously, we have shown p-channel FET devices based on the pure C12DPP-π-BT polymer. It is worth mentioning that, after blending with PCBM, not only has the electron current increased significantly, but the hole mobility has also been enhanced from 0.04 $cm^2V^{-1}s^{-1}$ to 0.08-0.09 $cm^2V^{-1}s^{-1}$. Regarding this interesting phenomena, we have three hypotheses: 1) the addition of PCBM could improve inter-chain interaction of C12DPP-π-BT polymer. For the pure polymer, inter-chain transport is impeded by the high potential barrier between neighboring polymers caused by high energy insulating dodecyl side chains. After intermixing, the flexible long side chain allows the proximity of PCBM to the polymer backbone. And the inserted PCBM can effectively reduce the potential barrier because of the relatively close HOMO levels

between C12DPP-π-BT and PCBM, thereby facilitating charge tunneling within polymer network and increasing hole mobility. This hypothesis is consistent with the increased molecular packing we observed in XRD experiment (in Section 2.3.4 XRD pattern indicates a reduced π–π stacking distance between polymer backbones from 4.9 Å for pure C12DPP-π–BT to 4.6 Å for C12DPP-π-BT:PCBM). 2) the second possible mechanism is that C12DPP-π–BT and PCBM could form a new electronic state such as a charge-transfer complex[82], which can transfer both electrons and holes more efficiently than pristine C12DPP-π–BT. 3) it is possible that PCBM blending changed the polymer grain structure, which could lead to reduced grain sizes and grain boundaries and hence better charge transport.

We further increased the weight ratio of PCBM (C12DPP-π-BT:PCBM 1:4 weight ratio) in the blend and observed that the device changed from behaving as an ambipolar transistor (C12DPP-π-BT:PCBM 1:4 weight ratio) to an n-channel FET device (electron dominated transport). We propose that, with too high concentration of PCBM, it is possible that the continuity of polymer network is broken, leading to rapidly deteriorating hole transport. The typical electron mobilities are low across all devices, which is an indication of a large number of electron traps at the surface and/or in the bulk caused by impurities and defects. Figure 2.13 exhibits output characteristics in the electron regime for n-channel FET device based on the polymer:PCBM blends (ratio 1:4) and output characteristics in both the electron (Figure 2.13 (c)) and hole (Figure 2.13 (d)) accumulation regimes for ambipolar FETs based on blends (ratio 1:2).

In conclusion, by adjusting the PCBM ratio to C12DPP-$\pi$–BT (0:1, 2:1, 4:1), we successfully altered the nature of FET device from p-channel to ambipolar to n-channel conducting. The transfer characteristics could provide useful information to balance electron-hole transport and optimize photovoltaic devices. In addition, the preliminary results of C12DPP-$\pi$–BT:PCBM blends have demonstrated the ability and potential for ambipolar OFET devices, which serve as the elements for organic complementary circuit technology.
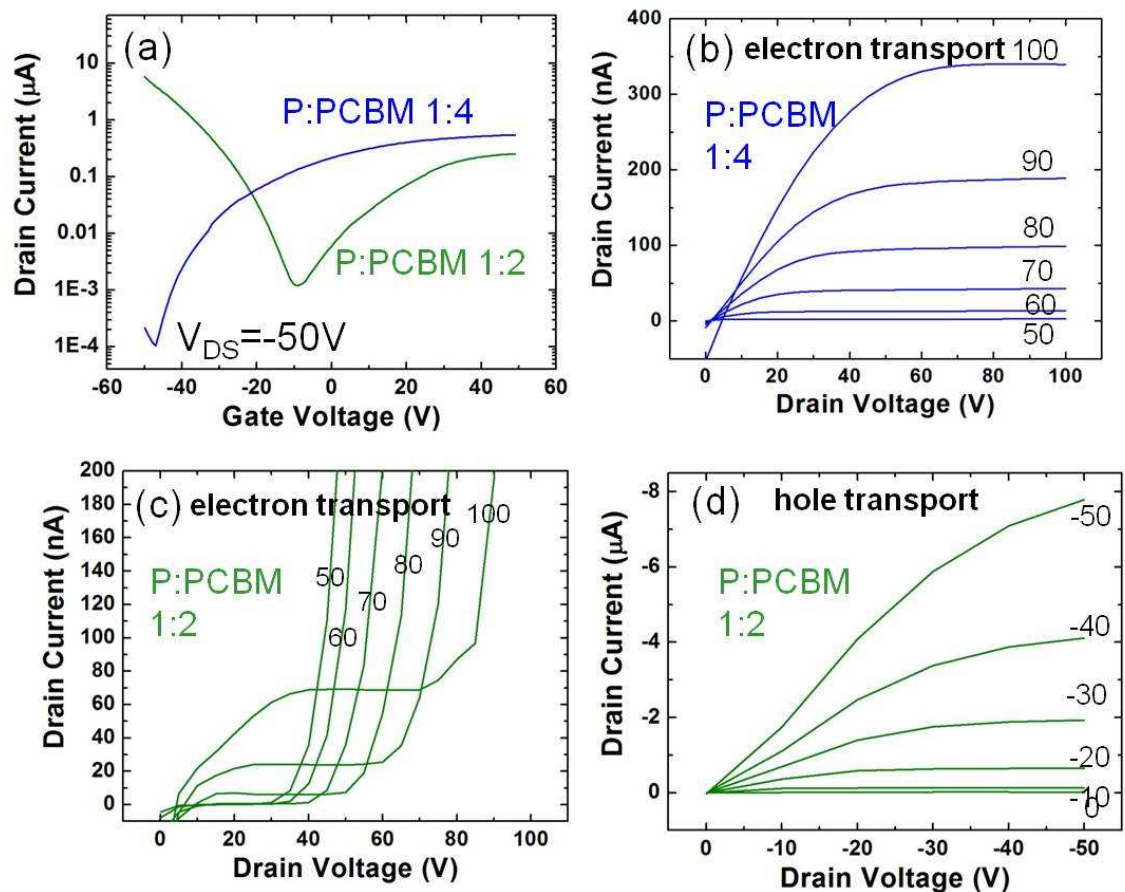
**Figure 2.13.** Characterization of FET devices with C12DPP-π-BT:PCBM blend. (a) transfer characteristics (C12DPP-π-BT:PCBM weight ratio1:2, 1:4) (b) output characteristics in electron regime for blends (C12DPP-π-BT:PCBM ratio 1:4); (c) output characteristics in electron and (d) hole accumulation regimes for blends (C12DPP-π-BT:PCBM ratio 1:2). All devices are fabricated with same procedure and channel width to length ratio of 20.

**2.4 Conclusion**

In conclusion, we report the synthesis, characterization, and implementation of a new diketopyrrolopyrrole-based polymer with energy levels located between those of commonly used electron donor and electron acceptor materials. Unlike previously reported diketopyrrolopyrrole-based polymers and small molecules which have only been used as either the electron donor or acceptor in OPVs, we show that C12DPP-$\pi$-BT can function as either an electron donor or electron acceptor in solution-processable organic photovoltaics. A moderate power conversion efficiency of 1.67% was achieved with the high $M_n$ C12DPP-$\pi$-BT polymer:PCBM blend devices and 0.84% with higher $M_n$ C12DPP-$\pi$-BT polymer:P3HT blend devices. SCLC measurements confirm both electron and hole transport in the C12DPP-$\pi$-BT copolymer. We have demonstrated that C12DPP-$\pi$-BT polymer with higher $M_n$ gives rise to increased photon generation and carrier transport and therefore higher $I_{sc}$, $V_{oc}$, and overall OPV efficiency. Comparing C12DPP-$\pi$-BT:PCBM and C12DPP-$\pi$-BT:P3HT devices, which are characterized by the same built-in potential from electrochemical calculations, a higher $I_{sc}$, but smaller $V_{oc}$ is obtained for C12DPP-$\pi$-BT:PCBM devices. The higher $I_{sc}$ in C12DPP-$\pi$-BT:PCBM devices is believed to originate from ultrafast, efficient charge transfer and more balanced electron and hole transport, while the $V_{oc}$ is limited by trap-assisted recombination and interfacial contact losses. In contrast, the C12DPP-$\pi$-BT:P3HT system achieves higher $V_{oc}$, yet suffers from lower $I_{sc}$ due to possible limitation in charge transfer hindered by long alkyl chain, which increases the intermolecular distance and prevents the closer contact of two polymers. The rational design of donor-acceptor copolymers can provide

organic photovoltaic materials with large built-in potentials and balanced electron and hole transport, promising efficient OPVs. The polymer based FET exhibited good hole current. And after further mixing with PCBM, the blends based FET demonstrated ambipolar transport characteristics with high hole mobility and improved electron transport. We successfully altered the nature of FET device from p-channel to ambipolar to n-channel conducting by adjusting the weight ratio of PCBM. The transfer characteristics could assist photovoltaic devices design. In addition, the preliminary results of C12DPP-π–BT:PCBM blends indicate its ability and potential for ambipolar OFET devices.

Further optimization of materials design and processing, such as shorter, yet solubilizing, branched side chains, investigation of solvents and annealing effects to increase charge transfer in polymer-polymer blends and improving morphologies to reduce carrier trapping in polymer-PCBM blends, is critical to further increase device efficiencies. Finally, the strong photoluminescence and ambipolar nature of C12DPP-π-BT make it a promising candidate for organic light emitting diode and organic light emitting transistor applications.

## References

1.      Bijleveld, J. C.; Zoombelt, A. P.; Mathijssen, S. G. J.; Wienk, M. M.; Turbiez, M.; de Leeuw, D. M.; Janssen, R. A. J. *Journal of the American Chemical Society* **2009,** 131, (46), 16616-16617.

2.      Günes, S.; Neugebauer, H.; Sariciftci, N. S. *Chemical Reviews* **2007,** 107, (4), 1324-1338.

3.      Hou, J.; Chen, H.-Y.; Zhang, S.; Chen, R. I.; Yang, Y.; Wu, Y.; Li, G. *Journal of the American Chemical Society* **2009,** 131, (43), 15586-15587.

4.      Park, S. H.; Roy, A.; Beaupre, S.; Cho, S.; Coates, N.; Moon, J. S.; Moses, D.; Leclerc, M.; Lee, K.; Heeger, A. J. *Nat Photon* **2009,** 3, (5), 297-302.

5.      Walker, B.; Tamayo, A. B.; Dang, X.-D.; Zalar, P.; Seo, J. H.; Garcia, A.; Tantiwiwat, M.; Nguyen, T.-Q. *Advanced Functional Materials* **2009,** 19, (19), 3063-3069.

6.      Li, G.; Shrotriya, V.; Huang, J.; Yao, Y.; Moriarty, T.; Emery, K.; Yang, Y. *Nat Mater* **2005,** 4, (11), 864-868.

7.      Peng, Q.; Park, K.; Lin, T.; Durstock, M.; Dai, L. *The Journal of Physical Chemistry B* **2008,** 112, (10), 2801-2808.

8.      Wienk, M. M.; Turbiez, M.; Gilot, J.; Janssen, R. A. J. *Advanced Materials* **2008,** 20, (13), 2556-2560.

9.      Chan, W. K.; Chen, Y.; Peng, Z.; Yu, L. *Journal of the American Chemical Society* **1993,** 115, (25), 11735-11743.

10.     Shi, M.-M.; Deng, D.; Chen, L.; Ling, J.; Fu, L.; Hu, X.-L.; Chen, H.-Z. *Journal of Polymer Science Part A: Polymer Chemistry* 49, (6), 1453-1461.

11.     Sun, S. S., N. S., *Organic PhotoVoltaics*. CRC Press: Boca Raton, FL, 2005.

12.     Bao, Z.; Chan, W. K.; Yu, L. *Journal of the American Chemical Society* **1995,** 117, (50), 12426-12435.

13.     Behnke, M.; Tieke, B. *Langmuir* **2002,** 18, (10), 3815-3821.

14.     Zhu, Y.; Zhang, K.; Tieke, B. *Macromolecular Chemistry and Physics* **2009,** 210, (6), 431-439.

15.     Beyerlein, T.; Tieke, B.; Forero-Lenger, S.; Brütting, W. *Synthetic Metals* **2002,** 130, (2), 115-119.

16.     Chen, L.; Deng, D.; Nan, Y.; Shi, M.; Chan, P. K. L.; Chen, H. *The Journal of Physical Chemistry C* 115, (22), 11282-11292.

17.     Zhou, E.; Yamakawa, S.; Tajima, K.; Yang, C.; Hashimoto, K. *Chemistry of Materials* **2009,** 21, (17), 4055-4061.

18.     Karsten, B. P.; Bijleveld, J. C.; Janssen, R. A. J. *Macromolecular Rapid Communications* 31, (17), 1554-1559.

19.     de Leeuw, D. M.; Simenon, M. M. J.; Brown, A. R.; Einerhand, R. E. F. *Synthetic Metals* **1997,** 87, (1), 53-59.

20.     Huo, L.; Hou, J.; Chen, H.-Y.; Zhang, S.; Jiang, Y.; Chen, T. L.; Yang, Y. *Macromolecules* **2009,** 42, (17), 6564-6571.

21.     Li, Y.; Singh, S. P.; Sonar, P. *Advanced Materials* 22, (43), 4862-4866.

22.     Zhou, E.; Wei, Q.; Yamakawa, S.; Zhang, Y.; Tajima, K.; Yang, C.; Hashimoto, K. *Macromolecules* **2009,** 43, (2), 821-826.

23.     Li, Y.; Sonar, P.; Singh, S. P.; Soh, M. S.; van Meurs, M.; Tan, J. *Journal of the American Chemical Society* 133, (7), 2198-2204.

24.    Coulson, D. R.; Satek, L. C.; Grim, S. O., *Tetrakis (Triphenylphosphine) Palladium (0)*. John Wiley & Sons, Inc.: 2007; p 121-124.

25.    Kozma, E.; Kotowski, D.; Bertini, F.; Luzzati, S.; Catellani, M. *Polymer* 51, (11), 2264-2270.

26.    Murphy, A. R.; Liu, J.; Luscombe, C.; Kavulak, D.; Fr 茅 chet, J. M. J.; Kline, R. J.; McGehee, M. D. *Chemistry of Materials* **2005,** 17, (20), 4892-4899.

27.    Rabindranath, A. R.; Zhu, Y.; Heim, I.; Tieke, B. *Macromolecules* **2006,** 39, (24), 8250-8256.

28.    Wu, M.-C.; Lo, H.-H.; Liao, H.-C.; Chen, S.; Lin, Y.-Y.; Yen, W.-C.; Zeng, T.-W.; Chen, Y.-F.; Chen, C.-W.; Su, W.-F. *Solar Energy Materials and Solar Cells* **2009,** 93, (6-7), 869-873.

29.    Brabec, C. J.; Cravino, A.; Meissner, D.; Sariciftci, N. S.; Fromherz, T.; Rispens, M. T.; Sanchez, L.; Hummelen, J. C. *Advanced Functional Materials* **2001,** 11, (5), 374-380.

30.    Gregg, B. A. *The Journal of Physical Chemistry B* **2003,** 107, (20), 4688-4698.

31.    Moliton, A.; Nunzi, J.-M. *Polymer International* **2006,** 55, (6), 583-600.

32.    Pommerehne, J.; Vestweber, H.; Guss, W.; Mahrt, R. F.; Bässler, H.; Porsch, M.; Daub, J. *Advanced Materials* **1995,** 7, (6), 551-554.

33.    Brabec, c., Dyakonov, V., Scherf, U., *Organic Photovoltaics: Materials, Device Physics, and Manufacturing Technologies*. 2008.

34.    Lof, R. W.; van Veenendaal, M. A.; Koopmans, B.; Jonkman, H. T.; Sawatzky, G. A. *Physical Review Letters* **1992,** 68, (26), 3924.

35.     Veldman, D.; Meskers, S. C. J.; Janssen, R. A. J. *Advanced Functional Materials* **2009,** 19, (12), 1939-1948.

36.     Park, Y.; Choong, V.; Gao, Y.; Hsieh, B. R.; Tang, C. W. *Applied Physics Letters* **1996,** 68, (19), 2699-2701.

37.     Eremina, N.; Degtyarenko, K.; Kopylova, T.; Samsonova, L.; Gadirov, R.; Maier, G. *Theoretical and Experimental Chemistry* **2009,** 45, (1), 63-68.

38.     Scharber, M. C.; Mühlbacher, D.; Koppe, M.; Denk, P.; Waldauf, C.; Heeger, A. J.; Brabec, C. J. *Advanced Materials* **2006,** 18, (6), 789-794.

39.     Rand, B. P.; Burk, D. P.; Forrest, S. R. *Physical Review B* **2007,** 75, (11), 115327.

40.     Christoph J. Brabec, V. D., Ullrich Scherf, *Organic photovoltaics: materials, device physics, and manufacturing technologies*. 2008.

41.     Thompson, B. C.; Fréchet, J. M. J. *Angewandte Chemie International Edition* **2008,** 47, (1), 58-77.

42.     Li, G.; Shrotriya, V.; Yao, Y.; Huang, J.; Yang, Y. *Journal of Materials Chemistry* **2007,** 17, (30), 3126-3140.

43.     Sariciftci, N. S.; Smilowitz, L.; Heeger, A. J.; Wudl, F. *Science* **1992,** 258, (5087), 1474-1476.

44.     Hórvölgyi, Z.; Kiss, É.; Koeppe, R.; Fuchsbauer, A.; Lu, S.; Sariciftci, N., Energy Transfer from CdSe/ZnS Nanocrystals to Zinc-Phthalocyanine for Advanced Photon Harvesting in Organic Photovoltaics. In *Colloids for Nano- and Biotechnology*, Springer Berlin / Heidelberg: 2008; Vol. 135, pp 16-20.

45.     Hideo, O.; Junya, K.; Jiamo, G.; Hiroaki, B.; Shinzaburo, I. *Journal of Photonics for Energy* 1, (1), 011118.

46.     Bakulin, A. A.; Hummelen, J. C.; Pshenichnikov, M. S.; van Loosdrecht, P. H. M. *Advanced Functional Materials* 20, (10), 1653-1660.

47.     Rabiej, S. *European Polymer Journal* **1993,** 29, (4), 625-633.

48.     Cheng, C. H.; Wang, J.; Du, G. T.; Shi, S. H.; Du, Z. J.; Fan, Z. Q.; Bian, J. M.; Wang, M. S. *Applied Physics Letters* **2010,** 97, (8), 083305.

49.     Chen, L.-M.; Hong, Z.; Li, G.; Yang, Y. *Advanced Materials* **2009,** 21, (14-15), 1434-1449.

50.     Gur, I.; Fromer, N. A.; Chen, C.-P.; Kanaras, A. G.; Alivisatos, A. P. *Nano Letters* **2006,** 7, (2), 409-414.

51.     Peet, J.; Senatore, M. L.; Heeger, A. J.; Bazan, G. C. *Advanced Materials* **2009,** 21, (14-15), 1521-1527.

52.     Chen, L.-M.; Xu, Z.; Hong, Z.; Yang, Y. *Journal of Materials Chemistry* 20, (13), 2575-2598.

53.     Gedde, U. W. H., M. S. , *Polymer Physics*. Kluwer Academic Publishers: 1995.

54.     Krause, S. In *Polymer-polymer miscibility*, Pure Appl. Chem., 1986; 1986; pp 1553-1560.

55.     Mihailetchi, V. D.; Koster, L. J. A.; Blom, P. W. M.; Melzer, C.; de Boer, B.; van Duren, J. K. J.; Janssen, R. A. J. *Advanced Functional Materials* **2005,** 15, (5), 795-801.

56.     Prosa, T. J.; Winokur, M. J.; Moulton, J.; Smith, P.; Heeger, A. J. *Macromolecules* **1992,** 25, (17), 4364-4372.

57.     Chang, J.-F.; Sun, B.; Breiby, D. W.; Nielsen, M. M.; Sölling, T. I.; Giles, M.; McCulloch, I.; Sirringhaus, H. *Chemistry of Materials* **2004,** 16, (23), 4772-4776.

58.     Beranek, R.; Kisch, H. *Photochemical & Photobiological Sciences* **2008,** 7, (1), 40-48.

59.     Street, R. A.; Schoendorf, M.; Roy, A.; Lee, J. H. *Physical Review B* 81, (20), 205307.

60.     Murgatroyd, P. N. *Journal of Physics D: Applied Physics* **1970,** 3, (2), 151.

61.     Toshinori, M.; Hideyuki, M. *Applied Physics Letters* **2009,** 95, (20), 203306.

62.     Chiguvare, Z.; Dyakonov, V. *Physical Review B* **2004,** 70, (23), 235207.

63.     Cardona, C. M.; Li, W.; Kaifer, A. E.; Stockdale, D.; Bazan, G. C. *Advanced Materials* **2011,** 23, (20), 2367-2371.

64.     Pensack, R. D.; Banyas, K. M.; Barbour, L. W.; Hegadorn, M.; Asbury, J. B. *Physical Chemistry Chemical Physics* **2009,** 11, (15), 2575-2591.

65.     Bijleveld, J. C.; Verstrijden, R. A. M.; Wienk, M. M.; Janssen, R. A. J. *Applied Physics Letters* 97, (7), 073304.

66.     Tengstedt, C.; Crispin, A.; Hsu, C. H.; Zhang, C.; Parker, I. D.; Salaneck, W. R.; Fahlman, M. *Organic Electronics* **2005,** 6, (1), 21-33.

67.     Shockley, W.; Queisser, H. J. *Journal of Applied Physics* **1961,** 32, (3), 510-519.

68.     Cohen, Y. S.; Xiao, S.; Steigerwald, M. L.; Nuckolls, C.; Kagan, C. R. *Nano Letters* **2006,** 6, (12), 2838-2841.

69.     Morana, M.; Wegscheider, M.; Bonanni, A.; Kopidakis, N.; Shaheen, S.; Scharber, M.; Zhu, Z.; Waller, D.; Gaudiana, R.; Brabec, C. *Advanced Functional Materials* **2008,** 18, (12), 1757-1766.

70.     Mandoc, M. M.; Kooistra, F. B.; Hummelen, J. C.; Boer, B. d.; Blom, P. W. M. *Applied Physics Letters* **2007,** 91, (26), 263505.

71.     Hau, S. K.; Yip, H.-L.; Acton, O.; Baek, N. S.; Ma, H.; Jen, A. K. Y. *Journal of Materials Chemistry* **2008,** 18, (42), 5113-5119.

72.     Shtein, M.; Mapel, J.; Benziger, J. B.; Forrest, S. R. *Applied Physics Letters* **2002,** 81, (2), 268-270.

73.     Galup-Montoro, C.; Schneider, M. C. MOSFET modeling for circuit analysis and design. *London/Singapore: World Scientific.*, 2007

74.     Kline, R. J.; McGehee, M. D.; Kadnikova, E. N.; Liu, J.; Fréchet, J. M. J. *Advanced Materials* **2003,** 15, (18), 1519-1522.

75.     Pesavento, P. V.; Chesterfield, R. J.; Newman, C. R.; Frisbie, C. D. *Journal of Applied Physics* **2004,** 96, (12), 7312-7324.

76.     Saudari, S. R.; Lin, Y. J.; Lai, Y., Kagan, C. R. *Adv. Mater.* **2010**, 22, 5063-5068

77.     Luan, S.; Neudeck, G. W. *Journal of Applied Physics* **1992,** 72, (2), 766-772.

78.     Kanicki, J.; Libsch, F. R.; Griffith, J.; Polastre, R. *Journal of Applied Physics* **1991,** 69, (4), 2339-2345.

79.     Horowitz, G.; Hajlaoui, M.E. Synt. Met. **2001,** 122, 185-189.

80.     Weitz, R. T.; Amsharov, K.; Zschieschang, U.; Burghard, M.; Jansen, M.; Kelsch, M.; Rhamati, B.; van Aken, P. A.; Kern, K.; Klauk, H. Chem. Mater. 2009, 21, 4949–4954.

81.     Kanemitsu, Y.; Funada, H.; Masumoto, Y. *Journal of Applied Physics* **1992,** 71, (1), 300-303.

82.     Vandewal, K.; Oosterbaan, W. D.; Bertho, S.; Vrindts, V.; Gadisa, A.; Lutsen, L.; Vanderzande, D.; Manca, J. V. *Applied Physics Letters* **2009,** 95, (12), 123303.

# Chapter 3

# Study of Organic-Inorganic Hybrid Solar Cells Based on P3HT and PbSe Nanocrystal

### 3.1 Introduction to Organic-Inorganic Hybrid Solar Cells

Organic-inorganic hybrid bulk heterojunction solar cells are considered to be one the most promising candidates for the development of high efficiency photovoltaic devices and have received extensive attention recently because their solution processability and their excellent flexibility to chemically modify the optical and electrical properties of both organic and inorganic components[1-5]. For the inorganic component, colloidal semiconductor nanocrystals offer quantum confinement and therefore tunable properties. They have been incorporated into hybrid devices as the electron acceptor in conjunction with p-type semiconducting polymers[6]. Lead selenide (PbSe) nanocrystals have attracted increasing interests because they extend the polymer-PbSe composite's absorption into infrared to harvest a large fraction of solar radiation in the long wavelength region[7, 8]. In addition, recent studies suggested that PbSe may lead to multiple exciton generation from absorption of a single photon and yield more than 100% in internal quantum efficiency[9, 10]. However, the reported photovoltaic devices performance based on PbSe and commonly used polymers Poly (3-hexylthiophene-2,5-diyl) (P3HT) or Poly [2-methoxy-5-(2-ethylhexyloxy)-1,4-phenylenevinylene] (MEH-PPV) is poor despite the fact that PbSe has extended NIR absorption and demonstrated good mobility in the transistor geometry [7, 8, 11, 12]. Bulk heterojunction hybrid photovoltaic devices with PbSe and P3HT blends have only demonstrated less than 0.1% overall energy conversion efficiency[7, 8]. In contrast, photovoltaic devices with similar structure using P3HT and CdSe nanocrystals blends achieved power conversion efficiencies as high as 2%.[13] The poor photovoltaic performance of PbSe in bulk heterojunction devices is counterintuitive to its excellent optical and opto-electrical property.

96

The morphology control of nanocrystals has been proven critical to the success of high efficiency solar cells. Huyuh et al. reported a substantial enhancement of the efficiency of CdSe nanocrystals hybrid solar cell by replacing CdSe quasi-spherical quantum dots with elongated nanorods and achieved an efficiency of 1.7%[4]. The processing conditions also significantly influence the device performance. Yang et al. reported improved device performance by using higher boiling point solvents to slow down the solidification time of wet films to allow P3HT self-assembly, hence improved the hole mobility and device efficiency[14].

To summarize, the motivations of our research on the PbSe-P3HT solar cell system include: 1) PbSe has extended absorption into NIR region which will increase the utilization of photon energy. The energy in NIR was wasted in many solar cell systems, including those shown excellent efficiency such as P3HT/PCBM and P3HT/CdSe; 2) we have deep expertise and previous research experience in the synthesis of lead chalcogenide nanocrystals and nanowires; 3) the branched (spiny) nanowires may provide the ideal structure for hybrid solar cells. The spiny surface provides high p-n surface area for charge separation and the low energy core of the nanowires (the tunnel) offers efficient percolation pathways for electron transfer.

PbSe nanocrystals and nanowires were expected to be very promising candidates for hybrid solar cells. Successful BHJ architecture requires the donor and acceptor materials to be tailored to provide: 1) strong and broad absorption of solar radiation, 2) a staggered energy level structure (type-II heterojunction) to drive charge separation at the donor/acceptor interface, and 3) high hole and electron mobilities for efficient charge collection. The scopes of this study include 1) synthesis of PbSe nanocrystals and PbSe

nanowires with tunable shapes by tailoring the reaction condition, 2) incorporation and optimization of this near-IR sensitive electron acceptor material with P3HT for the hybrid solar cell fabrication, and 3) exploration of the energy conversion mechanism in this system.

### 3.2 Experimental Section

### 3.2.1 Materials

All experiments were performed under nitrogen atmosphere by standard Schlenk techniques. Lead acetate trihydrate (Aldrich, 99.999%), lead (II) oxide (PbO, Aldrich, 99.9%), selenium pellets(<4 mm, 99.99%), trioctyl phosphine (TOP, Fluka, 90%), oleic acid (OA, Aldrich, 90%), diphenyl ether (DPE, Aldrich,99.9%) squalane (Aldrich, 99%), 1-octadecene(ODE, Aldrich, 90%), Octanoic Acid (Aldrich, 99%), hexadecylamine (HDA, Aldrich, 98%), n-tetradecylphosphonic acid (TDPA, Aldrich, 97%) were used as purchased without further purification. Common solvents, like anhydrous hexane, chloroform, methanol, ethanol, acetone, toluene, chlorobenzene, and dichlorobenzene, are purchased from Aldrich, TCI and Fisher Scientific.

### 3.2.2 Synthesis of PbSe Nanocrystals and Nanowires with Shape Control

All syntheses were carried out with standard air-free technique (Schlenk line). The following purification and size selection processes were performed in a nitrogen-purged glovebox. The synthesis of mono-dispersed PbSe nanocrystals and nanowires was carried out via hot-injection method developed by Cho and Murray[15] with some modifications.

I. Synthesis conditions were adjusted to control the size and shape of PbSe nanocrystals.

1. The typical synthesis routes for quasi-spherical PbSe nanocrystals consisted of the following steps:

1) Preparation of selenium precursor: 7.86g Selenium were dissolved in 100mL trioctyl phosphine (TOP) at 50 °C over 3 hours inside the glovebox to prepare 1M stock solution of trioctylphosphine selenide (TOPSe).

Preparation of lead precursor: 0.56g lead acetate trihydrate were dissolved into 10 mL squalane in the presence of 1mL oleic acid. Alternatively, lead oxide (PbO) can be used to substitute lead acetate trihydrate and diphenyl ether (DPE) can substitute squalane. This stock solution was heated to 85ºC for 30minutes to 1 hour under vacuum ($<10^{-3}$ mbar) to dry the solution.

2) Lead precursor solution was heated to 180°C and 4.5 mL of 1 M solution of TOPSe in TOP were rapidly injected under vigorous stirring. The injection temperature and growth time can be adjusted to control the size of the nanocrystals. The total growth time was usually 3-10 minutes.

3) After the desired size is achieved, the reaction was then quenched using a cold water bath. The crude product was purified and separated by adding a small volume of hexane and ethanol, followed by centrifugation and dissolution of the precipitate in hexane. Further purification and size selection of the product can be achieved by several redissolving-centrifuging cycles in hexane, ethanol and acetone solution.

2. Synthesis of cubic PbSe nanocrystals

0.44g lead oxide and 2mL oleic acid were added to 10 mL diphenyl ether and heated to 85°C for 30 min under vacuum. After cooling to 60°C, lead oleate solution was mixed with 4mL 1M TOPSe in TOP. Approx. 70% of this solution was swiftly injected into

8mL of diphenyl ether which had been pre-heated to 200°C. Quenching and purification processes were similar as above.

3. Synthesis of star shape PbSe nanocrystals

0.44g lead oxide and 2mL oleic acid were added to 10 mL octadecene and heated to 85°C for 30 min under vacuum. After cooling to 60°C, lead oleate solution was mixed with 4mL 1M TOPSe in TOP. Approx. 50% of this solution was swiftly injected into a mixed solution of 0.8mL of octanoic acid and 8ml octadecene which had been pre-heated to 200°C. Quenching and purification processes were similar as above.

II. Synthesis of PbSe nanowires with shape control

1. Synthesis of zig-zag and helical PbSe nanowires

0.44 g of lead oxide and 2mL of oleic acid were dissolved in 10mL of phenyl ether and heated to 85°C for 30 min under vacuum to form lead oleate and dry the solution. After cooling to 60 °C, the lead oleate solution was mixed with 4mL of 0.167 M TOPSe solution in TOP. Then the mixture was rapidly injected into a hot (240 °C) solution containing 8mL of phenyl ether and 1-2g dissolved hexadecylamine (HDA), under vigorous stirring.

2. Synthesis of undulated, star shape and straight wires

Similar as the synthesis of zig-zag and helical PbSe nanowires, the same amounts of Pb:Se precursors and oleic acid were used with modifying the co-surfactants to control the shape of the nanowires. No co-surfactants were added to the reaction mixture in the case of undulated nanowires. 0.8mL octanoic acid was added to 8mL phenyl ether to synthesize star shape branched nanowires. 0.1g n-tetradecylphosphonic acid (TDPA) was added to 8mL phenyl ether to synthesize straight nanowires.

### 3.2.3 Direct Synthesis of PbSe Nanocrystals in P3HT Solution

The lead precursor was prepared by dissolving 100mg lead acetate trihydrate and 10mg P3HT in either 5.5mL 1-octadecene (ODE) and dichlorobenzene (DCB) mixture (10:1 volume ratio) or 12mL dimethylsulphoxide (DMSO) and DCB mixture at 1:2 volume ratios. In a second flask, a selenium precursor (1M) was prepared by dissolving selenium powder in TOP. Both solutions were heated for 1 h at 180°C under vigorous stirring. Then, 0.8mL of the selenium precursor was rapidly injected and left to react for 3 minutes at 150°C and finally quenched by ice/water bath.

### 3.2.4 Characterization

Cyclic voltammograms were obtained employing a three electrode C3 cell stand and Epsilon electrochemical workstation. To prepare the sample for measurements, a PbSe nanocrystal solution was drop cast onto a platinum electrode and dried in the vacuum chamber. For ligand exchanged samples, the electrode with a PbSe nanocrystal film was first immersed in the ligand (short thiols, hydrazine and pyridine) containing acetonitrile solution for various times (10min – 2h) and then rinsed with acetonitrile before the measurements. Concentrations used (in 1mL acetonitrile): ethane-1,2-thiol (0.18μL/1mL), thiophenol (1.02μL/1mL), ethanedithiol (0.84μL/1mL), benzene-1,4-dithiol (4.98mg/1mL), hydrazine (64μL/1mL). For pyridine, pure pyridine was used without dilution with acetonitrile.

Absorption spectra were measured using a Varian Cary 5000 UV-Vis-NIR spectrophotometer. Photoluminescence (PL) spectra were measured on a Fluorolog 3 spectrofluorometer (HORIBA Jobin Yvon, Ltd.) upon excitation at 550 nm. TEM (Transmission electron microscopy) images were obtained using a JEM-1400 at 120kV.

Sample preparation for XRD measurement: Si/SiO$_2$ substrate was prepared as in Chapter 2. 50 µL of as-synthesized PbSe were drop-cast from chloroform on the pre-cleaned silicon wafers and allowed to dry. XRD were performed using monochromatic CuK$\alpha$ beam radiation (wavelength: 0.154 nm) from a Rigaku SmartLab at 40 kV and 30 mA.

### 3.2.5 Device Fabrication and Characterization

P3HT/PbSe blend hybrid solar cells were fabricated on ITO coated glass substrates. The cleaning and PEDOT:PSS deposition was similar as described in Chapter 2. For the active layer, a) P3HT:PbSe mixture in chloroform (30mg/mL, approx. weight ratio: 1:2) or b) P3HT in chloroform (10mg/mL) or c) P3HT:PCBM mixture in chlorobenzene (17mg/mL, weight ratio: 1:1) were typically used for the active layer. The blend solution was deposited by spin-coating on top of the PEDOT:PSS layer at 1500 rpm for one minute and then annealed at 140 °C for 20 min and dried under vacuum.

Current-voltage characteristics of the photovoltaic cells were acquired using a Keithley 2400 source-meter under the illumination of AM 1.5G solar simulated light (1 sun, 100 mW/cm$^2$) in air or in the nitrogen box.

### 3.3 Results and Discussion

### 3.3.1 Synthesis of PbSe Nanocrystals and Nanowires with Shape Control

To prepare materials for hybrid solar cells, nanocrystals and nanowires were synthesized via hot injection methods. The design of nanocrystal synthesis follows the mechanism for the formation of nanocrystals from a homogeneous, supersaturated

medium proposed by La Mer and coworkers[16]. As shown in Figure 3.1, this mechanism suggests a 2-stage process, involving a nucleation period and a growth period. At the 1st stage, a quick injection of TOPSe (trioctylphosphine selenide) into the lead precursor solution at high temperature increases the monomer concentration rapidly, resulting in an abrupt super-saturation of PbSe monomer for a brief period. A quick burst of nucleation event occurs with the formation of a large number of nuclei. This process consumes the monomer reactants quickly and lowers the concentration below the nucleation level. Then it enters the 2nd stage - growth regime, which allows the nanocrystals to grow further at a slow rate. Separation and controlling of the growth regime by adjusting reagent concentration, growth temperature and growth time are essential to achieve a narrow distribution and high monodispersity of the final product. At the growth stage, nanocrystals grow at a rate that is inversely proportional to the nanocrystal size[17]. Therefore smaller nanocrystals grow faster than the larger nanocrystals, narrowing the size distribution. When the reactant concentrations were depleted below the critical monomer concentration ($C_c$), Ostwald ripening occurs[18, 19]. Larger nanocrystals grow and smaller nanocrystals dissolve, widening particle size distributions. To minimize this defocusing effect, the concentration of monomer needs to be kept above $C_c$ by controlling reaction time, and/or supplying additional precursor when the monomer concentration is too low in order to achieve the desired size with a focused distribution[17]. In the experiments, aliquots were taken during the reaction and size and dispersity were checked with TEM to determine the optimal growth time. A second drop-wise injection during the growth stage was also used to narrow the size distribution when necessary.
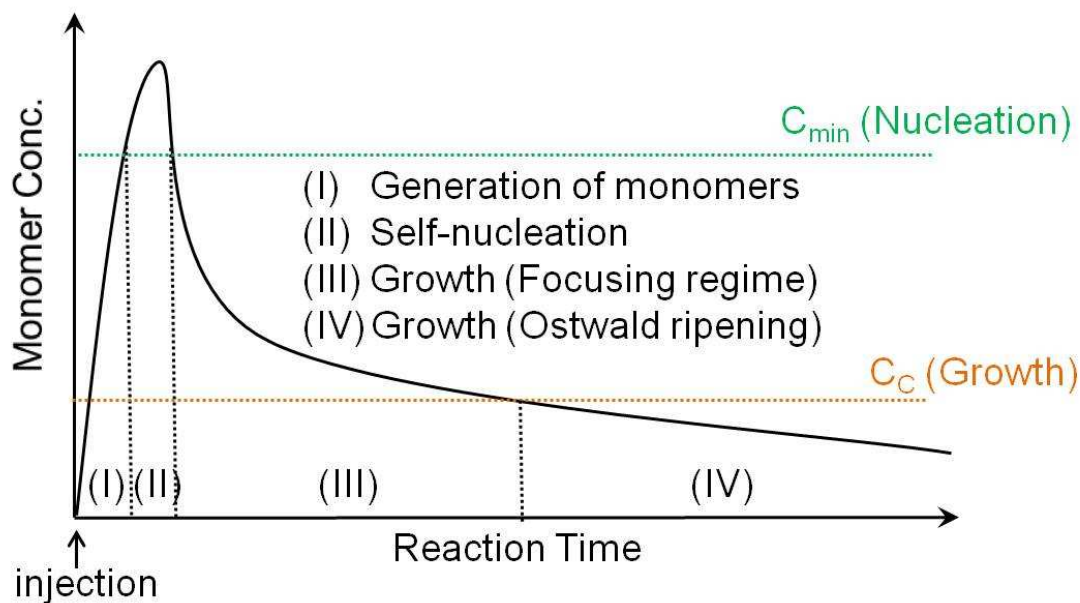
**Figure 3.1.** Schematic diagram illustrating synthesis of nanocrystal in colloid solution via hot injection method, showing the nucleation and growth region.

The synthesis of PbSe is based on the reaction between two precursors, lead oleate and trioctylphosphine-selenium, in the presence of long-chain surfactants. The oleic acid and the trioctylphosphine (TOP) are bound to the metal (Pb) and the chalcogenide (Se), respectively, to form the two precursors. Surfactants control the reaction rate and prevent aggregation between nanocrystals during reactions and stables the synthesized nanocrystals. Shape control of nanocrystal was achieved mainly through the adjustment of reaction temperature, growth time and surfactant. Shape-transition of nanocrystal from quasi-spherical to octahedrons to cubic occurs with increasing nanocrystal diameter as has been reported.[15, 20] The macroscopic PbSe has a cubic, rocksalt-type structure due to the lower surface energy of {100} facets than higher index {111} planes[21]. However, total stabilizing lattice energy is lower in the bulk than that on the surface because of the

high energy edges and corners. The balance between the force of maximizing {100} facets and the force of reducing edges and corners leads to the evolution of shapes of PbSe. It is predicted that when the size is small, the nanocrystals tend to exhibit quasi-spherical shape to minimize the surface:volume ratio. As the size increases, it will favor the formation of cubic structure to maximize {100} facets. The TEM image shown in Figure 3.2(a,b) confirmed this theory. For the star shape nanocrystals, shown in Figure 3.2(c), octanoic acid has been used as a co-surfactant with oleic acid. The star shape product is the result of faster growth of {100} facets than {111} facets. This may be attributed to blocking of {111} facets by octanoic acid, which decreases the growth rate along this direction. This mechanism was initially proposed by Cho et al., who used primary amines to assist the formation of star shape PbSe nanocrystal.[15] PbSe nanocrystals with different sizes (quasi-spherical) have also been synthesized and characterized. The absorption spectra of PbSe nanocrystal in Figure 3.2(f) indicate strong quantum confinements. The quantum confined optical property provides a convenient way to tune the absorption of nanocrystal to maximize the overlap with the solar spectrum. And the absorption in the red/infrared region compensates the absorption of widely used polymer, for example P3HT and MEH-PPV, which only absorbs in the visible range, in the hybrid solar cell.
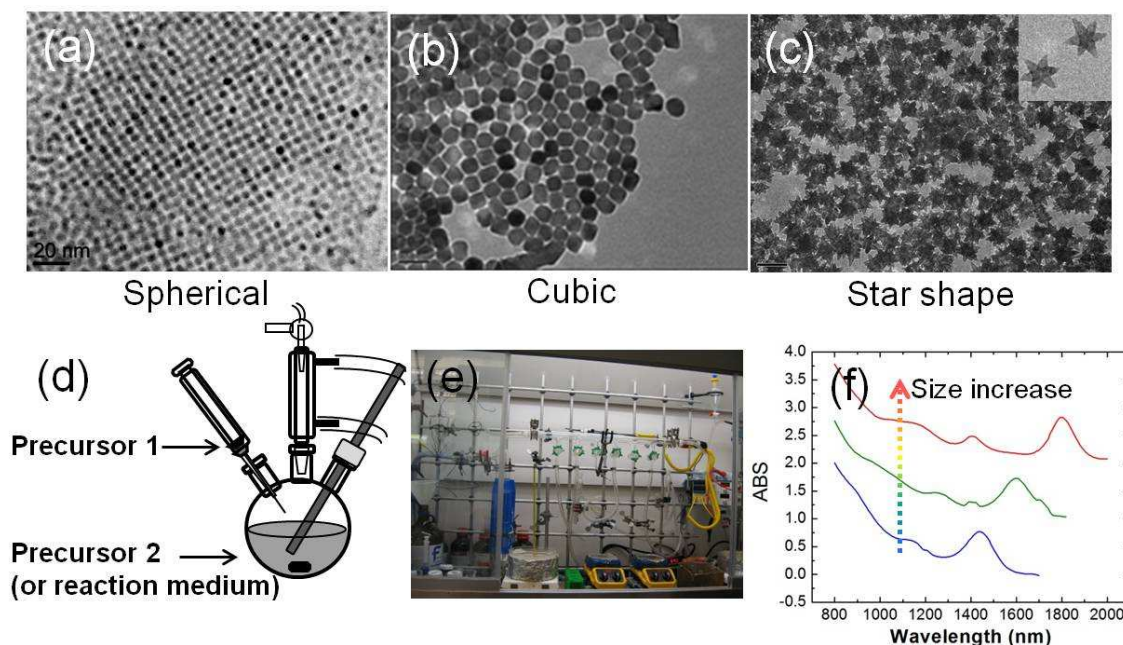
**Figure 3.2.** TEM images of PbSe NCs with different shapes (a) quasi-spherical nanocrystals, (b) cubic nanocrystals and (c) star shape nanocrystals; (d) Schematic illustration of synthesis of nanocrystal in solution via hot injection; (e) Photo of N2/vacuum Schlenk line for air sensitive synthesis; (f) Size dependent UV-Vis absorption spectra of PbSe nanocrystals, red shifting with increasing nanocrystals sizes due to quantum confinement effects (approx. nanocrystal size: 3.6nm, 5.4nm, 7.6nm, from bottom to top) Scale bar: (a) 20nm (b) 50nm (c) 200nm

PbSe nanowires with different shape and morphology have also been synthesized. During the synthesis, surfactants, reaction temperature, growth time, Pb:Se ratio and concentration all played important roles in the shape control of nanowires. A number of nanowires with different shapes and reaction conditions are shown in Figure 3.3. The mechanism for the formation of final elongated products can be explained using the

106

hypothesis of dipole moment induced oriented attachment of nanocrystals[15], which suggests the dipolar interaction of nanocrystal provides the driving force for the nanocrystals to attach to each other in a specific direction. Taking branched nanowires for example, it first formed star shape PbSe nanocrystal with the assistance of co-surfactant as described in the last paragraph. PbSe nanocrystals are believed to possess a dipole moment because they lack central symmetry due to noncentrosymmetric distribution of Pb and Se terminated {111} facets[15]. The dipolar interaction will then drive the alignment and assembly of nanocrystals along its direction under high growth temperature. TEM images presented in Figure 3.3 confirmed this hypothesis. In Figure 3.3(b), which was at the earlier stage of nanowires formation, the star shape nanocrystals started to attach along <100> crystallographic direction, and formed nanorods and short nanowires. As the chaining process continued, the majority of nanocrystals would attach to each other, forming long branched nanowires. (Figure 3.3(e))

So far, through adjusting co-surfactant, reactants ratio/concentration and reaction temperature and growth time, PbSe NCs with excellent tunability in size and NWs in different shapes has been synthesized. The next step would be exploration of this material in solar cell applications.
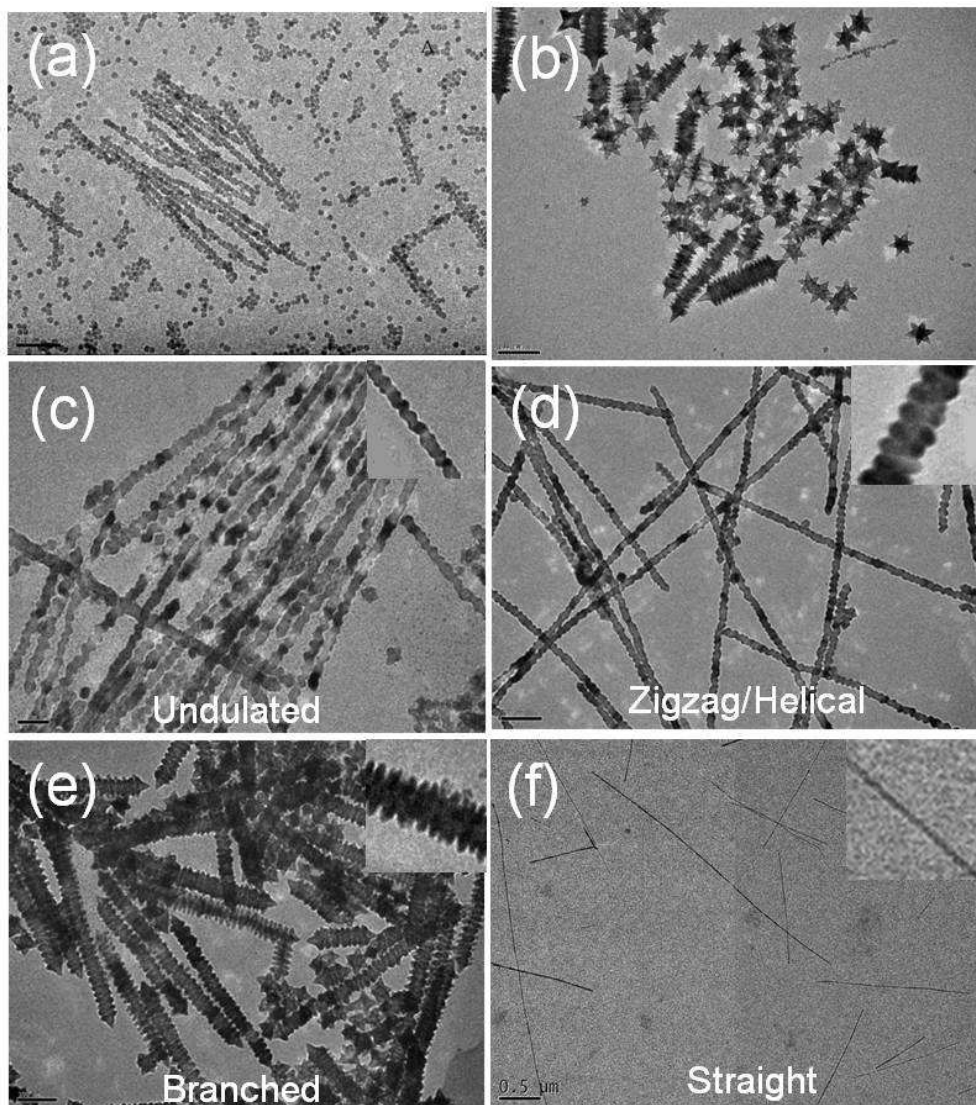
**Figure 3.3.** TEM image of (a) Chaining process begins with quasi-spherical nanocrystal as building blocks (b) Chaining process of star shape nanocrystal as building blocks (c) Undulated nanowires (d) Zigzag/Helical nanowires (e) Branched nanowires (f) Straight nanowires. Inset shows a zoom-in view of the nanowires. (co-surfactants used for each shape: undulated (no co-surfactant); zig-zag/helical (hexadecylamine); star shape branched (octanoic acid); straight (n-tetradecylphosphonic acid); Scale bar: (a) 100nm (b) 100nm (c) 50nm (d) 100nm (e) 100nm (f) 500 nm

108

### 3.3.2 Current-Voltage Characterization and Photovoltaic Performance Comparison

Bulk heterojunction solar cells were fabricated and characterized with the device structure of ITO/PEDOT:PSS/P3HT:PbSe/LiF/Al. A thin layer of LiF (1nm) was used to reduce the work function of Al from 4.2 eV to 3.5 eV[22] to facilitate electron injection. The PEDOT:PSS serves as hole transport layer and smoothes the surface between ITO and active layer[23, 24]. Figure 3.4(a) shows the I-V curves of the devices for P3HT:PbSe blends with the typical photovoltaic performance. These devices demonstrated a low power conversion efficiency of 0.01-0.08% with $I_{sc}$ of 0.2-0.8 mA/cm$^2$ $V_{oc}$ of 0.25-0.35 V and FF of 0.25-0.38. This result is consistent with the performance of P3HT:PbSe based solar cells published by other researchers[5,7,8]. The variation of devices' characteristics arises from several factors: 1) quality of PbSe nanocrystals varies. Due to the nature of wet-synthesis, the nanocrystals from different batches exhibited a small difference in size and concentration; 2) stock condition of PbSe nanocrystals solution. PbSe nanocrystals are sensitive to oxygen and may be oxidized with ambient air contact, which in turn leads to the formation of lead oxides and the loss of ligands and Pb atoms and therefore reduces the size of the nanocrystals[25, 26]. Surface oxygen can also potentially p-dope the PbSe nanocrystals to switch the polarity of nanocrystals[27]; (3) variations in the mixing and processing condition of device fabrication. TEM image (Figure 3.4(b)) was used to indicate the dispersity of PbSe nanocrystals in P3HT polymer matrix as in the film. PbSe formed superlattice and aggregation in small areas and may cause microscopic non-uniformity in the electrical properties across the interface.

Based on the poor energy conversion efficiency which was lower than 0.1%, we hypothesized that sufficient charge separation may not exist between P3HT and PbSe, in which case a solar cell with P3HT alone as the active material will display a similar efficiency. To investigate the role of P3HT and PbSe nanocrystals, control devices of P3HT, PbSe, and P3HT/PCBM have been fabricated and studied. Schottky solar cells were fabricated with the device structure of ITO/PEDOT:PSS/P3HT/LiF/Al. In this configuration, the charge separation mainly occurs at the interface between P3HT and metal electrode (Al). The P3HT devices demonstrated a power conversion efficiency of 0.04% with $I_{sc}$ of 0.4 mA/cm$^2$ and $V_{oc}$ of 0.3 V, and FF 0.35, which is in a comparable range with the performance of P3HT/PbSe heterojunction solar cells. These results indicate that PbSe nanocrystals may not provide the expected function as n-type material to introduce charge separation at the interface between P3HT and PbSe, while the charge separation occurs predominantly at the interface between P3HT and LiF/Al. PbSe Schottky solar cells have also been fabricated. However, the devices exhibited poor performance and shortcuts because of the rough surface in these early devices. To understand and compare an n-type material, PbSe nanocrystal was replaced with PCBM as the electron acceptor and solar cells based on P3HT and PCBM blends with same device layout were fabricated. PCBM is an excellent solution processable electron acceptor, with high electron affinity to support efficient charge separation at the p-n heterojunction[28-29]. Current-voltage characterization demonstrated a high power conversion efficiency of 2.9% with Isc of 13.9 mA/cm$^2$, Voc of 0.46 V and FF of 0.45 as shown in Figure 3.4(d). The efficiency is nearly two-order of magnitude higher than that of P3HT:PbSe solar cells (0.01-0.08%). The large discrepancy between P3HT:PbSe and

P3HT:PCBM performance as bulk heterojunction solar cells and the similarity between P3HT:PbSe and P3HT performance provide the first evidence of the absence of charge separation between P3HT and PbSe. And we conclude that, for the PbSe NCs with specific size range we used (4-10 nm in diameter), P3HT:PbSe devices essentially function as single layer Schottky solar cells, rather than the expected heterojunction solar cells.
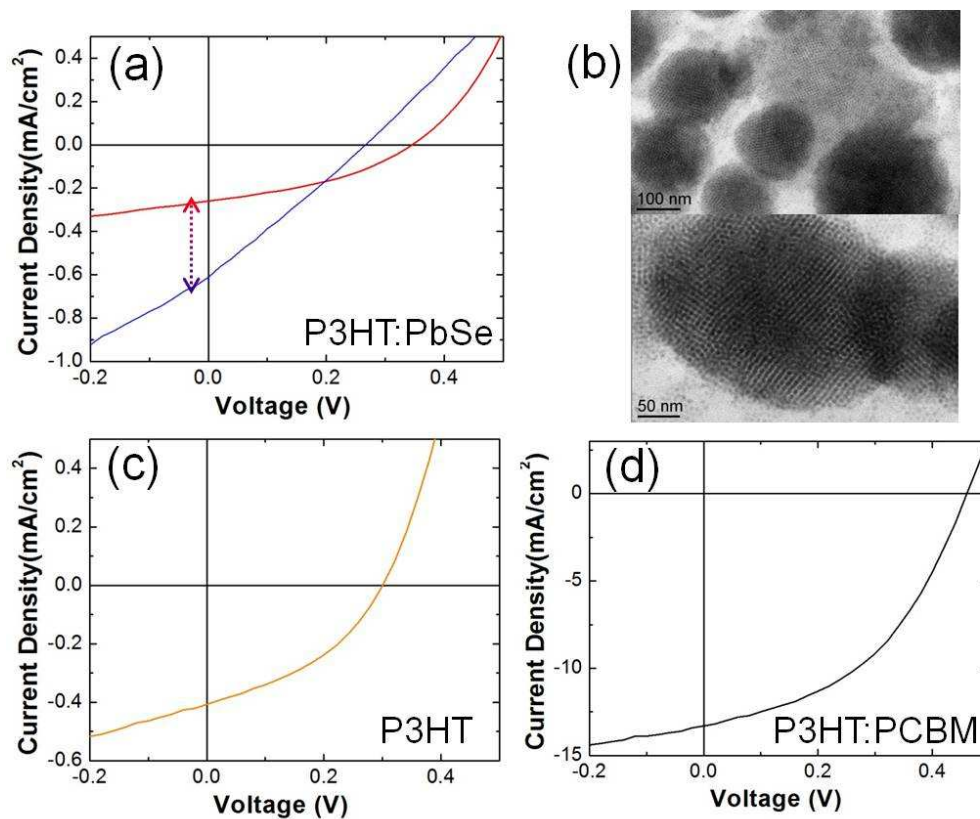


**Figure 3.4.** (a) Representative current-voltage characteristics of P3HT:PbSe (red-blue shows device performance variation) hybrid solar cells (b) TEM image of P3HT:PbSe nano-composites, which represents the blends for P3HT:PbSe solar cell (c) Current-voltage characteristics of P3HT Schottky solar cells (d) Current-voltage characteristics of

P3HT:PCBM bulk heterojunction solar cells. All devices were tested under the illumination of AM 1.5G, 100 mW/cm$^2$.

### 3.3.3 Optical Study

To investigate whether there is photoinduced charge transfer between PbSe quantum dots and P3HT, photoluminescence (PL) quenching[30] experiments were employed. P3HT has a strong spontaneous emission in the red region upon optical excitation. When in proximity to another acceptor material, a depletion layer will form at the interface, and therefore charge transfer will lead to the decrease in the intensity of PL signal. In addition, if the acceptor material has smaller bandgap and the absorption spectrum of the acceptor material overlaps with the emission spectrum of the donor material, energy transfer could occur, resulting in the decrease of the intensity of PL signal. The donor-acceptor interfaces between 1) P3HT and PbSe and 2) P3HT and PCBM were compared. In Figure 3.5(b), the PL spectra of the P3HT film and a blend of P3HT and PCBM film showed that the PL of P3HT is quenched by nearly 80% when mixed with PCBM, compared with that of a pristine P3HT film. This indicates effective charge transfer between the two components, which is consistent with previous current-voltage characterization results of high efficiency solar cells. In contrast, in Figure 3.5(d), the PL spectra of P3HT and the P3HT:PbSe blended films show only 10-20% quenching in the PL signal. This small reduction more likely results from 1) absorption or scattering by PbSe and/or 2) the slight difference in film thickness (absorption peak of P3HT is slightly higher than that of P3HT:PbSe blend film (Figure 3.5(c)). The lack of PL quenching indicates the absence of both energy and charge transfer. We believe that there are two main factors which attribute to the lack of PL quenching and poor solar cell performance:

1) long oleate capping ligands around the PbSe nanocrystals surface may serve as an electrical insulating layer between PbSe and P3HT; 2) energy level alignment of P3HT and PbSe may not be suitable to form a type-II heterojunction for the efficient photoinduced charge separation at the interface. Both factors have been investigated and will be discussed in the next two sections.
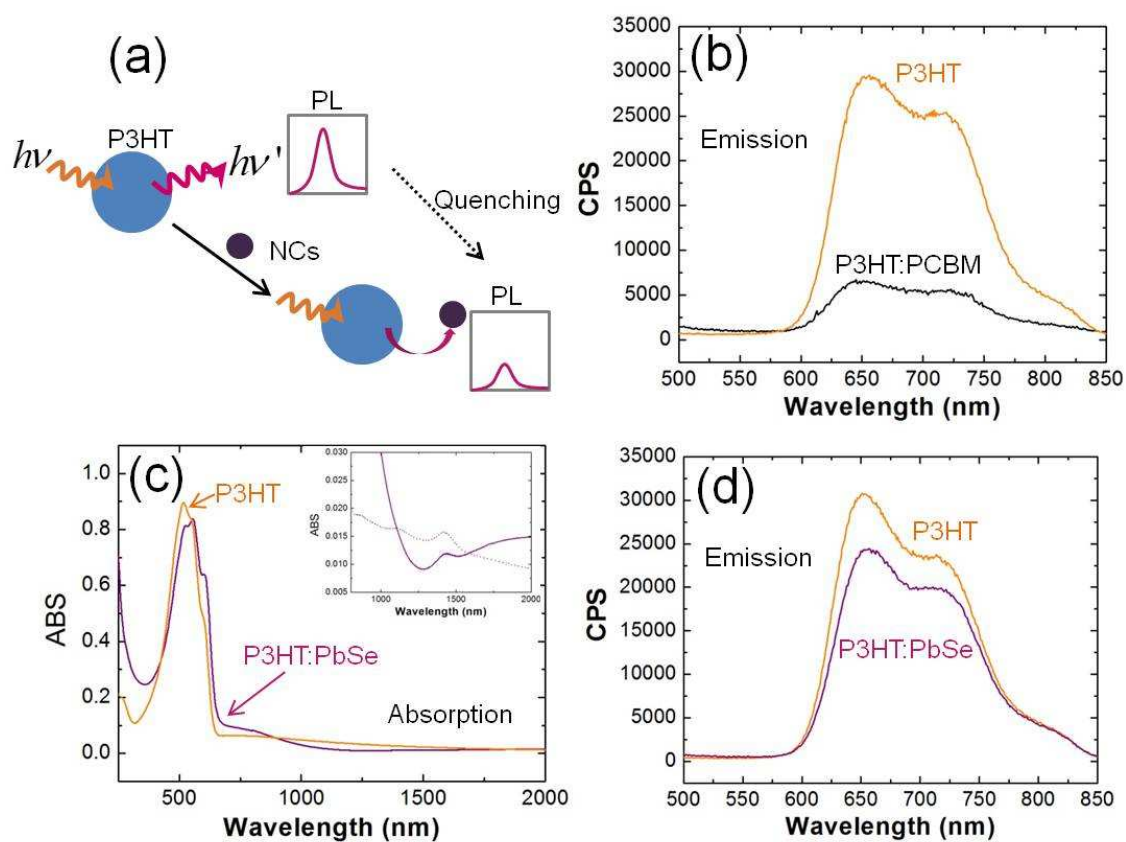


**Figure 3.5.** (a) Schematic diagrams showing the photoluminescence quenching process. (b) Photoluminescence spectrum, showing photoluminescence of pristine P3HT thin film is significantly quenched in the presence of PCBM (c) UV-Vis absorption spectra of P3HT and P3HT:PbSe film (d) Photoluminescence spectrum, showing no significantly quenching in the presence of PbSe.

113

### 3.3.4 Direct Synthesis of PbSe Nanocrystals in P3HT and Photovoltaic Application

To minimize the insulating effect of oleate surfactant, oleic acid free synthesis has been developed. The long oleate capping ligands around the PbSe nanocrystals surface may hinder charge transfer between the polymer and nanocrystals and cause the poor device performance. A novel method of synthesizing PbSe NCs/NWs using P3HT as the surfactant instead of oleic acid has been explored. In this synthesis, the electron donating sulfur of P3HT is anticipated to bind to Pb, forming a similar structure as lead oleate precursor. During the reaction, its long hexyl side chains will provide necessary steric hindrance to stabilize nanocrystal, aid growth and prevent large scale phase separation and precipitation. The as-synthesized PbSe:P3HT nano-composites can be readily used for solar cell fabrication without further treatment.

As the TEM image shown in Figure 3.6 (a), PbSe NCs elongated dots/short rods was obtained from synthesis with dimethylsulphoxide (DMSO) and dichlorobenzene (DCB) as co-solvents. And interestingly, the samples with short rods grow into microns long nanowires at room temperature after sitting for 24 hours in the glovebox (Figure 3.6(b)). As a comparison, PbSe synthesized with oleic acid is typically stable over weeks. The shape evolution is believed to result from dipole induced oriented attachment and colloidal self-assembly of the PbSe nanocrystals[31] with weaker binding P3HT surfactant. Since DMSO is a coordinating solvent and P3HT has good solubility in dichlorobenzene, it is possible that the bound P3HT surface ligands are gradually released from the PbSe surface, promoting the growth of nanowires. Star/snow flake shape PbSe nanocrystals were obtained from synthesis with 1-octadecene, a high boiling point non-coordinating

solvent. The difference in nanocrystal shape and morphology could be attributed to 1) different coordinating properties[32] and 2) different polarity of two solvent systems[33].
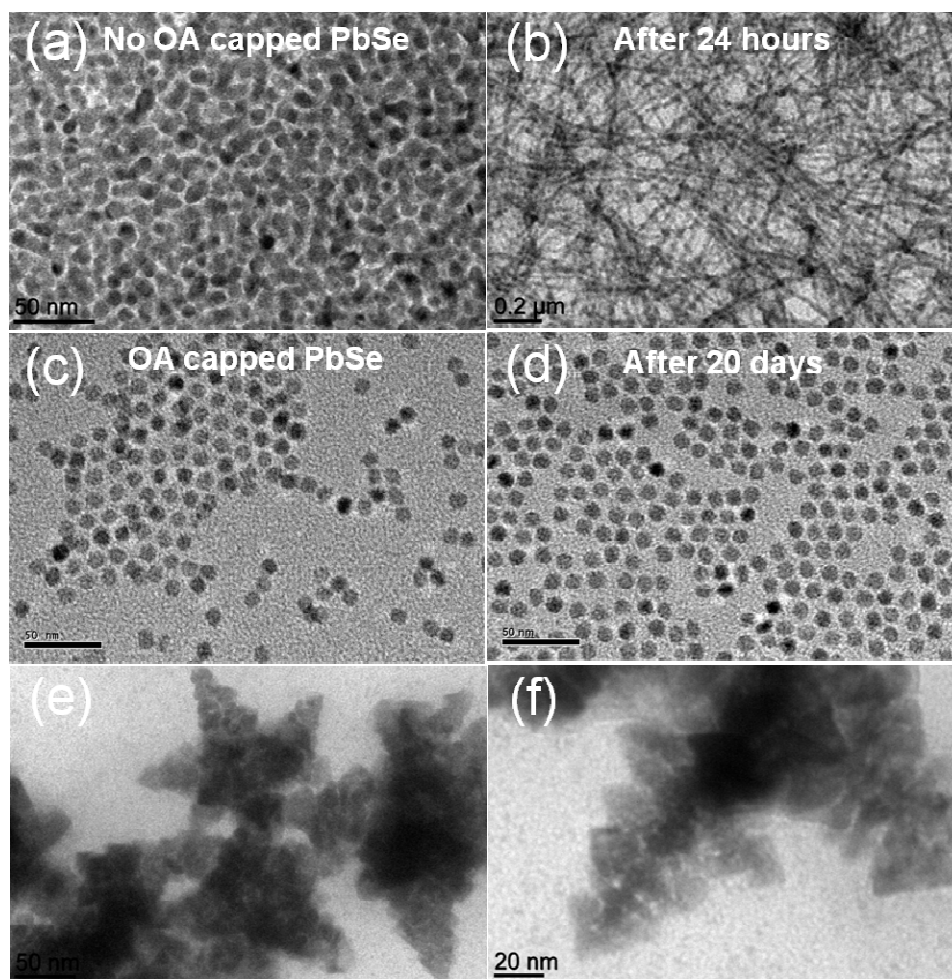


**Figure 3.6.** TEM image of (a) as-synthesized PbSe nanocrystals with P3HT as a surfactant and an anhydrous solution of dimethylsulphoxide (DMSO) and dichlorobenzene (DCB) (1:2 volume ratio) as the reaction solvent (b) sample **a** after sitting in the glovebox for 24 hours (c) oleic acid (OA) capped PbSe nanocrystals (d) sample **c** after sitting in the glovebox for 20 days (e,f) as-synthesized PbSe nanocrystals with P3HT as reaction surfactant using the high boiling point solvent, 1-octadecene(ODE)

115

as the reaction solvent. Scale bar: (a) 50nm (b) 200nm (c) 50nm (d) 50nm (e) 50nm (f) 20nm

Figure 3.7(a) shows X-ray diffraction (XRD) data of as-synthesized PbSe nanocrystal-P3HT composite (DMSO:DCB as solvents) and standard pattern for bulk PbSe structure (JCPDS card no. 6-0354). The strong (100) diffraction peak intensity around $2\theta = 5.4°$ and the higher order (200) diffraction peak at $2\theta = 10.8°$ indicates good semi-crystallinity for P3HT. The other 3 intense and sharp diffraction peaks can be assigned to (111), (200), and (220) planes corresponding to the bulk cubic structure of PbSe indicating high crystallinity of the nanocrystal.

To compare the performance of oleic acid free synthesized PbSe with previous experiment results, bulk heterojunction solar cells were fabricated and characterized. The as-synthesized P3HT:PbSe composite was washed with hexane, re-dispersed in chloroform and spin-coated on the ITO/PEDOT following standard fabrication procedure. Figure 3.7(b) shows the I-V curves of the devices for P3HT:PbSe composites. Unfortunately, these devices only demonstrated a low power conversion efficiency of 0.015% with $I_{sc}$ of 0.15mA/cm$^2$, $V_{oc}$ of 0.4 V, and FF of 0.25. Therefore, removing oleate capping ligands did not improve P3HT:PbSe devices performance. Further characterization is needed to determine if the direct synthesis of P3HT/PbSe is a promising route for solar cell applications.
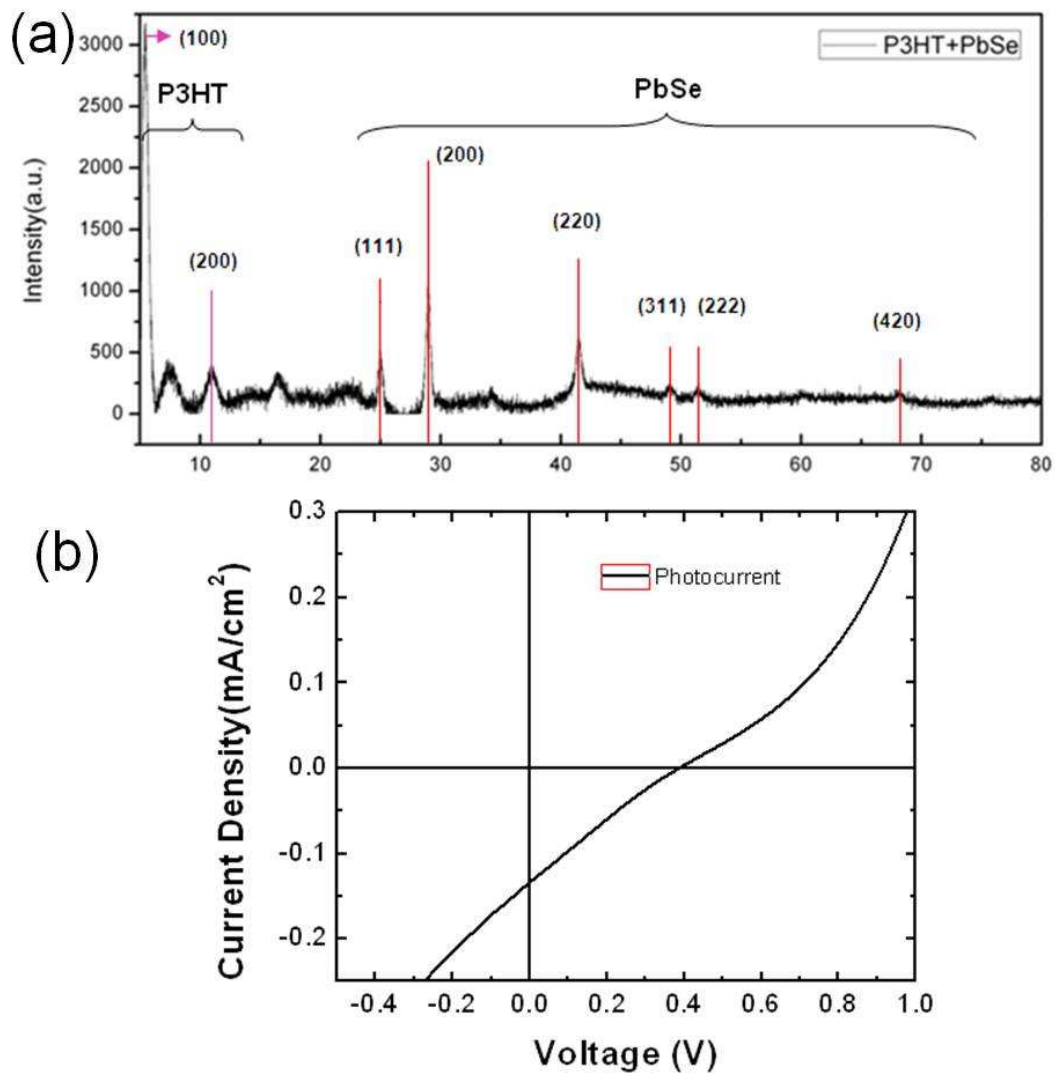
**Figure 3.7.** (a) XRD pattern of PbSe synthesized in P3HT. JCPDS card no. 6-0354 for bulk PbSe structure is marked with red line for reference. (b) Current-voltage characteristics. As-synthesized solution was precipitated with hexane and then re-dispersed in chloroform, and then was used as the active layer for a solar cell device.

### 3.3.5 Ligand Exchange of Wet Synthesized PbSe Nanocrystals and Characterizations

One critical requirement for sufficient charge separation and transfer is the formation of favorable type II band alignment. To better align the energy levels of PbSe with P3HT, surface ligand exchange has been explored to tune the energy level positions of PbSe nanocrystals. A variety of organic molecules have been explored to adjust the energy levels/band position by introducing surface dipoles[34, 35]. However, most research has focused on the modification on 2-D bulk surfaces, with only a few research groups reporting successful band shifting controlled by ligand exchange treatment for colloidal nanocrystals such as InAs[36] and PbSe NWs[37]. Here we explored 6 commonly used ligands, ethanethiol, thiophenol, benzenedithiol, ethanedithiol, pyridine, and hydrazine. Thiolates, pyridine and hydrazine have demonstrated the ability to tune the band position or to modify the surface and enhance the charge transfer at the interface[36, 38-40]. Figure 3.8 depicts surface ligand exchange process with ethanethiol.
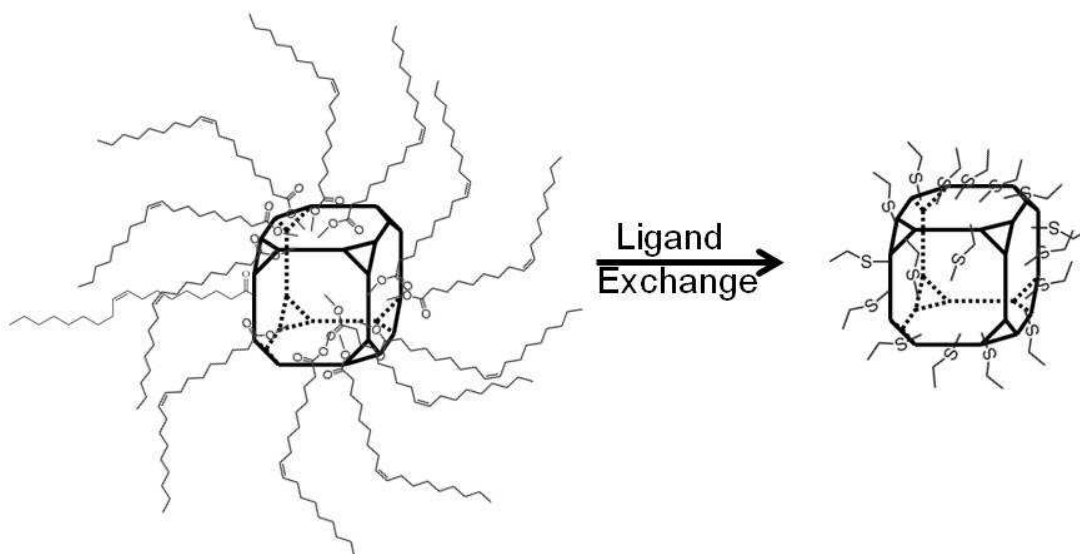
**Figure 3.8.** Schematic of surface ligand exchange process, showing the oleate ligands on PbSe surface replaced by much shorter thiolate. (Besides the dominated oleate ligands, 0-5% of TOP may also be presented as capping agent[26], which is omitted here in the cartoon.)

UV-Vis spectra of PbSe nanocrystal films have been measured to verify the preservation of quantum confinement after ligand exchange. Samples exchanged with ethanethiol, thiophenol, ethanedithiol, benzenedithiol and hydrazine retained most of the quantum confinement. However, the peak position and width has changed to different extents in these samples, among which ethanedithiol, benzenedithiol and hydrazine treated samples exhibit broader peaks post-exchange. Also, the absorption of PbSe was shifted to the red region, indicating possible aggregation and enhanced electronic coupling of nanocrystal during the treatment[6]. Among all six treatments, the pyridine exchanged sample lost quantum confinement, indicated by the largest broadening in both the red and blue regions, which could be attributed to 1) the increase in the nanocrystal

size distribution; 2) the additional wave function distortion caused by surface charges[41]; and 3) enhanced interparticle electronic coupling, which arises from the proximity of nanocrystals with shorter surface ligands[42].
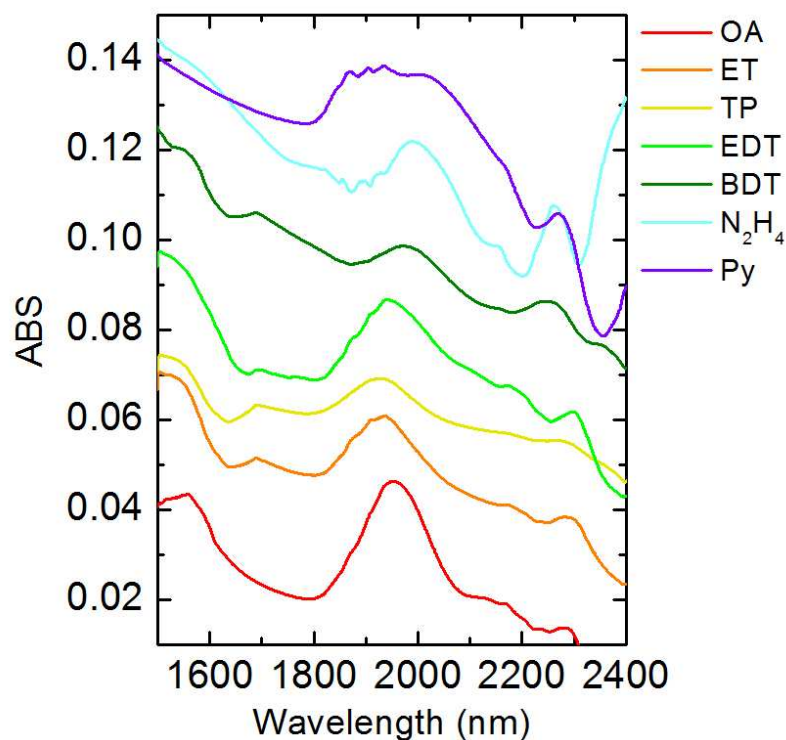


**Figure 3.9.** UV-Vis absorption spectra of PbSe nanocrystal films on quartz with different capping ligands (OA: oleic acid, ET: ethanethiol, TP: thiophenol, BDT: benzenedithiol, EDT: ethanedithiol, N2H4: hydrazine and Py: pyridine)

Electrochemical measurements were used to study the electronic structure of PbSe before and after ligand exchange, and to characterize the alignment of its energy levels relative to P3HT. Figure 3.10(a-c) shows cyclic voltammograms collected for drop cast films of PbSe nanocrystals with different capping ligands on a platinum working

electrode. The HOMO value was derived based on the oxidation peak. For benzenedithiol, the peak onset (relative to oleate capped PbSe) has been used to calculate the HOMO value because of the broadening of peak. The LUMO value was calculated by adding the optical bandgap to the HOMO value. The results are summarized in Table 3.1. Based on these measurements, most of the PbSe samples (OA capped or ligand exchanged) do not provide favorable energy levels to form type-II heterojunction with P3HT, which has LUMO of -3.1eV and HOMO of -5.1 eV. Only benzenedithiol and pyridine exchanged samples indicate a favorable shift moving the bandgap below 5.1eV (P3HT HOMO). However, this is not sufficient to claim that the exchanged PbSe forms a type-II heterojunction with the commonly studied polymers P3HT. The reasons include: 1) even for the lowest HOMO obtained, -5.17eV is close enough to P3HT HOMO (-5.1eV) and charge transfer direction remains unknown; 2) the P3HT HOMO value is calculated based on the onset of peak, and there are a lot of debates on the real value relative to vacuum[7, 8, 43]; 3) influences of solvents, ions, and surface effects are present in electrochemical measurements, and interfacial chemistry and interactions between the materials in blends in working solid-state devices also play important roles for band alignment[44]. Consistent with these complications, the devices I-V characterization with exchanged PbSe didn't show any improvements to suggest the existence of photo-induced charge transfer at the interface. These findings about the lack of induced charge transfer is consistent with the results reported by Ginger et al.[45] around a similar time.

**Table 3.1**. Optical and electrochemical properties of PbSe after ligand exchange

| Modifying Ligand | Absorption (nm) | HOMO (eV) | LUMO (eV) | $E_g$ (eV) |
|---|---|---|---|---|
| oleic acid | 1955 | -5.02 | -4.39 | 0.63 |
| ethanethiol | 1938 | -4.97 | -4.33 | 0.64 |
| thiophenol | 1930 | -5.06 | -4.42 | 0.64 |
| ethanedithiol | 1940 | -5.04 | -4.4 | 0.64 |
| benzenedithiol | 1970 | -5.17 | -4.54 | 0.63 |
| hydrazine | 1989 | -5.02 | -4.4 | 0.62 |
| pyridine | 1950 | -5.14 | -4.5 | 0.64 |
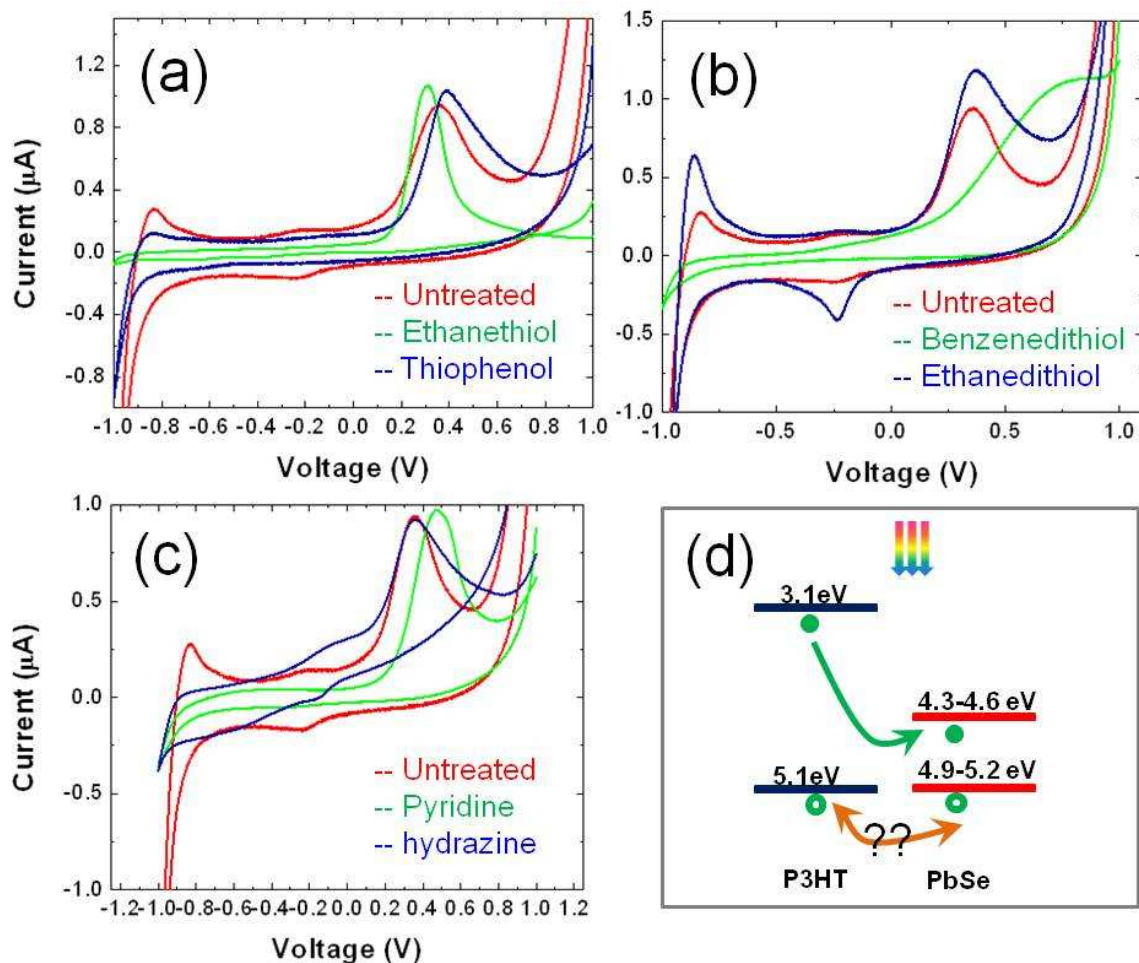
**Figure 3.10.** (a-c) Cyclic voltammograms of OA capped (untreated) PbSe and ligand exchanged PbSe with different ligands, measured as a thin film on a platinum working electrode in an acetonitrile solution of 0.01 M TBAPF$_6$. (d) Energy level alignment of P3HT and PbSe (with various treatment), value derived from cyclic voltammograms, in reference to vacuum.

## 3.4 Conclusion

In conclusion, we explored the synthesis and photovoltaic application of PbSe nanocrystals in combination with P3HT and discussed the charge transfer at the interface.

Wet chemical routes were used to synthesize PbSe nanocrystals tunable in size and shape by tailoring the reaction temperature, growth time and selection of surfactants. PbSe nanowires were also synthesized through oriented attachment in solution of nanocrystal building blocks to form straight, zigzag, helical, and branched nanowires. Near-IR sensitive PbSe nanocrystals were integrated with the organic semiconductor P3HT to fabricate organic-inorganic bulk heterojunction solar cells. Even after optimization, solar cell performance was poor, with efficiency around 0.05% which is similar to the performance of P3HT Schottky cell. And this efficiency is consistent with the values reported by other researchers using PbSe nanocrystal and polymer blends in heterojunction solar cells. The low and comparable efficiency of P3HT/PbSe devices and P3HT only devices suggests that the working mechanism for P3HT/PbSe blends lean towards Schottky diode solar cells rather than the bulk heterojunction solar cells as previously expected. Consistent with that, results of photoluminescence quenching experiments also suggested a lack of charge transfer in blends of PbSe NCs and P3HT. Long oleate capping ligands on PbSe surface serve as an insulating layer and may hinder the charge transfer at the interface. To minimize its influence, a novel route of direct synthesis of PbSe nanocrystal/nanowires in polymer P3HT solution without oleic acid and postsynthetic solid exchange with short capping ligand to replace oleic acid has been explored. However, the direct synthesized PbSe/P3HT blends did not yield better device performance, indicating that the oleate insulation may not be the only cause of the low performance. Electrochemical and current-voltage characterization reveals a misalignment of the two materials and a possible type I band alignment, which is unfavorable for charge separation in solar cell application. Nanowires typically exhibit

narrower bandgap than that of nanocrystal because of the large size of the core (diameter of nanowires).[4] So it will move the band towards even more unfavorable position (higher lying HOMO of acceptor) for type II heterojunction formation, which is the reason why we decide not to further pursue the application of PbSe nanowires in the P3HT:PbSe hybrid solar cells. Therefore we conclude that the absence of photoinduced charge transfer and misalignment of energy levels in P3HT/PbSe system suggests incompatibility of these two materials to form efficient heterojunction solar cells for the specific PbSe NCs size range (4-10 nm) that we used. It is worth to mention that, by introducing PbSe NCs with even smaller size (1-3 nm), it is possible to increase the bandgap and shift the HOMO level of PbSe towards a more favorable position when combined with P3HT. Recently, the Alivisatos lab reported the improvement of open circuit voltage and significant enhancement of PbSe Schottky device performance using the concept of "ultrasmall" size NCs[46]. And for PbSe NCs/P3HT solar cell devices, adopting NCs with ultrasmall sizes could potentially overcome the band mismatch challenge. Beyond the ligand exchange work shown above, FT-IR and photocurrent measurements will be useful to understand surface chemistry and how interface structure affects charge transfer and carrier recombination. Time-resolved microwave conductivity measurements and photoinduced absorption spectroscopy will also give a better understanding of photoinduced charge separation at the interface between the nanocrystal and P3HT. Direct synthesis in P3HT provides a promising approach for many wet chemical nanocrystal synthesis. The self-assembly process and dipole induced attachment should be further investigated to have a better control over size and shape to tune the optical and electrical properties. The Se precursor, TOPSe, can be replaced with TBPSe

(tributyl phosphine selenide) to study the role of TOP ligands in this synthesis route. Oriented dipole induced attachment in polymer solution under electric field with either a lateral or vertical structure may provide us new understanding of the assembly mechanism, charge transport and charge transfer (for example, monitoring PL quantum yield and decay for polymer when slowly annealing quantum dot in polymer matrix), and opportunity for interesting applications such as organic light emitting field effect transistors.

## 3.5 References

1. Zhou, Y.; Eck, M.; Kruger, M. *Energy & Environmental Science* **2010,** 3, (12), 1851-1864.

2. Palaniappan, K.; Murphy, J. W.; Khanam, N.; Horvath, J.; Alshareef, H.; Quevedo-Lopez, M.; Biewer, M. C.; Park, S. Y.; Kim, M. J.; Gnade, B. E.; Stefan, M. C. *Macromolecules* **2009,** 42, (12), 3845-3848.

3. Xu, T.; Qiao, Q. *Energy & Environmental Science* **2011,** 4, (8), 2700-2720.

4. Huynh, W. U.; Dittmer, J. J.; Alivisatos, A. P. *Science* **2002,** 295, (5564), 2425-2427.

5. Fritz, K. P.; Guenes, S.; Luther, J.; Kumar, S.; Sariciftci, N. S.; Scholes, G. D. *Journal of Photochemistry and Photobiology A: Chemistry* **2008,** 195, (1), 39-46.

6. Liu, Y.; Gibbs, M.; Puthussery, J.; Gaik, S.; Ihly, R.; Hillhouse, H. W.; Law, M. *Nano Letters* **2010,** 10, (5), 1960-1969.

7. Cui, D.; Xu, J.; Zhu, T.; Paradee, G.; Ashok, S.; Gerhold, M. *Applied Physics Letters* **2006,** 88, (18), 183111.

8. Xiaomei Jiang, R. D. S., Sergey B. Lee, Jeffrey M. Pietryga, Victor I. Klimov and Anvar A. Zakhidov *Journal of Materials Research* **2007,** 22, 2204-2210

9. Ellingson, R. J.; Beard, M. C.; Johnson, J. C.; Yu, P.; Micic, O. I.; Nozik, A. J.; Shabaev, A.; Efros, A. L. *Nano Letters* **2005,** 5, (5), 865-871.

10. Semonin, O. E.; Luther, J. M.; Choi, S.; Chen, H.-Y.; Gao, J.; Nozik, A. J.; Beard, M. C. *Science* **2011,** 334, (6062), 1530-1533.

11. Borchert, H. *Energy & Environmental Science* **2010,** 3, (11), 1682-1694.

12. Talapin, D. V.; Murray, C. B. *Science* **2005,** 310, (5745), 86-89.

13.  Radychev, N.; Lokteva, I.; Witt, F.; Kolny-Olesiak, J.; Borchert, H.; Parisi, J. r. *The Journal of Physical Chemistry C* **2011,** 115, (29), 14111-14122.

14.  Li, G.; Shrotriya, V.; Huang, J.; Yao, Y.; Moriarty, T.; Emery, K.; Yang, Y. *Nat Mater* **2005,** 4, (11), 864-868.

15.  Cho, K.-S.; Talapin, D. V.; Gaschler, W.; Murray, C. B. *Journal of the American Chemical Society* **2005,** 127, (19), 7140-7147.

16.  LaMer, V. K.; Dinegar, R. H. *Journal of the American Chemical Society* **1950,** 72, (11), 4847-4854.

17.  Peng, X.; Wickham, J.; Alivisatos, A. P. *Journal of the American Chemical Society* **1998,** 120, (21), 5343-5344.

18.  Ostwald, W. *Lehrbuch der Allgemeinen Chemie* **1896,** 2, (1).

19.  Vengrenovich, R.; Gudyma, Y.; Yarema, S. *Semiconductors* **2001,** 35, (12), 1378-1382.

20.  Houtepen, A. J.; Koole, R.; Vanmaekelbergh, D.; Meeldijk, J.; Hickey, S. G. *Journal of the American Chemical Society* **2006,** 128, (21), 6792-6793.

21.  Sliem, M. A.; Chemseddine, A.; Bloeck, U.; Fischer, R. A. *CrystEngComm* **2011,** 13, (2), 483-488.

22.  Eremina, N.; Degtyarenko, K.; Kopylova, T.; Samsonova, L.; Gadirov, R.; Maier, G. *Theoretical and Experimental Chemistry* **2009,** 45, (1), 63-68.

23.  Tengstedt, C.; Crispin, A.; Hsu, C. H.; Zhang, C.; Parker, I. D.; Salaneck, W. R.; Fahlman, M. *Organic Electronics* **2005,** 6, (1), 21-33.

24.  Kirkeminde, A.; Retsch, M.; Wang, Q.; Xu, G.; Hui, R.; Wu, J.; Ren, S. *Nanoscale* **2012,** 4, (15), 4421-4425.

25.     Dai, Q.; Zhang, Y.; Wang, Y.; Wang, Y.; Zou, B.; Yu, W. W.; Hu, M. Z. *The Journal of Physical Chemistry C* **2010,** 114, (39), 16160-16167.

26.     Moreels, I.; Fritzinger, B.; Martins, J. C.; Hens, Z. *Journal of the American Chemical Society* **2008,** 130, (45), 15081-15086.

27.     Oh, S.; Kim, D. K.; Kagan, C. R. *ACS Nano* **2012**, 6, (5), 4328-4334.

28.     Thompson, B. C.; Kim, Y.-G.; McCarley, T. D.; Reynolds, J. R. *Journal of the American Chemical Society* **2006,** 128, (39), 12714-12725.

29.     Newman, C. R.; Frisbie, C. D.; da Silva Filho, D. A.; Brédas, J.-L.; Ewbank, P. C.; Mann, K. R. *Chemistry of Materials* **2004,** 16, (23), 4436-4451.

30.     Sariciftci, N. S.; Smilowitz, L.; Heeger, A. J.; Wudl, F. *Science* **1992,** 258, (5087), 1474-1476.

31.     Zhang, X.; Zhang, Z.; Glotzer, S. C. *The Journal of Physical Chemistry C* **2007,** 111, (11), 4132-4137.

32.     Al-Salim, N.; Young, A. G.; Tilley, R. D.; McQuillan, A. J.; Xia, J. *Chemistry of Materials* **2007,** 19, (21), 5185-5193.

33.     Stavrinadis, A.; Beal, R.; Smith, J. M.; Assender, H. E.; Watt, A. A. R. *Advanced Materials* **2008,** 20, (16), 3105-3109.

34.     Haick, H.; Ghabboun, J.; Niitsoo, O.; Cohen, H.; Cahen, D.; Vilan, A.; Hwang, J.; Wan, A.; Amy, F.; Kahn, A. *The Journal of Physical Chemistry B* **2005,** 109, (19), 9622-9630.

35.     Vilan, A.; Shanzer, A.; Cahen, D. *Nature* **2000,** 404, (6774), 166-168.

36.     Soreni-Harari, M.; Yaacobi-Gross, N.; Steiner, D.; Aharoni, A.; Banin, U.; Millo, O.; Tessler, N. *Nano Letters* **2008,** 8, (2), 678-684.

37. Kim, . K.; Vemulkar, T. R.; Oh, S. J.; Koh, W. K.; Murray, C. B.; Kagan, C. R. *ACS Nano,* 2011, 5 (4), pp 3230–3236.

38. Wu, Y.; Zhang, G. *Nano Letters* **2010,** 10, (5), 1628-1631.

39. Lokteva, I.; Radychev, N.; Witt, F.; Borchert, H.; Parisi, J. r.; Kolny-Olesiak, J. *The Journal of Physical Chemistry C* **2010,** 114, (29), 12784-12791.

40. Graetzel, M.; Janssen, R. A. J.; Mitzi, D. B.; Sargent, E. H. *Nature* **2012,** 488, (7411), 304-312.

41. Law, M.; Luther, J. M.; Song, Q.; Hughes, B. K.; Perkins, C. L.; Nozik, A. J. *Journal of the American Chemical Society* **2008,** 130, (18), 5974-5985.

42. Fafarman, A. T.; Koh, W.-k.; Diroll, B. T.; Kim, D. K.; Ko, D.-K.; Oh, S. J.; Ye, X.; Doan-Nguyen, V.; Crump, M. R.; Reifsnyder, D. C.; Murray, C. B.; Kagan, C. R. *Journal of the American Chemical Society* **2011,** 133, (39), 15753-15761.

43. Solomeshch, O.; Kigel, A.; Saschiuk, A.; Medvedev, V.; Aharoni, A.; Razin, A.; Eichen, Y.; Banin, U.; Lifshitz, E.; Tessler, N. *Journal of Applied Physics* **2005,** 98, (7), 074310.

44. Cardona, C. M.; Li, W.; Kaifer, A. E.; Stockdale, D.; Bazan, G. C. *Advanced Materials* **2011,** 23, (20), 2367-2371.

45. Noone, K. M.; Anderson, N. C.; Horwitz, N. E.; Munro, A. M.; Kulkarni, A. P.; Ginger, D. S. *ACS Nano* **2009,** 3, (6), 1345-1352.

46. Ma, W.; Swisher, S. L.; Ewers, T.; Engel, J.; Ferry, V. E.; Atwater, H. A.; Alivisatos, A. P. *ACS Nano* **2011** 5, (10). 8140-8147

# Chapter 4

# Study of Organic-Inorganic Hybrid Solar Cells Based on P3HT and Thiocyanate-capped CdSe Nanocrystal

**4.1 Introduction**

Organic-inorganic hybrid solar cells offer excellent flexibility for chemical modification and different material combinations to optimize optical and electrical property. For the inorganic component, colloidal semiconductor nanocrystals serve as the most promising candidate for the electron acceptor[1-4]. In Chapter 3, we have investigated P3HT/PbSe system and concluded that the lack of photoinduced charge transfer and misalignment of energy levels in P3HT/PbSe system suggests incompatibility of these two materials for efficient heterojunction solar cells. For the next step, CdSe nanocrystals were investigated to explore the surface chemistry, quantum confinement and processing condition effects on the device performance. Among the inorganic nanocrystal materials, CdSe nanocrystals possesses three distinctive advantages: 1) tunable absorption covering the entire visible spectrum range[5], 2) low lying HOMO and LUMO levels which makes it a good electron acceptor[6] and 3) wet-synthesis route has been established to allow control of the size and shape of CdSe nanocrystals[7, 8]. In theory, P3HT/CdSe hybrid solar cells should perform better than the P3HT/PCBM system due to higher absorption coefficient of inorganic semiconductor nanocrystals and its higher intrinsic electron mobility[9] than that of PCBM[10]. However, the current performance of polymer/nanocrystal hybrid solar cells in the field is relatively poor compared to the polymer/fullerene based devices[3, 4, 11, 12]. Our goal is to adopt different surface treatment methods and new device design to overcome the bottlenecks which limit solar cell efficiency.

One major challenge is to remove the long capping ligands used during the synthesis of CdSe nanocrystals, which works as electrical insulating layers and impedes efficient electron transport in the solar cell. To overcome this drawback, extensive research has

been carried out to develop ligand exchange methods using shorter capping ligands to reduce the interparticle distance and facilitate electron transport within inorganic nanoparticle network and increase charge separation at the polymer-CdSe interface. Materials for ligand exchange, such as pyridine[3, 13], thiols[14, 15], amines[4, 16] and chloride[17] have been investigated and brought the power conversion efficiency to 1.8% for P3HT/CdSe quantum dots (QDs) by utilizing pyridine and butylamine ligand exchange[4]. Recently, several non-ligand-exchange alternative approaches have also been explored to remove the long capping ligands. Zhou and Krüger demonstrated a post-synthetic hexanoic acid wash treatment to remove the long hexadecylamine capping group on CdSe QDs and achieved power conversion efficiency of 2.0% for P3HT/CdSe QDs hybrid devices[18]. The other research effort involves utilizing weak binding ligands that can be removed by thermal treatment or aging. Seo and Prasad reported a thermal decomposition method to cleave the ligands, which improved power conversion efficiency of P3HT:CdSe bulk heterojunction solar cell from 0.21% to 0.44% [19].

Besides surface treatments, the morphology control of nanocrystals has proven to be critical to enhance the power conversion efficiency of solar cells. The ideal nanocrystal structure shall provide high interfacial area for charge separation between donor and acceptor and directional percolation pathways perpendicular to the substrate for electron transfer, as discussed in the previous chapters. Huyuh and Alivisatos have reported a substantial enhancement of CdSe hybrid solar cell efficiency by replacing CdSe quasi-spherical quantum dots with elongated nanorods and achieved an impressive efficiency of 1.7%[3]. In addition, 3-dimentional branched CdSe nanoparticles have also been investigated to further improve the efficiency of hybrid P3HT:CdSe solar cells to 2.2 %[20].

It is worth noting that, besides the optimization of CdSe nanocrystals, several labs have also reported the synthetic efforts on the small organic molecule/polymer components with high hole mobility and extended light absorption for the solar cells which also led to enhancement of device performance[21, 22]. However, these are beyond the scope of our study in this chapter.

Most research effort of efficiency improvement on P3HT and CdSe nanocrystals are based on bulk heterojunction devices. In the bulk heterojunction structure, the challenge of miscibility of organic and inorganic components, the difficulty to control nanoscale morphology, and environmental concerns of the toxicity of commonly used pyridine for ligand exchange treatment, all greatly limit its potential application and call for new strategy.

Here we took advantage of the thiocyanate solution exchange method recently developed by Dr. Aaron Fafarman in our lab, and used orthogonal solvents to fabricate a novel, solution-processable bilayer device via sequential spincoating. This technique provides two distinct advantages to the basic research and applied science field: 1) it allows investigation into the role of the separate components and interfaces in a controllable manner, and 2) in practice, the ability to optimize absorption, mobility and morphology of both layers independently and the ease of sequential solution processes are important for large-scale and low cost manufacturing of organic solar cells. In this chapter, the photovoltaic application of thiocyanate capped CdSe nanocrystals in combination with P3HT in the bilayer device is demonstrated. Several key factors that influence device performance, such as nanocrystal size and intermixing between the two

components (diffuse bilayer heterojunction) will be discussed in detail. Preliminary results of inverted bilayer solar cells will also be discussed.

### 4.2 Experimental Section

### 4.2.1 Synthesis of CdSe Nanocrystals

Cadmium selenide (CdSe) nanocrystals were synthesized by Benjamin T. Diroll from Dr. Christopher B. Murray lab. A modified procedure from literature[8, 23] has been used.

*"In a typical reaction, 20.0 g of trioctylphosphine oxide, 20.0 g of octadecylamine, and 2.1 g of cadmium stearate were dried under vacuum at 120°C for 1 h and then heated to 320°C under nitrogen, whereupon 10.0 mL of 1.25 M selenium in tributylphosphine solution was rapidly injected. Growth was continued at 290°C."[Adapted from Ref.23]*

### 4.2.2 Thiocyanate ligand exchange of CdSe Nanocrystals

The thiocyanate ligand exchange process is adapted from the method developed and published by Aaron T. Fafarman in our lab. For the typical solution exchange, the procedure below was followed[23]:

NH$_4$SCN (Acros, 99.9%) was purified by recrystallization from anhydrous isopropanol. 3-4 mL of NH$_4$SCN solution (100 mM in acetone) was added to 6 mL of a dispersion of CdSe nanocrystal in hexanes (to control the concentration, CdSe solution has been diluted/concentrated to have an optical density around 10 per cm$^3$ of solution at the lowest energy excitonic absorption peak). The mixture was stirred at 3000 rpm for 2 min with vortex mixer. The solution turned cloudy quickly, showing phase separation of CdSe nanocrystals from the solution. Then it was centrifuged 2000 × g for 1 min. After decanting the clear supernatant, CdSe nanocrystals was re-dispersed in 10 mL

tetrahydrofuran (THF), stirred at 3000 rpm for 2 min and then centrifuged $2000 \times g$ for 1 min to precipitate the CdSe nanocrystals, followed by the similar purification process with toluene and finally re-dispersed in dimethylformamide (DMF). The exchanged CdSe nanocrystals in DMF solution is not very stable and starts to precipitate over 1 h because of particle aggregation[23]. So the fresh thiocyanate exchanged CdSe nanocrystals was always used within minutes after ligand exchange. Due to the air sensitivity of CdSe nanocrystals, all steps were performed inside of the nitrogen glovebox.

### 4.2.3 Characterization

Cyclic voltammograms were obtained employing a three electrode C3 cell stand and Epsilon electrochemical workstation. To prepare the sample for CV measurements, CdSe nanocrystals solution was drop-cast onto platinum electrode and dried in the vacuum chamber. Absorption spectra were measured using a Varian Cary 5000 UV-Vis-NIR spectrophotometer. Photoluminescence (PL) spectra were measured on a Fluorolog 3 spectrofluorometer (HORIBA Jobin Yvon, Ltd.) upon excitation at 450 nm. TEM (Transmission electron microscopy) images were obtained using a JEM-1400 at 120kV. AFM (Atomic force microscopy) measurements were carried out using a Digital Instruments Multimode AFM operated in tapping mode.

### 4.2.4 Device Fabrication and Characterization

Both bilayer and bulk heterojunction solar cells have been fabricated. The whole process was performed inside of the nitrogen filled glovebox except for the ITO cleaning step and PEDOT:PSS deposition step.

(1) Regular bilayer solar cells (ITO/PEDOT/P3HT/CdSe/ Al)

The substrate cleaning and PEDOT:PSS deposition was similar as described in Chapter 2. For the active layers, P3HT (5mg/mL in chlorobenzene) was first spin-cast on the PEDOT:PSS coated ITO glass at 1000 rpm for 10 s to 1 min, followed by the spincoating deposition of CdSe nanocrystals at 800 rpm for 1 min from DMF. For the *bilayer* structure, P3HT was annealed before CdSe nanocrystals deposition at 140°C for 10 minutes followed by CdSe nanocrystals deposition and a $2^{nd}$ annealing at 140°C for 10 minutes. For the *diffuse bilayer* structure, P3HT was kept wet without any annealing before depositing the CdSe layer. Then the active layer (P3HT/CdSe) was simultaneously annealed at 140°C for 20 minutes. A back electrode of 80 nm aluminum (Al) as cathode was deposited as described in Chapter 2.

(2) Inverted bilayer solar cell (ITO/TiO$_2$/CdSe/P3HT/Au)

The substrate cleaning was similar as described in Chapter 2. After thoroughly cleaning, a 40 nm TiO$_2$ was deposited by the Atomic Layer Deposition (ALD, Cambridge Nanotech Savannah 200) on the ITO glass at 200°C to modify the ITO for electron injection. Then the ITO/TiO$_2$ electrode was transferred into glovebox, and a thin layer (approx. 40 nm) of CdSe nanocrystals was spin-cast on top of TiO$_2$, followed by the deposition of P3HT layer and annealing at 140°C. A back electrode of 60-80 nm gold (Au) as anode was deposited through the shadow mask.

(3) Heterojunction solar cells (ITO/PEDOT/pentacene:CdSe/Al)

The substrate cleaning and PEDOT:PSS deposition was similar as described in Chapter 2. For the active layer mixture, 1 volume of pentacene precursor (13,6-N-sulfinylacetamidopentacene) dissolved in chloroform (15mg/mL) was mixed with 1 volume of thiocyanate capped CdSe nanocrystals in DMF (optical density around 60),

followed by the spincasting of this mixture onto the PEDOT:PSS layer. Then the devices were baked at 200 °C for 90 s to anneal the device and convert the pentacene precursor (13,6-N-sulfinylacetamidopentacene) to pentacene. A back electrode of 80 nm aluminum (Al) as cathode was deposited as described in Chapter 2.

Current-voltage characteristics of the photovoltaic cells were acquired using a Keithley 2400 source-meter under the illumination of AM 1.5G solar simulated light (1 sun, 100 mW/cm$^2$) in air or in sealed nitrogen cell.

## 4.3 Results and Discussions

## 4.3.1 Effect of CdSe Nanocrystal Size on Bilayer Devices Performance

To enhance photoconductivity of CdSe nanocrystals and facilitate charge transfer between CdSe nanocrystals and P3HT, solution ligand exchange with thiocyanate has been used to replace the traditional pyridine exchange approach. Wet-chemically synthesized CdSe nanocrystals are often capped with long, insulating surfactants such as trioctylphosphine oxide or oleic acid or octadecylamine. We have used NH$_4$SCN for the exchange in which the thiocyanate replaces the original capping group. Prior to exchange, CdSe nanocrystals are passivated by different types of ligands with a hydrophobic tail of one or several alkyl chains which form stable suspension in non-polar solvents such as hexane or toluene. After ligand exchange, the capping hydrophobic ligands are replaced by thiocyanate, causing the CdSe nanocrystals to precipitate out from non-polar solvents. After adding polar solvents such as DMF and DMSO, short, negatively charged thiocyanate can dissociate from the surface of the nanocrystal and form electrostatic double layer with the localized positive charges on the nanocrystal surface, which

138

stabilizes the nanocrystal dispersion in solvents via electrostatic repulsion[23]. Therefore thiocyanate capped CdSe nanocrystals will only be dispersible in polar solvents.

Figure 4.1(a,b) shows the schematic of device layout and the energy level diagram constructed from the reported work functions of electrode materials ITO/PEDOT:PSS and Al[24, 25], and reported HOMO and LUMO energies derived from cyclic voltammograms for CdSe nanocrystals and P3HT[6]. When blended with P3HT, both HOMO and LUMO of CdSe nanocrystals lies below those of P3HT, forming an effective type II heterojunction at the P3HT and CdSe nanocrystals interface with 0.1-0.4 eV LUMO offset for efficient exciton separation and charge transfer and a high built-in potential (1.6-1.9 eV) that is larger than the built in potential of the extensively studied P3HT:PCBM system (0.7-1.3 eV as calculated from the reported ranges for the HOMO level of P3HT and the LUMO level of PCBM), which is favorable to increase the open circuit voltage[26, 27]. Absorption and photoluminescence spectra of P3HT and CdSe nanocrystals (approx. 4.5 nm in diameter) in thin film are shown in figure 4.1(c).

To investigate whether thiocyanate ligand exchange affects the size distribution of CdSe nanocrystal, the absorption spectrum of CdSe film before and after ligand exchange was characterized. Before ligand exchange, the synthesized CdSe nanocrystals exhibit fine resolution of the second excitonic peak and narrow full width at half-maximum (FWHN, 30 nm) of emission peak, indicating that the CdSe nanocrystal has a narrow size distribution. The first exciton peak occurs at 599 nm for the as-synthesized raw CdSe nanocrystal thin film. After the thiocyanate ligand exchange, the first exciton absorption peak of CdSe thin film is shifted to 606nm. The 7nm red shift of the first excitonic peak suggests enhanced interparticle electronic coupling, which arises from the proximity of

nanocrystal with shorter surface ligands[28]. The narrow first exciton peak indicates the thiocyanate ligand exchange process preserved the quantum confined optical property and narrow size distribution of CdSe nanocrystals.

The shift between absorption peak and photoluminescence peak is known as the Stokes shift. CdSe nanocrystals exhibit a small Stokes shift (10 nm) while the P3HT polymer exhibits a large Stokes shift (120 nm) (Figure 4.1(d)). The Stokes shift observed in CdSe nanocrystals is generally considered to result from exchange splitting of the excitonic states by electron-hole exchange interaction[29]. The large Stokes shift of P3HT can be attributed to the photoexcitation conformation of polymer, which likely induces conformation of P3HT backbone from non-planar flexible ground state, such as distorted planar structure, to rigid planar excited state[30].
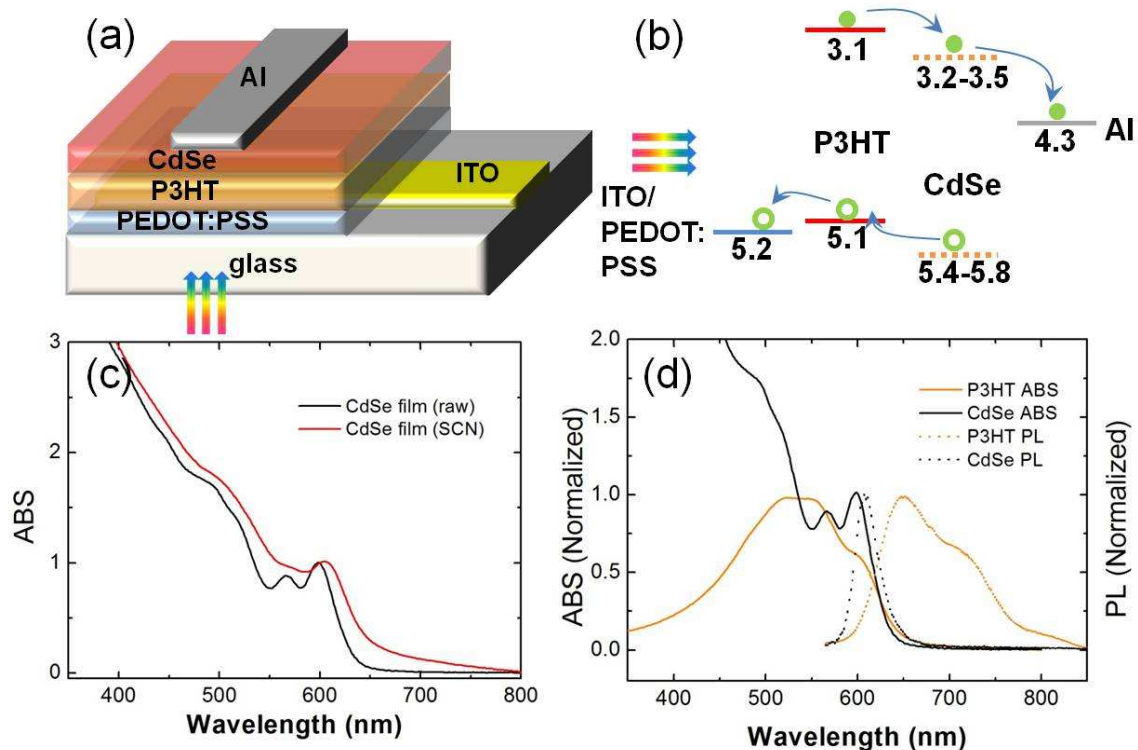
**Figure 4.1**. (a) Schematic of P3HT/CdSe bilayer heterojunction devices (b) energy level alignment of active layer components (value for CdSe nanocrystals adapted from literature[6] for CdSe QD size 2.5-5.5 nm) (c) Normalized UV-Vis absorption spectra of CdSe raw film without ligand exchange (black line) and thiocyanate ligand exchanged CdSe film (red line). (d) UV-Vis absorption spectra and photoluminescence spectra of P3HT (orange lines) and CdSe nanocrystals (raw material without ligand exchange, black lines) in film

CdSe nanocrystals of different sizes have been synthesized, followed by thiocyanate ligand exchange, and incorporated into the P3HT/CdSe bilayer devices to test the optimal size of CdSe nanocrystals. Due to quantum confinement effects, the increase in nanocrystal size will decrease the bandgap and extend the absorption to longer wavelengths, which increases the total absorption and light utilization. However, as a result of narrowing bandgap, the LUMO level of nanocrystal will move deeper in energy and reduce the built-in potential, which causes greater energy loss during the exciton dissociation process. Therefore, one challenge is to tune the size of CdSe nanocrystals to find the optimal trade-off between maximizing absorption and reducing dissociation loss.

Figure 4.2(a) shows the UV-vis absorption spectra of CdSe nanocrystals with different sizes, controlled by adjusting nanocrystal growth time. The average diameter (D) of CdSe nanocrystals was calculated from the first excitonic absorption peak of UV-vis absorption spectrum by using the following equation[5]:

$$D = (1.6122 \times 10^{-9})\lambda_{max}{}^4 - (2.6575 \times 10^{-6})\lambda_{max}{}^3$$
$$+ (1.6242 \times 10^{-3})\lambda_{max}{}^2 - 0.4277\lambda_{max} + 41.57 \qquad (1)$$

Based on the equation, the average diameter (D) of CdSe nanocrystals was 2.6 nm, 3.8 nm, 5.2 nm. The optical bandgap of the CdSe nanocrystals are 2.38 eV (2.6 nm), 2.14 eV (3.8 nm), and 2.03 eV (5.2 nm), derived from their absorption peak.

We then fabricated the bilayer heterojunction solar cells with ITO/PEDOT:PSS/P3HT/CdSe/Al device layout using the CdSe nanocrystals of different sizes. And the current-voltage characteristics of devices with optimal performance are shown in figure 4.2 (d) and summarized in Table 4.1.

The most prominent dependence on nanocrystal size is the short circuit current. It increased monotonically from 0.53 mA/cm$^2$ to 3.01 mA/cm$^2$ when the CdSe nanocrystals size increased from 2.6 nm to 5.2 nm. The better $I_{sc}$ in larger CdSe nanocrystals could mainly be attributed to three reasons: 1) the expanded absorption range (compared with 2.6 nm nanocrystal, 5.2 nm nanocrystal extend the absorption further, covering 550-650 nm region), 2) for the same transport distance, less hopping sites are required for the electrons to transport from the p-n interface to the metal electrode in the larger nanocrystal film, and 3) fewer traps in cells with larger nanocrystals compared with smaller nanocrystals - as larger nanocrystal have a smaller surface to volume ratio and hence a lower density of surface defects caused by dangling bonds which will act as traps and recombination centers for charge carriers that lead to a decrease of photocurrent. This hypothesis is also consistent with the decreasing series resistance observed when increasing the size of CdSe nanocrystal in the device. (Table 4.1)

The open circuit voltage ($V_{oc}$) decreased from 0.87 V to 0.61 V when the CdSe nanocrystals size increased from 2.6 nm to 5.2 nm. The theoretical maximum value of $V_{oc}$ is determined by the built-in potential, which equals to the energy difference between the HOMO level of the donor and LUMO level of the acceptor[31]. The decreasing electron affinity of the CdSe nanocrystals (acceptor) with larger size reduces the built-in potential and increases the energy loss when an electron transfers from the LUMO level of the donor (P3HT) to the acceptor (CdSe nanocrystals), therefore reducing the $V_{oc}$. It is worth noting that the differences between $V_{oc}$ for devices based on 3.8 nm and 5.2 nm CdSe nanocrystals are fairly small, which could be attributed to the relatively flat size

dependence of the LUMO levels of CdSe nanocrystals after 4nm[6] when the size of the nanocrystal is close to or exceeds the Bohr radius for CdSe.

Fill factor (FF) also increased with the increasing size of the CdSe nanocrystals. The high fill factor was achieved by reducing the equivalent series resistance ($R_s$) and increasing the shunt (parallel) resistance ($R_{sh}$).The series resistance is determined by the bulk resistance of the active material and contact resistance between each layer to the current flow. The more efficient charge transport of devices based on the larger CdSe nanocrystals can reduce the series resistance effectively. On the other hand, shunt resistance is a measurement of leakage of current between the two electrodes, which is typically dependent on the stacking morphology and sensitive to device fabrication condition. So the shunt resistance is likely to be independent of CdSe nanocrystals sizes. It is worth noting that most of the devices demonstrate a high fill factor of 0.45-0.60, suggesting a balanced hole and electron transport achieved in the devices. If the hole and electron transport are unbalanced, either hole or electron accumulation will occur, leading to the space-charge limited current, which follows a square-root dependence on applied voltage. And in the case with space-charge effects, the fill factor will be smaller than $0.4$[12, 32].

In conclusion, bilayer heterojunction devices based on P3HT and various sizes of CdSe nanocrystals have been fabricated using the thiocyanate ligand exchange method and the photovoltaic performance of these devices exhibits size dependent behavior. By going from smaller (2.6 nm) to larger (5.2 nm) CdSe nanocrystals, the power conversion efficiency has been improved from 0.19% to 1.06%, mainly attributed to the increase of $I_{sc}$ and FF. The $V_{oc}$ decreases initially with the increasing size but shows size independent

LUMO levels after the size increased above 4 nm. We believe that increasing the CdSe nanocrystals size to even larger size (5.5-8 nm) will further improve the device performance. We have attempted to follow the same ligand exchange process to prepare larger CdSe nanocrystal. However, the nanocrystals aggregated and could no longer be dispersed into DMF or DMSO. Optimization of the ligand exchange process is still under investigation. Modification of ligand exchange process such as adjusting the SCN to CdSe nanocrystals ratio or adopting other solvent/ solvent mixture may help to incorporate large size CdSe nanocrystals. In addition, solid exchange of the CdSe thin film, which does not require re-dispersion of CdSe nanocrystals, may work as an alternative solution. For the results discussed in the following Section 4.3.2, CdSe nanocrystals with size range 4.6-5 nm (absorption 600-610 nm) were used.
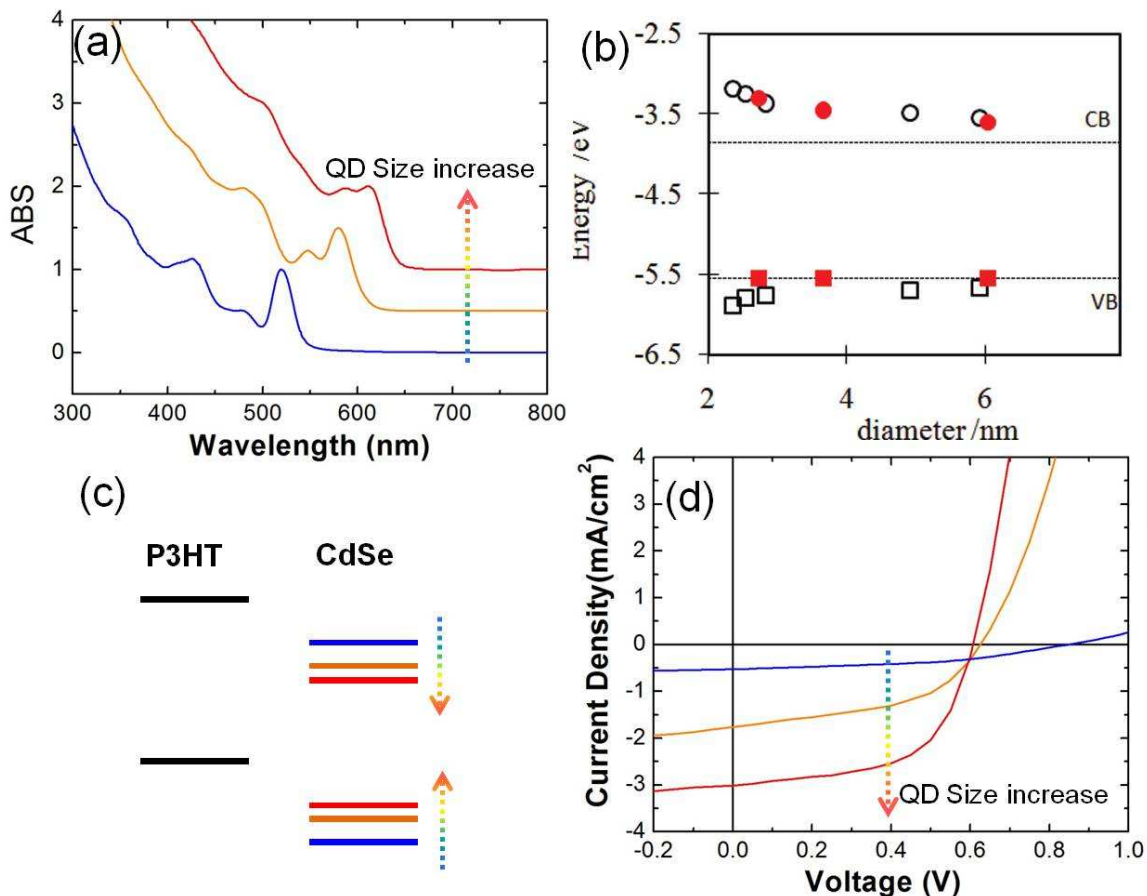
**Figure 4.2**. Effects of CdSe nanocrystal sizes: (a) Normalized UV-Vis absorption spectra of CdSe nanocrystals with different sizes (2.6 nm, 3.8 nm, 5.2 nm from bottom to top), (b) graph adapted from literature[6], demonstrating size dependent HOMO levels (open squares derived from electrochemical characterization and filled squares based on photoemission measurements) and LUMO levels (open circles derived from electrochemical characterization and filled circles based on photoemission measurements) [6], (c) Schematic energy diagram showing the effects of increasing CdSe nanocrystal size, (d) Current-voltage characteristics of P3HT/CdSe bilayer heterojunction devices with different CdSe nanocrystal sizes (2.6 nm, 3.8 nm, 5.2 nm from top to bottom)

**Table 4.1**. Performance parameters of the P3HT/CdSe bilayer solar cells with different CdSe nanocrystal sizes, under AM 1.5G illuminations.

| CdSe size (nm) | Absorption (nm) | $I_{sc}$ (mA/cm$^2$) | $V_{oc}$ (V) | FF | Efficiency (%) | $R_s$ $\Omega{\cdot}cm^2$ | $R_{sh}$ $\Omega{\cdot}cm^2$ |
|---|---|---|---|---|---|---|---|
| 2.6 | 520 nm | 0.53 | 0.85 | 0.43 | 0.19 | 60 | 4768 |
| 3.8 | 580 nm | 1.76 | 0.63 | 0.48 | 0.53 | 23 | 1153 |
| 5.2 | 612 nm | 3.01 | 0.61 | 0.58 | 1.06 | 12 | 1395 |

### 4.3.2 Diffuse Bilayer Solar Cells

Compared to bulk heterojunction P3HT:CdSe devices, bilayer structure offers advantages of easier, independent optimization of each layer and less recombination centers due to well separated donor and acceptor phases. However, bilayer devices typically suffer from limited interfacial area and less than optimal exciton utilization rate due to short exciton diffusion length (typically smaller than 10 nm for P3HT polymer[33]). To overcome these disadvantages in the bilayer solar cell, we took the advantage of "wet deposition" and "simultaneously annealing" of each layer to develop "diffuse bilayer" heterojunction device. A similar approach has been reported very recently[33, 34] through intermixing while fabricating P3HT and PCBM bilayer solar cell with PCBM penetrating into the P3HT layer through the P3HT amorphous region. The comparable size of PCBM domain and CdSe nanocrystal (2-6 nm) leads to an analogous design in the experiment[35]. The diffuse bilayer structure is conceptually in-between bilayer heterojunction and bulk heterojunction, aiming to keep the advantages of both designs, such as large interfacial area and separate pathways for opposite charge carriers. An illustration of the device

layout is shown in Figure 4.3. For the fabrication process, P3HT was first spincast on top of the PEDOT:PSS coated ITO from a high boiling point solvent (chlorobenzene or dichlorobenzene). When the film is still wet, a second layer of CdSe nanocrystals in DMF was spincast on top of P3HT immediately. Then the devices were annealed together at 140 ˚C for 10-15 minutes. Partial intermixing and diffusion of CdSe nanocrystals and P3HT could be driven by swelling of the wet P3HT film and the following thermal annealing process[33, 36].
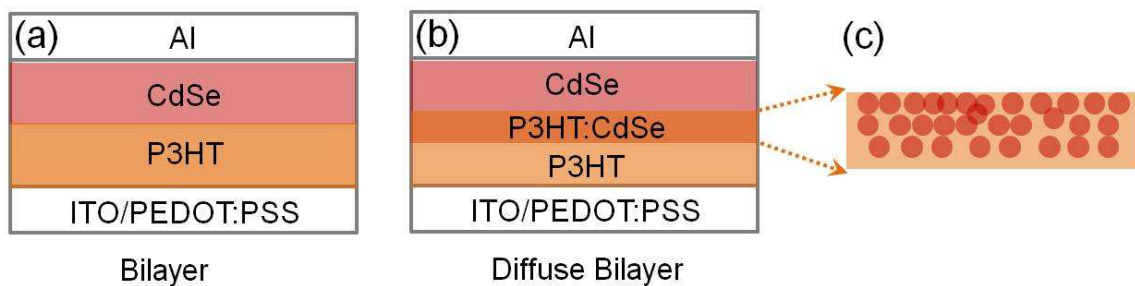


**Figure 4.3.** Schematic of an organic solar cell device with (a) bilayer heterojunction (b) diffuse bilayer heterojunction (c) a zoom-in view of the diffuse (intermixing) layer showing CdSe nanocrystals diffuses into P3HT film.

The bilayer heterojunction solar cells with ITO/PEDOT:PSS/P3HT/CdSe/Al device layout have been fabricated with simultaneously-annealing (diffuse bilayer heterojunction, CdSe nanocrystals spincast when P3HT layer is wet and both layers were annealed together), and compared with devices with separately annealing (bilayer heterojunction, P3HT annealed before spincasting of CdSe nanocrystals and each layer was annealed separately). The current-voltage characteristics of devices with typical performance are shown in Figure 4.4 (c) and summarized in Table 4.2. The best device

148

based on separately annealing P3HT/CdSe bilayer demonstrated a power conversion efficiency of 1.06% with $I_{sc}$ of 3.0 mA/cm$^2$ and $V_{oc}$ of 0.61 V. The best devices based on diffuse (simultaneously annealing) P3HT/CdSe bilayer showed a power conversion efficiency of 1.31% with $I_{sc}$ of 3.9 mA/cm$^2$ and $V_{oc}$ of 0.59 V, which represents a 24% efficiency improvement over traditional bilayer devices using the simultaneously annealing technique. Based on the measurements of five different devices made under the same fabrication conditions, the average efficiency has been improved from 0.89% (bilayer, separately annealing) to 1.06% (diffuse bilayer, simultaneously annealing). Breaking down the critical performance parameters, the enhancement in device efficiency is mainly attributed to the increased short circuit current. Bilayer solar cells with well-known pyridine ligand exchanged CdSe nanocrystals and P3HT have also been fabricated as a comparison (Figure 4.4 (d) and Table 4.2), which exhibited much lower power conversion efficiency than that of thiocyanate exchanged CdSe nanocrystals and P3HT bilayer devices due to less optimization and potentially lower electron mobility[23]. But they have also demonstrated the same trend of enhanced device performance using simultaneously annealing technique. Based on such comparison, using thiocyanate as the ligand exchange material for bilayer CdSe/polymer solar cell is clearly advantageous and such wet-deposition/simultaneously-annealing technique can potentially be applied to other bilayer solar cell fabrication process as well.

To explore the mechanism of increasing photocurrent in diffuse bilayer devices, the absorption and photoluminescence spectra of P3HT film, CdSe film and P3HT/CdSe bilayer under different annealing techniques were compared. The absorption spectra (Figure 4.4(a)) indicate a slightly red-shifted absorption when both films were annealed

together, featuring an enhanced shoulder representing the first excitonic peak of CdSe nanocrystals. The origin or this phenomenon is not clear at this point. However, we hypothesize that depositing the CdSe film on top of the wet P3HT film promotes intermixing between the two layers, and the absorption change in each layer (P3HT, P3HT/CdSe, CdSe) and reflection at the interfaces changed the spatial distribution of the squared optical electric-field strength[37] to facilitate the absorption of CdSe nanocrystals. Also, the diffused CdSe nanocrystals results in a thicker spatial distribution of nanocrytals which could contribute to the increased absorption as well[38]. For the PL spectra (Figure 4.4(b)), the photoluminescence of CdSe film disappeared after the ligand exchange possibly due to the insufficient surface passivation which results in the increase in the non-radiative decay process through surface defects and/or energy traps[39]. On the other hand, 80% of the P3HT PL signal was quenched in the presence of CdSe nanocrystals indicating an efficient charge and/or energy transfer between P3HT and CdSe nanocrystals. According to the literature, in the case of CdSe nanocrystals with shorter ligand, this process is more likely to be charge transfer dominated[40]. The slightly stronger quench in the diffuse bilayer structure can be the result of intimate contact of P3HT and CdSe nanocrystals in the intermixing region, which is consistent with the absorption spectra and implies the possibility of better charge transfer, and hence the larger short circuit current.
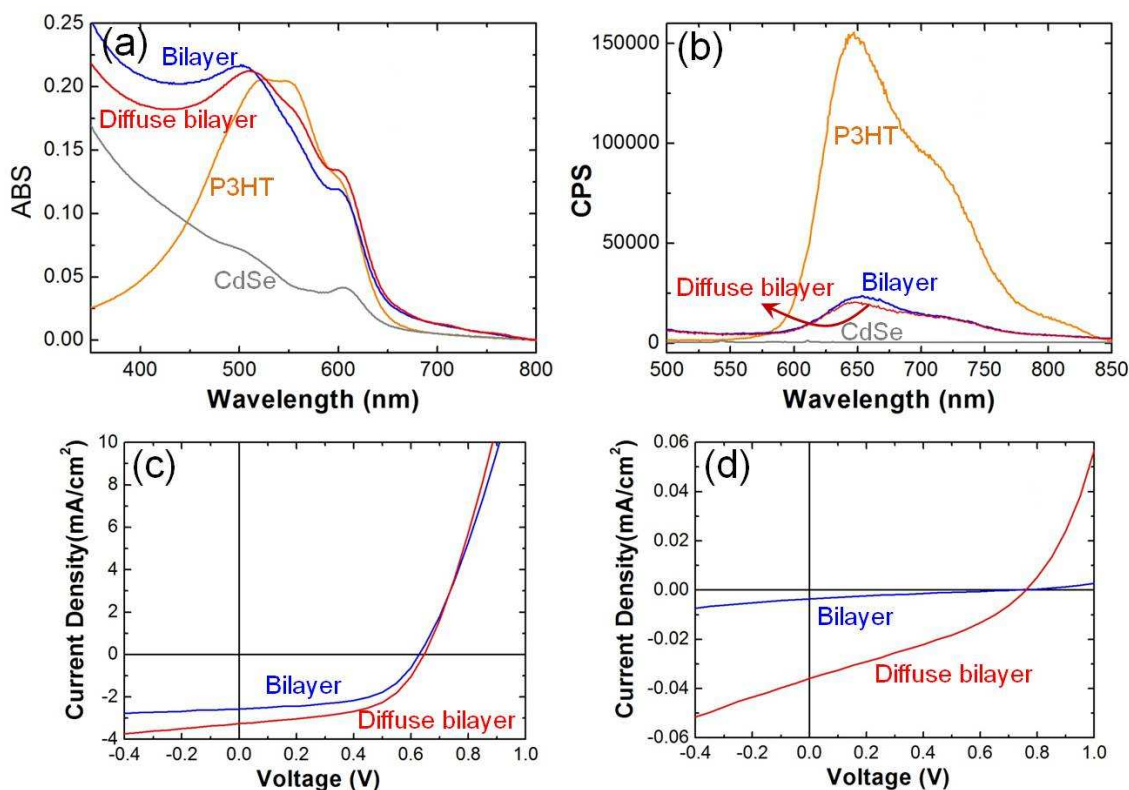
**Figure 4.4.** (a) UV-Vis absorption spectra of pristine P3HT, thiocyanate exchanged CdSe, and P3HT/CdSe bilayer film and diffuse bilayer film, (b) The photoluminescence (PL) of pristine P3HT, thiocyanate exchanged CdSe nanocrystals, and P3HT/CdSe bilayer film, showing strongly quenched P3HT PL in the presence of CdSe nanocrystals. PL spectra were measured on a Fluorolog 3 spectrofluorometer (HORIBA Jobin Yvon, Ltd.) upon excitation at 450 nm. (c) Current-voltage characteristics of P3HT/CdSe bilayer heterojunction devices and diffuse bilayer devices with *thiocyanate* exchanged CdSe nanocrystals and P3HT, (d) Current-voltage characteristics of P3HT/CdSe bilayer heterojunction devices and diffuse bilayer devices with *pyridine* exchanged CdSe nanocrystals and P3HT (Bilayer: P3HT annealed before spincasting of CdSe nanocrystals

and each layer was annealed separately; Diffuse bilayer: CdSe nanocrystals spincast when P3HT layer is wet and both layers were annealed together)

**Table 4.2**. Performance parameters of the P3HT/CdSe bilayer solar cells showing simultaneous annealing/wet film deposition effects, under AM 1.5G illuminations.

| Ligand | Anneal | | $I_{sc}$ (mA/cm$^2$) | $V_{oc}$ (V) | FF | Efficiency (%) |
|---|---|---|---|---|---|---|
| Thiocyanate | separately | Best | 3.0 | 0.61 | 0.58 | 1.06 |
| | | average | 2.7±0.4 | 0.61±0.04 | 0.54±0.02 | 0.89±0.11 |
| | simultaneously | Best | 3.9 | 0.59 | 0.57 | 1.31 |
| | | average | 3.2±0.4 | 0.61±0.01 | 0.54±0.03 | 1.06±0.16 |
| Pyridine | separately | | 0.004 | 0.71 | 0.21 | 0.001 |
| | simultaneously | | 0.036 | 0.76 | 0.34 | 0.093 |

In order to analyze the contribution of absorption at each wavelength to the photocurrent generation, the spectral response/incident photon conversion efficiency (IPCE) of the devices as a function of excitation energy was measured (Figure 4.5). From the IPCE spectra, the diffuse bilayer device has higher monochromatic external quantum efficiency over the entire wavelength range. The biggest enhancement over the bilayer device lies in 500-600 nm region, which could be attributed to 1) increased absorption as we observed in the UV-vis absorption spectrum, 2) larger donor-acceptor interface and 3) decreased "filter effect"[41]. (The strong absorption of P3HT at 500 nm – 600nm will create an exciton generation profile close to the ITO/PEDOT:PSS side and these exciton is located out of the diffusion length towards the interface between P3HT and CdSe nanocrystals, therefore not contributing to the photocurrent generation. However, the diffused CdSe nanocrystals effectively shorten the distance between exciton generation

site and dissociation heterojunction interface, thus weakening the internal "filter effects" and increasing photocurrent generation.) On the other hand, at shorter wavelength range (420-500 nm), the photon conversion efficiency in diffuse bilayer device is also higher, which cannot be explained by the absorption. This improvement may be attributed to either the reduced "filter effects" or increased interfacial area for exciton dissociation.
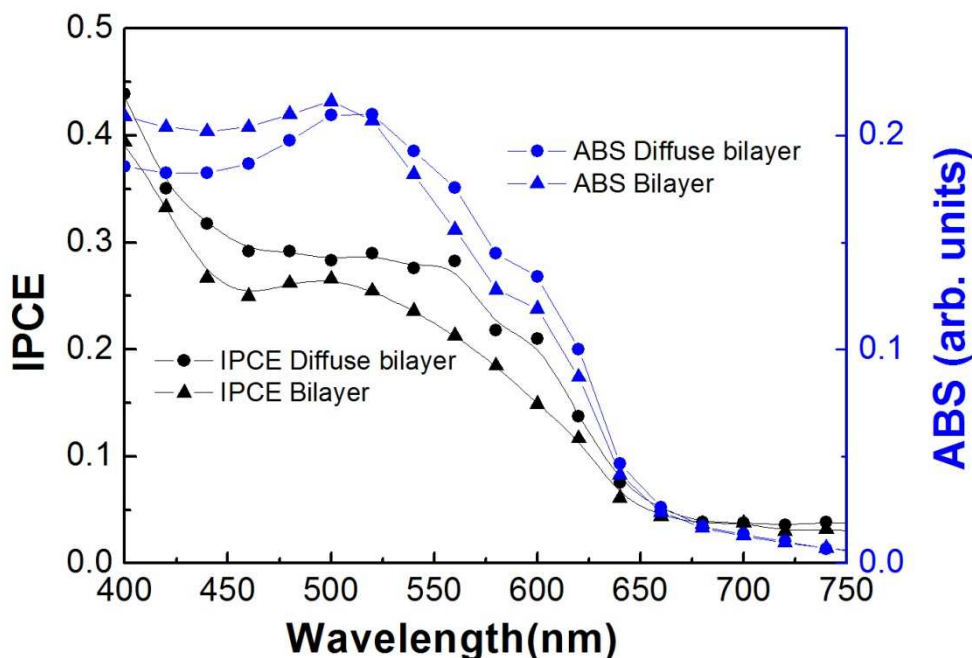


**Figure 4.5.** IPCE and UV-vis absorption of P3HT/PCBM diffuse bilayer and bilayer devices. (●) IPCE for P3HT/CdSe *diffuse* bilayer solar cells, (▲) IPCE for P3HT/CdSe bilayer solar cells, (●) Absorption for P3HT/CdSe *diffuse* bilayer and (▲) Absorption for P3HT/CdSe bilayer

AFM characterization of as-spincast (un-annealed) and annealed P3HT films, in the absence of CdSe nanocrystals, was performed to explore the morphological difference

between the surface and implication of P3HT annealing on the following CdSe nanocrystals deposition. As shown in Figure 4.6, the un-annealed film exhibits a smoother (RMS 600 pm) surface with larger grain size than annealed film (RMS 1000-2000 pm). After annealing the polymer P3HT grain elongates in the z-direction. It is possible that, after deposition of the second CdSe layer, the CdSe nanocrystals swell the P3HT surface and diffuse through the boundary of P3HT grain and then get solidified together after simultaneously annealing. It is worth noting that for the annealed film, the increased surface roughness and grain boundaries also allow the CdSe nanocrystals to penetrate around grain boundaries to a certain extent, which provides a relatively large interface (than that of a sharp "real" bilayer) and likely contributes to the decent efficiency (0.9%) of P3HT/CdSe bilayer devices even without any intermixing treatment. However, AFM measurements did not provide enough structural information in the bulk nor interface between the two components after the deposition of CdSe nanocrystals. To more directly study the morphology difference between bilayer and diffuse bilayer with intermixing layer, cross sectional SEM and EDS mapping was used to characterize the interface. However, due to the facility limitation (stage shifting and low resolution), we were not yet able to obtain the image of cross-section of layers with good resolution on the order of 10s nm. TEM images of the cross-section will be useful to visualize morphology of each layer[42]. X-ray photoelectron spectroscopy (XPS) and Small-angle neutron scattering (SANS) together will also provide useful information about the relative distributions of P3HT and CdSe nanocrystals throughout the active layer[36]. These techniques require special expertise, and sample preparation skills and will be investigated in the future to better understand P3HT/CdSe bilayer system.
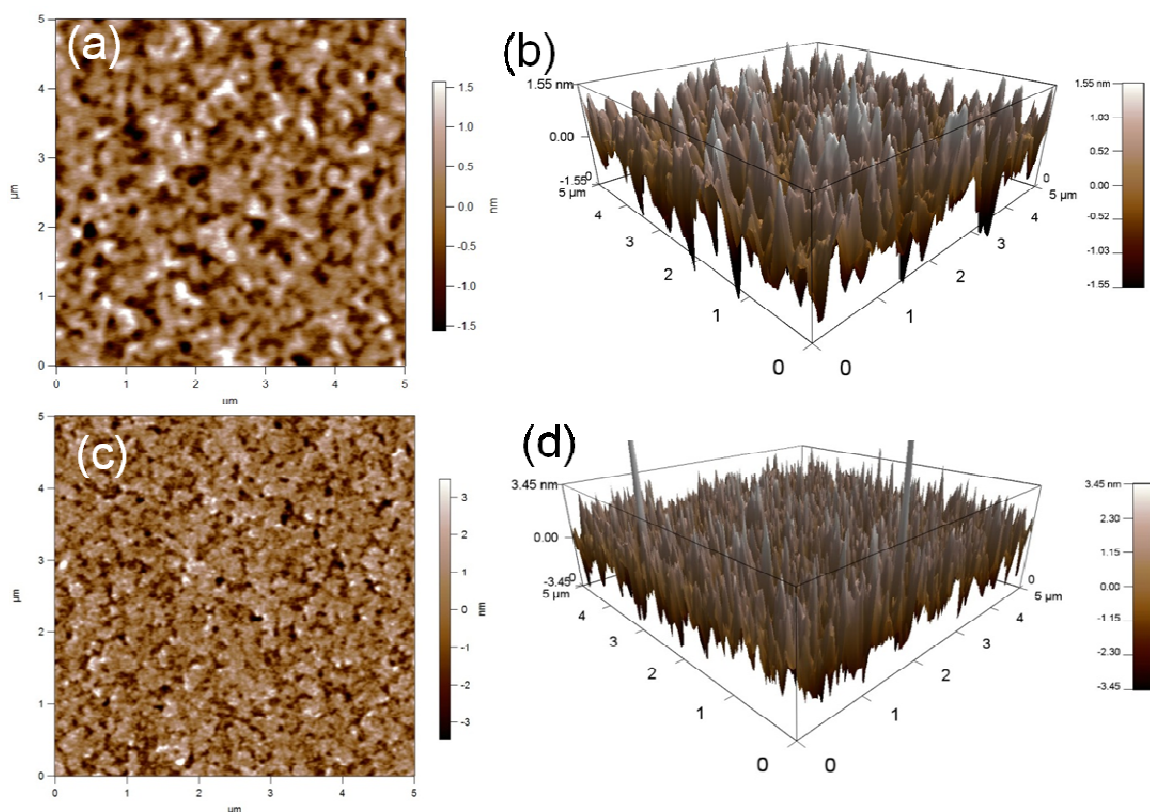
**Figure 4.6.** AFM topography image and 3-D AFM height image of P3HT film before and after annealing: (a) AFM topography image (b) 3-D AFM height image of as spincast and un-annealed P3HT film (z-scale: ±1.55nm), (c) AFM topography image (d) 3-D AFM height image of annealed P3HT film (annealed at 140C for 10 minutes) (z-scale: ±3.45nm). (Scanned sample size 5x5 μm)

### 4.3.3 Inverted Bilayer Solar Cells

Previously, the regular device structure of ITO/PEDOT:PSS/P3HT/CdSe/Al was used, where PEDOT:PSS modifies the ITO layer and serves as the anode contact, and the low-work-function metal Aluminum serves as the cathode. This structure is typically not stable in the air due to: 1) the low work function cathode oxidizes in air, and 2) the thiocyanate ligand exchanged CdSe nanocrystals are air and moisture sensitive. Besides measuring it in the nitrogen filled cell and laminating the device with epoxy and cover glass to avoid air contact, an alternative method - inverted device structure has been explored to overcome the air sensitivity and device instability by modifying the ITO layer as the cathode and introducing a high work function anode. ITO has a work function of 4.5-4.7 eV and lies in between the donor HOMO (5.1 eV) and acceptor LUMO (3.4-3.8 eV). In principle, it can serve as an anode by modifying the contact with PEDOT:PSS deposition (5.2 eV) or cathode by modifying the contact with $TiO_2$[43], $ZnO$[44], and $Cs_2CO_3$[45], which lowers the charge injection barrier and facilitates electron collection at ITO electrode. In the inverted structure, the polarity of ITO was altered by depositing 40 nm $TiO_2$ via Atomic Layer Deposition technique on top of ITO and using it as the cathode for electron extraction instead of hole collection as in the regular device structure. A high work function metal, such as gold (Au) was used as the anode for hole collection. The inverted structure and corresponding band diagram has been shown in Figure 4.7(a) and the device layout and band diagram for regular solar cells was included as a comparison. In the inverted bilayer solar cells, the high work function top electrode (Au) is less air sensitive, which offers better ambient interface. Top Au electrode and

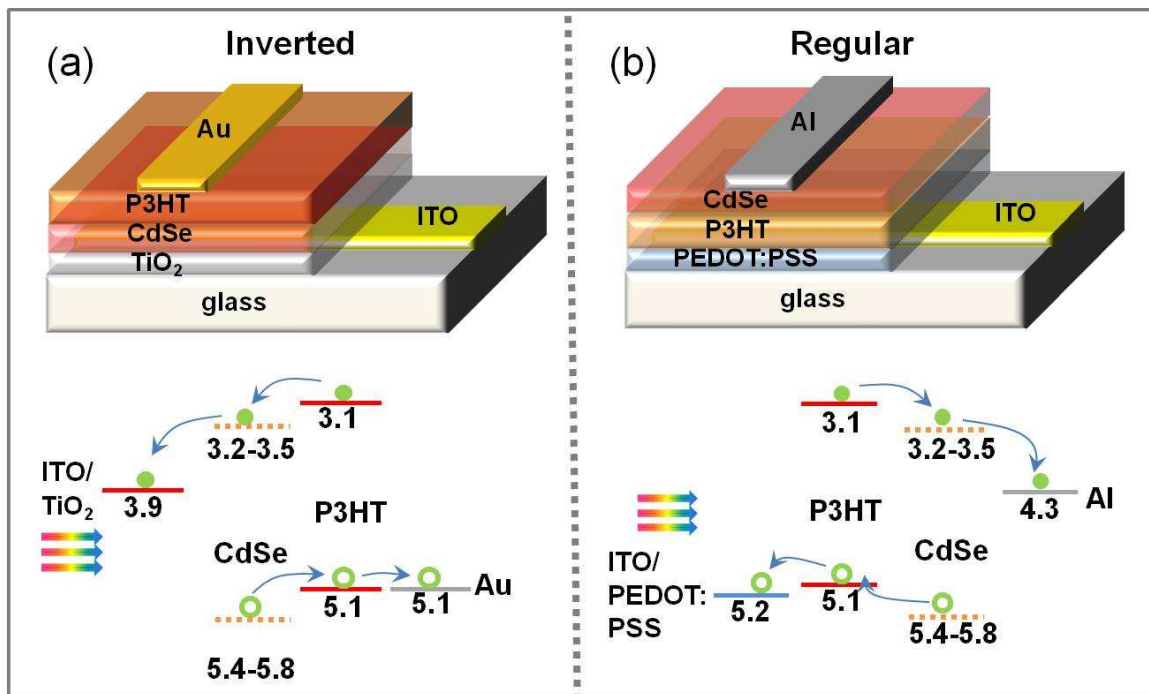donor material (P3HT) can protect the underneath CdSe layer to minimize oxidation of the CdSe nanocrystals.



**Figure 4.7**. (a) Schematic of CdSe/P3HT inverted bilayer heterojunction devices and corresponding energy level alignment, (b) Schematic of P3HT/CdSe regular bilayer heterojunction devices and corresponding energy level alignment. Value for CdSe nanocrystals adapted from literature[6] for CdSe QD size 2.5-5.5 nm, $TiO_2$ modified ITO adapted from literature[46] and PEDOT:PSS modified ITO adapted from literature[47].

Prototype devices based on $ITO/TiO_2/CdSe/P3HT/Au$ have been fabricated and characterized. The CdSe nanocrystal size is about 4.2 nm. The current-voltage characteristics of devices with representative performance are shown in Figure 4.8. The

device was typically tested every 3 minutes for the first 10-20 minutes and every 10 minutes after that in air under continuous illumination. Initially, the as-fabricated device showed a power conversion efficiency of 0.17% with $I_{sc}$ of 1.12 mA/cm$^2$ and $V_{oc}$ of 0.45 V. Improvements of Isc, $V_{oc}$ and FF were observed over time when the device was under AM 1.5G illumination as shown in Figure 4.8. After 20 minutes – 1 hour of light soaking, the increase in photocurrent saturates, and the maximum efficiency reached 0.42% with $I_{sc}$ of 2.4 mA/cm$^2$, $V_{oc}$ of 0.55 V and FF of 0.32. Similar behavior has been observed by other researchers when fabricating inverted bulk heterojunction solar cells with P3HT:PCBM blend and $TiO_2$ modified ITO[48-50]. The enhancement in photocurrent is mainly attributed to the increase of photoconductivity of $TiO_2$ layer and decreased serial resistance. It is believed that shallow electron traps exists in $TiO_2$ layer, which serve as recombination center and impede electron transfer[48, 49]. Illumination will generate photoexcited electrons to fill these traps. The adsorbed oxygen on the surface (O2$^-$) and adsorbed hydroxyl groups from moisture will also contribute to filling the shallow electron traps in $TiO_2$[48, 49]. When the traps are filled, photoconductivity of $TiO_2$ layer increases and $TiO_2$ layer starts to transport electron efficiently, which explains the gradually increasing photocurrent observed under illumination in the I-V characterization experiment. By comparing the performance parameters between the regular and inverted structure, the main difference is the low fill factor observed in inverted solar cells, which is typically around 0.3 while FF in regular devices is around 0.5 or larger. This is most likely an indication of unbalanced electron/hole transfer and defects at the interface between $TiO_2$ and CdSe nanocrystals[51]. The optimization of $TiO_2$ layer is critical and still under investigation in our lab. In addition, optimizing thickness of each layer and

increasing nanocrystal size will also help to improve device performance. Besides improving air stability, the inverted structure also provides a convenient way to treat CdSe nanocrystal films by solid ligand exchange, which overcomes the precipitation challenge when incorporating larger nanocrystals in solution. In addition, P3HT layer won't get affected because P3HT layer is deposited after CdSe deposition and solid ligand exchange treatment in the inverted structure.
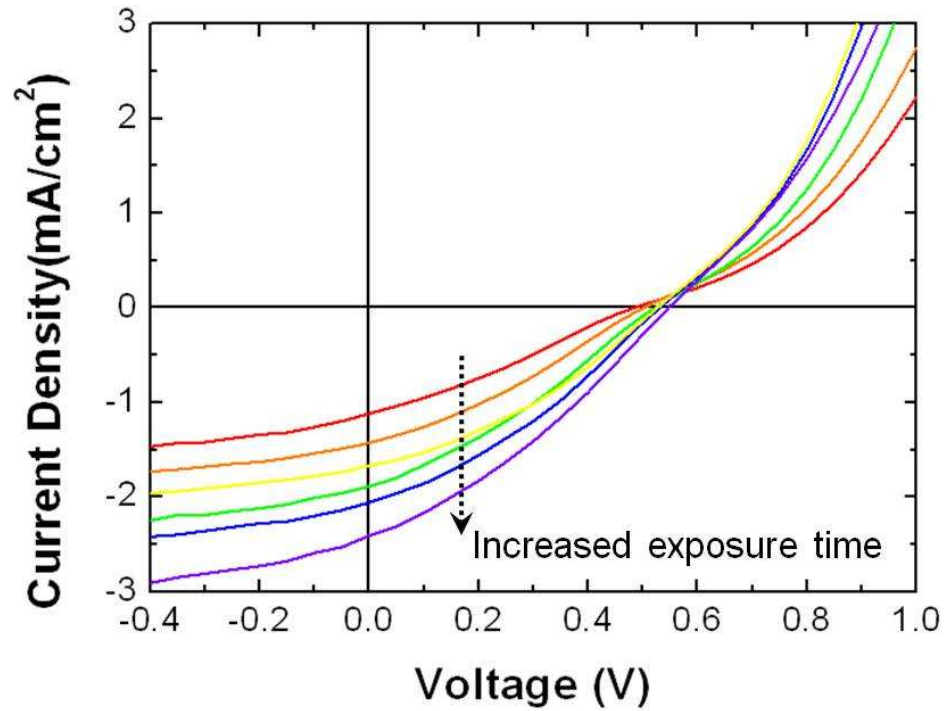


**Figure 4.8**. Current-voltage characteristics of inverted bilayer solar cells under continuous AM 1.5G illuminations. Arrow direction indicates increasing illumination time. The typical total soaking time to saturation is 20-40 minutes, data collection interval: ~3 min for the first 3 data points and ~10 min for the latter points.

### 4.3.4 Bulk Heterojunction Solar Cells

CdSe nanocrystals have also been incorporated into *bulk heterojunction* solar cells using thiocyanate exchange method. The main challenge here is dispersing the CdSe nanocrystals in polymer/small organic molecule semiconducting matrix. After ligand exchange, thiocyanate capped CdSe nanocrystals will only be dispersible in polar solvents, while most popular semiconducting p-type material have poor solubility in polar solvents. In order to accommodate the solubility needs for different components, we developed a solvent mixture consisting of a good solvent for CdSe nanocrystals suspension and a good solvent for the p-type organic molecule. Here we used pentacene precursor as the p-type electron donor. CdSe nanocrystals were first dissolved in DMF to form a suspension. Then a second non-polar solvent was added into solution slowly until CdSe nanocrystals start to precipitate out from the mixture, which determines the maximal ratio for non-polar component. In our experiment, CdSe nanocrystals and pentacene precursor could be co-dissolved in the mixture of DMF and chloroform (1:1 volume ratio), which was then spincast as the active layer followed by an annealing at 200˚C to thermally convert the pentacene precursor to pentacene. Finally, a bulk heterojunction layer consisting of dispersed CdSe nanocrystals in pentacene is achieved. The current-voltage characteristic of a test device without processing optimization is shown in Figure 4.9. It exhibited a low power conversion efficiency of 0.14% with $I_{sc}$ of 0.55 mA/cm2, $V_{oc}$ of 0.63 V and FF of 0.40. The efficiency is mainly limited by the low $I_{sc}$. Further optimization of nanocrystal to organics ratio and processing condition to control film morphology may improve the device performance.
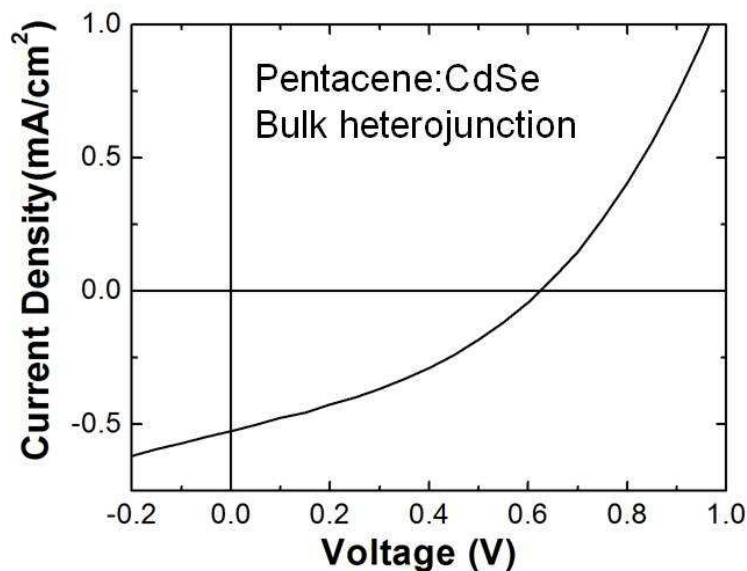
**Figure 4.9**. Current-voltage characteristics of pentacene:CdSe bulk heterojunction solar cells under AM 1.5G illuminations.

## 4.4 Conclusions

In Chapter 4, we demonstrated the photovoltaic application of thiocyanate capped CdSe nanocrystals in combination with P3HT. Orthogonal solvents were used to fabricate solution-processable bilayer solar cells via sequential spincoating. We took advantage of quantum confined property of nanocrystals to optimize the short circuit current and open circuit voltage and developed the wet deposition/simultaneously annealing method to promote intermixing between two components. The devices' performance improved substantially after increasing the size of CdSe nanocrystals and adopting intermixing (simultaneously annealing) methods. The device with 1.3% efficiency was achieved after optimization. It is worth noting that this is the highest efficiency obtained for P3HT/CdSe bilayer solar cells to our knowledge. With the trend of significantly increased short circuit

current upon increasing nanocrystal size, we expect that devices with efficiency over 2% are achievable by increasing CdSe nanocrystal size or adopting other nanocrystal shapes, such as nanorods or branched nanoparticle. This bilayer approach using the thiocyanate ligand exchange method provides a new perspective for the design of organic-inorganic hybrid solar cells and also allows investigation and understanding of the role of each component and interfaces in a controllable manner, which will benefit the optimization and rational device design for bulk heterojunction solar cells. In addition, the bilayer sequential fabrication method is useful to be incorporated into multi-layer multiple junction solar cells, which is believed to be the most promising approach to achieve high efficiency organic solar cell for commercialization.

For future research to better understand this system, there are two main directions:

1) Morphological and structural study to understand the intermixing mechanism. TEM images of the cross-section shall be taken to visualize morphology of each layer[42]. The resonant soft X-ray reflectivity (RSoXR) can be useful to characterize the interlayer diffusion[34]. X-ray photoelectron spectroscopy (XPS) and small-angle neutron scattering (SANS) together will provide useful information about the relative distributions of P3HT and CdSe throughout the active layer[36].

2) Further optimization of interfaces via adjusting process condition and optimization of thickness for each layer. For example, solvent or solvent mixture can be carefully chosen to better "swell" the P3HT surface to further facilitate the intermixing. And high boiling point solvents and slow annealing in solvent vapor can also be used to allow sufficient time for interlayer diffusion and polymer self-assembly, which could potentially improve device performance. In addition, p-i-n structure could be adopted

with a thin layer of P3HT as the hole transport layer, a mixture of P3HT:CdSe diffuse layer as intrinsic absorber layer and a highly doped CdSe nanocrystals (indium doped CdSe has been proven to successfully shift Fermi energy above trap levels and provide bandlike transport in CdSe quantum dot thin-films[9]) as efficient electron transport layer. The relative position of middle absorber can be optimized by controlling the thickness of each layer, so as to form optical interference pattern to enhance light absorbance in the photoactive region to have better light utilization and reduce recombination loss at contacts.

## 4.5 References

1.      Zhou, Y.; Eck, M.; Kruger, M. *Energy & Environmental Science* **2010,** 3, (12), 1851-1864.

2.      Xu, T.; Qiao, Q. *Energy & Environmental Science* **2011,** 4, (8), 2700-2720.

3.      Huynh, W. U.; Dittmer, J. J.; Alivisatos, A. P. *Science* **2002,** 295, (5564), 2425-2427.

4.      Olson, J. D.; Gray, G. P.; Carter, S. A. *Solar Energy Materials and Solar Cells* **2009,** 93, (4), 519-523.

5.      Yu, W. W.; Qu, L.; Guo, W.; Peng, X. *Chemistry of Materials* **2003,** 15, (14), 2854-2860.

6.      Markus, T. Z.; Wu, M.; Wang, L.; Waldeck, D. H.; Oron, D.; Naaman, R. *The Journal of Physical Chemistry C* **2009,** 113, (32), 14200-14206.

7.      Peng, X.; Manna, L.; Yang, W.; Wickham, J.; Scher, E.; Kadavanich, A.; Alivisatos, A. P. *Nature* **2000,** 404, (6773), 59-61.

8.      Qu, L.; Peng, X. *Journal of the American Chemical Society* **2002,** 124, (9), 2049-2055.

9.      Choi, J.-H.; Fafarman, A. T.; Oh, S. J.; Ko, D.-K.; Kim, D. K.; Diroll, B. T.; Muramoto, S.; Gillen, J. G.; Murray, C. B.; Kagan, C. R. *Nano Letters* **2012,** 12, (5), 2631-2638.

10.     Mihailetchi, V. D.; Blom, P. W. M.; Hummelen, J. C.; Rispens, M. T. *Journal of Applied Physics* **2003,** 94, (10), 6849-6854.

11.     Lokteva, I.; Radychev, N.; Witt, F.; Borchert, H.; Parisi, J. r.; Kolny-Olesiak, J. *The Journal of Physical Chemistry C* **2010,** 114, (29), 12784-12791.

12. Li, G.; Shrotriya, V.; Huang, J.; Yao, Y.; Moriarty, T.; Emery, K.; Yang, Y. *Nat Mater* **2005,** 4, (11), 864-868.

13. Heinemann, M. D.; von Maydell, K.; Zutz, F.; Kolny-Olesiak, J.; Borchert, H.; Riedel, I.; Parisi, J. *Advanced Functional Materials* **2009,** 19, (23), 3788-3795.

14. Fu, W.; Shi, Y.; Qiu, W.; Wang, L.; Nan, Y.; Shi, M.; Li, H.; Chen, H. *Physical Chemistry Chemical Physics* **2012,** 14, (35), 12094-12098.

15. Greaney, M. J.; Das, S.; Webber, D. H.; Bradforth, S. E.; Brutchey, R. L. *ACS Nano* **2012,** 6, (5), 4222-4230.

16. Lek, J. Y.; Xi, L.; Kardynal, B. E.; Wong, L. H.; Lam, Y. M. *ACS Applied Materials & Interfaces* **2011,** 3, (2), 287-292.

17. Owen, J. S.; Park, J.; Trudeau, P.-E.; Alivisatos, A. P. *Journal of the American Chemical Society* **2008,** 130, (37), 12279-12281.

18. Zhou, Y.; Riehle, F. S.; Yuan, Y.; Schleiermacher, H.-F.; Niggemann, M.; Urban, G. A.; Kruger, M. *Applied Physics Letters* **2010,** 96, (1), 013304.

19. Seo, J.; Kim, W. J.; Kim, S. J.; Lee, K.-S.; Cartwright, A. N.; Prasad, P. N. *Applied Physics Letters* **2009,** 94, (13), 133302.

20. Gur, I.; Fromer, N. A.; Chen, C.-P.; Kanaras, A. G.; Alivisatos, A. P. *Nano Letters* **2006,** 7, (2), 409-414.

21. Dayal, S.; Kopidakis, N.; Olson, D. C.; Ginley, D. S.; Rumbles, G. *Nano Letters* **2009,** 10, (1), 239-242.

22. Seo, J.; Cho, M. J.; Lee, D.; Cartwright, A. N.; Prasad, P. N. *Advanced Materials* **2011,** 23, (34), 3984-3988.

23.     Fafarman, A. T.; Koh, W.-k.; Diroll, B. T.; Kim, D. K.; Ko, D.-K.; Oh, S. J.; Ye, X.; Doan-Nguyen, V.; Crump, M. R.; Reifsnyder, D. C.; Murray, C. B.; Kagan, C. R. *Journal of the American Chemical Society* **2011,** 133, (39), 15753-15761.

24.     Park, Y.; Choong, V.; Gao, Y.; Hsieh, B. R.; Tang, C. W. *Applied Physics Letters* **1996,** 68, (19), 2699-2701.

25.     Eremina, N.; Degtyarenko, K.; Kopylova, T.; Samsonova, L.; Gadirov, R.; Maier, G. *Theoretical and Experimental Chemistry* **2009,** 45, (1), 63-68.

26.     Scharber, M. C.; Mühlbacher, D.; Koppe, M.; Denk, P.; Waldauf, C.; Heeger, A. J.; Brabec, C. J. *Advanced Materials* **2006,** 18, (6), 789-794.

27.     Christoph J. Brabec, V. D., Ullrich Scherf, *Organic photovoltaics: materials, device physics, and manufacturing technologies*. 2008.

28.     Andres, R. P.; Bielefeld, J. D.; Henderson, J. I.; Janes, D. B.; Kolagunta, V. R.; Kubiak, C. P.; Mahoney, W. J.; Osifchin, R. G. *Science* **1996,** 273, (5282), 1690-1693.

29.     Bagga, A.; Chattopadhyay, P. K.; Ghosh, S. *Physical Review B* **2006,** 74, (3), 035341.

30.     Tretiak, S.; Saxena, A.; Martin, R. L.; Bishop, A. R. *Physical Review Letters* **2002,** 89, (9), 097402.

31.     Brabec, C. J.; Cravino, A.; Meissner, D.; Sariciftci, N. S.; Fromherz, T.; Rispens, M. T.; Sanchez, L.; Hummelen, J. C. *Advanced Functional Materials* **2001,** 11, (5), 374-380.

32.     Goodman, A. M.; Rose, A. *Journal of Applied Physics* **1971,** 42, (7), 2823-2830.

33.     Treat, N. D.; Brady, M. A.; Smith, G.; Toney, M. F.; Kramer, E. J.; Hawker, C. J.; Chabinyc, M. L. *Advanced Energy Materials* **2011,** 1, (1), 82-89.

34.     Chen, D.; Liu, F.; Wang, C.; Nakahara, A.; Russell, T. P. *Nano Letters* **2011,** 11, (5), 2071-2078.

35.     Beal, R. M.; Stavrinadis, A.; Warner, J. H.; Smith, J. M.; Assender, H. E.; Watt, A. A. R. *Macromolecules* **2010,** 43, (5), 2343-2348.

36.     Lee, K. H.; Schwenn, P. E.; Smith, A. R. G.; Cavaye, H.; Shaw, P. E.; James, M.; Krueger, K. B.; Gentle, I. R.; Meredith, P.; Burn, P. L. *Advanced Materials* **2011,** 23, (6), 766-770.

37.     Gruber, D. P.; Meinhardt, G.; Papousek, W. *Solar Energy* **2005,** 79, (6), 697-704.

38.     Chen, L.-M.; Xu, Z.; Hong, Z.; Yang, Y. *Journal of Materials Chemistry* **2010,** 20, (13), 2575-2598.

39.     Milliron, D. J.; Alivisatos, A. P.; Pitois, C.; Edder, C.; Fréchet, J. M. J. *Advanced Materials* **2003,** 15, (1), 58-61.

40.     Xu, J.; Wang, J.; Mitchell, M.; Mukherjee, P.; Jeffries-El, M.; Petrich, J. W.; Lin, Z. *Journal of the American Chemical Society* **2007,** 129, (42), 12828-12833.

41.     Gevaerts, V. S.; Koster, L. J. A.; Wienk, M. M.; Janssen, R. A. J. *ACS Applied Materials & Interfaces* **2011,** 3, (9), 3252-3255.

42.     Moon, J. S.; Takacs, C. J.; Sun, Y.; Heeger, A. J. *Nano Letters* **2011,** 11, (3), 1036-1039.

43.     Schmidt, H.; Zilberberg, K.; Schmale, S.; Flugge, H.; Riedl, T.; Kowalsky, W. *Applied Physics Letters* **2010,** 96, (24), 243305.

44.     Wang, J.-C.; Weng, W.-T.; Tsai, M.-Y.; Lee, M.-K.; Horng, S.-F.; Perng, T.-P.; Kei, C.-C.; Yu, C.-C.; Meng, H.-F. *Journal of Materials Chemistry* **2010,** 20, (5), 862-866.

45.    Li, G.; Chu, C.-W.; Shrotriya, V.; Huang, J.; Yang, Y. *Applied Physics Letters* **2006,** 88, (25), 253503.

46.    Li, C.-Y.; Wen, T.-C.; Lee, T.-H.; Guo, T.-F.; Huang, J.-C.-A.; Lin, Y.-C.; Hsu, Y.-J. *Journal of Materials Chemistry* **2009,** 19, (11), 1643-1647.

47.    Shrotriya, V.; Li, G.; Yao, Y.; Chu, C.-W.; Yang, Y. *Applied Physics Letters* **2006,** 88, (7), 073508.

48.    Golego, N.; Studenikin, S. A.; Cocivera, M. *Physical Review B* **2000,** 61, (12), 8262-8269.

49.    Kim, C. S.; Lee, S. S.; Gomez, E. D.; Kim, J. B.; Loo, Y.-L. *Applied Physics Letters* **2009,** 94, (11), 113302.

50.    Kim, J. Y.; Lee, K.; Coated, N. E.; Moses, D.; Nguyen, T. Q.; Dante, M.; Heeger, A. J. *Science* **2007**, 317, 222.

51.    Chu, C; Shrotriya, V.; Li, G.; Yang, Y. *Appl. Phys. Lett*. **2006**, 88, 153504.